

2021

## Development of Rotary Variable Damping and Stiffness Magnetorheological Dampers and their Applications on Robotic Arms and Seat Suspensions

Lei Deng

Follow this and additional works at: <https://ro.uow.edu.au/theses1>

### University of Wollongong

#### Copyright Warning

You may print or download ONE copy of this document for the purpose of your own research or study. The University does not authorise you to copy, communicate or otherwise make available electronically to any other person any copyright material contained on this site.

You are reminded of the following: This work is copyright. Apart from any use permitted under the Copyright Act 1968, no part of this work may be reproduced by any process, nor may any other exclusive right be exercised, without the permission of the author. Copyright owners are entitled to take legal action against persons who infringe their copyright. A reproduction of material that is protected by copyright may be a copyright infringement. A court may impose penalties and award damages in relation to offences and infringements relating to copyright material.

Higher penalties may apply, and higher damages may be awarded, for offences and infringements involving the conversion of material into digital or electronic form.

Unless otherwise indicated, the views expressed in this thesis are those of the author and do not necessarily represent the views of the University of Wollongong.

---

### Recommended Citation

Deng, Lei, Development of Rotary Variable Damping and Stiffness Magnetorheological Dampers and their Applications on Robotic Arms and Seat Suspensions, Doctor of Philosophy thesis, School of Mechanical, Materials, Mechatronic and Biomedical Engineering, University of Wollongong, 2021.  
<https://ro.uow.edu.au/theses1/1088>



UNIVERSITY  
OF WOLLONGONG  
AUSTRALIA

# **Development of Rotary Variable Damping and Stiffness Magnetorheological Dampers and their Applications on Robotic Arms and Seat Suspensions**

Lei Deng

Supervisors:

Prof. Weihua Li

Prof. Haiping Du

Dr. Shuaishuai Sun

This thesis is presented as part of the requirement for the conferral of the degree:

Doctor of Philosophy of the Engineering

University of Wollongong

School of Mechanical, Materials, Mechatronic and Biomedical Engineering

March 2021

## **Abstract**

This thesis successfully expanded the idea of variable damping and stiffness (VSVD) from linear magnetorheological dampers (MR) to rotary magnetorheological dampers; and explored the applications of rotary MR dampers on the robotic arms and seat suspension.

The idea of variable damping and stiffness has been proved to be able to reduce vibration to a large degree. Variable damping can reduce the vibration amplitude and variable stiffness can shift the natural frequency of the system from excitation and prevent resonance. Linear MR dampers with the capacity of variable damping and stiffness have been studied by researchers. However, Linear MR dampers usually require larger installation space than rotary MR dampers, and need more expensive MR fluids to fill in their chambers. Furthermore, rotary MR dampers are inherently more suitable than linear MR dampers in rotary motions like braking devices or robot joints. Hence, rotary MR dampers capable of simultaneously varying the damping and stiffness are very attractive to solve angular vibration problems. Out of this motivation, a rotary VSVD MR damper was designed, prototyped, with its feature of variable damping and stiffness verified by experimental property tests in this thesis. Its mathematical model was also built with the parameters identified. The experimental tests indicated that it has a 141.6% damping variation and 618.1% stiffness variation. This damper's successful development paved the way for the applications of rotary MR dampers with the similar capability of variable damping and stiffness.

One of the investigated applications of rotary VSVD MR dampers is the positioning control system for a robotic arm. The positioning control system can control arm's point-to-point motions such as a pick& place movement. During the positioning movement of a robotic arm, overshoot and vibration in the settling process are two common problems that impair the positioning performance. To solve these issues, a positioning control system for a robotic arm with a rotary VSVD MR damper is studied in this thesis. A modified rotary VSVD MR damper is utilized in the positioning system. With the proposed control strategy, its positioning control performance was evaluated by both the numerical simulation and experimental test under two excitations: a step signal and a customized signal. Both the simulations results and experimental tests demonstrated that the VSVD control has better performance in reducing overshoot, vibration and energy consumption of the system than the uncontrolled case, variable

damping only case, and variable stiffness case.

Another application of rotary VSVD MR dampers is seat suspensions. Drivers of heavy-duty vehicles are usually exposed to long-term vibration due to the road surface unevenness, which is harmful to their mental and physical health. For the design of a seat suspension, a spring with large stiffness is needed to meet load capacity requirements and avoid end-stop impact when the limited stroke is used out. However, a large stiffness of the seat suspension means large vibration transmissibility. Hence, to reduce the vibration and protect drivers, a VSVD seat suspension with two rotary VSVD MR dampers was investigated. The rotary VSVD MR dampers for the seat suspension are designed, prototyped and installed on the cross-section of the suspension's scissors structure, so that the damping and stiffness of the seat suspension can be regulated by controlling the dampers. By changing their damping, vibration amplitude can be reduced. Additionally, via controlling the stiffness, small stiffness can be prescribed to the small stroke range to reduce the vibration transmissibility. Large stiffness can also be given to the large stroke range to prevent end-stop impacts. Furthermore, the energy can be dissipated by the designed stiffness control strategy so to reduce vibration as well. With three road excitation profiles: harmonic signal, damping signal and random signal, the vibration control performance of the proposed seat suspension is evaluated by both mathematical simulations and experimental tests. Both the results and the simulations proved the vibration was significantly reduced by the proposed VSVD seat suspension.

Apart from vibration, a seat suspension should also be able to reduce the impact and protect drivers in scenarios such as off-road induced shock for heavy-duty, the landmine blast-induced shock for military vehicles and harsh- or crash- landings for helicopters. Considering these kinds of impact can result in severe injuries like spinal fractures to the drivers, a high impact protection capacity is a must for the design of seat suspensions used in the mentioned scenarios. MR dampers have been widely researched in the application of seat suspension. However, most of the research on seat suspension is based on linear MR dampers, and linear MR dampers have a critical drawback of high velocity sensitivity resulted from their mechanical structure. As a result, the seat suspension based on linear MR dampers also possess a high-velocity dependency, and its output damping force increases dramatically with the increase of impact velocity, posing a threat to the drivers' health. Unlike a linear MR damper of which the magnetorheological fluids need to flow from one chamber to another through a very



small gap which causes the high velocity-dependent problem, a rotary MR damper doesn't possess this velocity-dependent problem as its magnetorheological fluids only working on shear mode. Based on these analyses, the impact performance of a rotary MR damper based seat suspension was researched. Its impact protection performance is numerically compared with a linear MR seat suspension with static analysis and dynamic simulation. The simulations, including static analysis and dynamic simulation, proved that the rotary seat suspension has less velocity sensitivity than the linear seat suspension and better performance in impact protection. Furthermore, with an MTS landmark 370 system, the impact protection performance of the rotary MR seat suspension is also evaluated in a small impact velocity range.

## Acknowledgements

First and foremost, I would like to express my sincere gratitude to my supervisor Prof. Weihua Li, who is always ready to provide guidance, support and suggestion. As an expert in the research field of magnetorheological technology, Prof. Li provided profound knowledge and insightful suggestions on the research topics. As a mentor, his work attitude and diligence are great merits for me to follow. As a friend, he always concerns about the career and life development of the students. I also want thanks to my co-supervisor, Prof. Haiping Du, for the great help and support of my PhD research and career development.

Then, I would like to extend my sincere thanks to Dr. Shuaishuai Sun, who is a great role model for me to look up to. Thanks for encouraging me to work harder, providing patient guidance, valuable comments and thoughtful suggestions. Your diligence and the pursuit of excellence will always motivate me on the academic road.

I would like to offer my special thanks to Matthew Christie for the great help. I learnt a lot from him, and been very happy to work with him. I also want to express my appreciation to other colleagues: Dr. Shiyang Tan, Dr. Donghong Ning, Dr. Jiang Yang, Dr. Dan Yuan, Dr. Qianbin Zhao, Dr. Sheng Yan, Xiaojing Zhu, Vladimir Sokolovski, Guolin Yun, Hongda Lu, Dr. Hui Huang, Shida Jin, Jianqiang Yu, Tianhe Jin, Bo Yang, Yuxin Zhang, Wenxing Li, Jin Zhao and Huang Zhang. I want to express my appreciation to the workshop staff for the great help in manufacturing and assembling: Stuart Rodd, Alex Gonzalez and Stuart Goodwin, Douglas Henness.

Finally, I would like to thanks my family. I am very grateful to my parents and sister for the unwavering support and belief in me. Thanks my girlfriend, Wenqi Long, for giving me so much happiness and joy. Your encouragement and support is the most important motivation for my PhD study. Thanks the Greatest of All Time basketball player, Kobe Bryant, for motivating me in the past decades. I was really sad to hear your pass away news on January 26, 2020.

## Certification

*I, Lei Deng, declare that this thesis submitted in fulfilment of the requirements for the conferral of the degree of Doctor of Philosophy, from the University of Wollongong, is wholly my own work unless otherwise referenced or acknowledged. This document has not been submitted for qualifications at any other academic institution.*

---

*Lei Deng*

*22<sup>st</sup> March 2021*

## Table of Contents

Abstract .....	I
Acknowledgements .....	IV
Certification.....	V
Table of Contents.....	VI
List of Figure.....	IX
List of Tables.....	XIII
Chapter 1 .....	1
Introduction .....	1
1.1 Research background and motivation.....	1
1.2 Research objectives.....	3
1.3 Outline .....	3
Chapter 2 .....	5
Literature review .....	5
2.1 Magnetorheological fluids and magnetorheological dampers .....	5
2.1.1 Magnetorheological fluids .....	5
2.1.2 Magnetorheological dampers .....	7
2.2 Variable damping and stiffness.....	12
2.3 Positioning control of robotic arms .....	15
2.4 Vibration control of seat suspensions .....	18
2.4.1 Passive seat suspension .....	18
2.4.2 Active seat suspension .....	19
2.4.3 Semi-active seat suspension.....	21
2.5 Impact protection of seat suspension .....	24
2.6 Conclusion .....	25
Chapter 3 .....	27
Design, testing and modelling of a rotary variable damping and stiffness magnetorheological damper.....	27
3.1 Introduction.....	27
3.2 Structural design and analysis of the VSVD rotary damper.....	27
3.2.1 The structure of the MR VSVD rotary damper.....	27
3.2.2 Working principle .....	29
3.2.3 Magnetic field simulation .....	29
3.3 Experimental testings and analysis .....	30
3.3.1 Experiment setup for property test.....	30

3.3.2 Testing results and analysis.....	31
3.4 Modeling and parameter identification.....	38
3.4.1 Model establishment .....	38
3.4.2 Model establishment .....	40
3.5 Conclusion .....	43
Chapter 4 .....	44
Positioning control system of a robotic arm using a VSVD rotary damper .....	44
4.1 Introduction.....	44
4.2 The proposed positioning system of a robotic arm and its working principle 44	
4.3 System Modeling and Parameter Identification.....	48
4.4 Numerical evaluation of the positioning control system .....	53
4.4.1 Step function signal simulation.....	53
4.4.2 Customised function signal simulation .....	56
4.5 Experimental evaluation of the positioning control system.....	58
4.5.1 Step function signal simulation.....	59
4.5.2 Customised function signal simulation .....	60
4.6 Conclusion .....	63
Chapter 5 .....	64
Vibration control of a seat suspension using VSVD magnetorheological damper .....	64
5.1 Introduction.....	64
5.2 Prototype and working principle of the VSVD seat suspension.....	65
5.2.1 VSVD seat suspension .....	65
5.2.2 VSVD MR damper for the seat suspension .....	66
5.2.3 Property test of the VSVD seat suspension .....	67
5.3 Control strategy design .....	70
5.4 Numerical evaluation of the VSVD seat suspension .....	72
5.4.1 Mathematical modelling of the seat suspension.....	72
5.4.2 Numerical simulation results and analysis.....	77
5.5 Experimental verification of the VSVD seat suspension.....	82
5.5.1 Test system setup .....	82
5.5.2 Test results and analysis.....	83
5.6 Conclusion .....	87
Chapter 6 .....	88
Study on the impact protection performance of a rotary magnetorheological seat suspension .....	88
6.1 Introduction.....	88

6.2	Mechanical structural design of RMRSS .....	88
6.3	Mathematical modelling of RMRSS and LMRSS.....	90
6.3.1	Mathematical modelling of RMRSS.....	90
6.3.2	Mathematical modelling of LMRSS .....	92
6.4	Numerical evaluation of RMRSS and LMRSS .....	95
6.4.1	Transient output force analysis .....	95
6.4.2	Dynamic impact simulations.....	96
6.5	Experimental evaluation of the RMRSS.....	101
6.5.1	Dynamic property characterization of the RMRSS .....	102
6.5.2	Impact test of the RMRSS .....	103
6.6	Conclusion .....	105
Chapter 7	.....	107
Conclusion and future work.....		107
7.1	Conclusions.....	107
7.1.1	Developing a rotary VSVD MR damper.....	107
7.1.2	Positioning control of a robotic arm.....	107
7.1.3	Vibration control of a seat suspension .....	107
7.1.4	Impact protection of seat suspensions.....	108
7.2	Future work.....	108
7.2.1	Developing MR dampers with a large damping range.....	108
7.2.2	Energy saving study on the robotic arm manoeuvre.....	109
7.2.3	Developing an MR damper based semi-active seat suspension with non-linear stiffness .....	109
7.2.4	Application of rotary VSVD MR dampers on the impact protection application.....	110
References .....		111
Publications during my PhD study.....		119
Appendix .....		121
The modified VSVD damper for position control of a robotic arm .....		121

## List of Figure

Figure 2.1. MRF: (a)-(c) without a magnetic field. (b)-(f) with a magnetic field [37, 38]	6
Figure 2.2. Working modes for MRF device [35]	7
Figure 2.3. A typical linear MR damper [56]	8
Figure 2.4. Typical Rotary MR dampers. (a) disc type and (b) drum type [57]	9
Figure 2.5. A drum type MR damper with a serpentine flux path [59]	9
Figure 2.6. A multi-disk MR brake [62]	10
Figure 2.7. Typical single-coil hybrid type of MR dampers. (a) disc type and (b) drum type [57]	11
Figure 2.8. Rotary MR dampers with multi-coils structure [68]	11
Figure 2.9. Configuration and hydromechanical model of the Compressible MR structure. [74]	12
Figure 2.10. A linear VSVD MR damper with MRE unit and MRF unit. [14]	13
Figure 2.11. Design drawing and prototype of VSVD MR dampers with one spring. [15, 16]	14
Figure 2.12. Design drawing and prototype of the VSVD MR damper with two spring. [17]	15
Figure 2.13. Set of gearbox and belt transmission for antagonistic actuation. [85, 86]	16
Figure 2.14. Positioning system based on magnetorheological damper with power generation [86]	17
Figure 2.15. An artificial muscle manipulator based on MR brake [88]	17
Figure 2.16. A typical passive seat suspension [97]	18
Figure 2.17. An active seat suspension with a rotary motor and gearbox [101]	20
Figure 2.18. An active seat suspension with two linear actuators [105]	20
Figure 2.19. An active seat suspension with Two-DOF for military vehicles [106]	21
Figure 2.20. Schematic of an MR seat suspension for helicopters: (a) MR damper (b) seat suspension [19]	22
Figure 2.21. Structure of an MR seat suspension. (a) rotary MR damper (b) seat suspension. [18]	23
Figure 2.22. Structural schematic of a self-powered MR seat suspension [116]	24
Figure 2.23. An MR seat suspension for military vehicles. [120]	25

Figure 3.1. Variable stiffness and damping rotary MR damper structure.....	28
Figure 3.2. Magnetic field simulation: (a) modelled damper, and (b) average flux through the MRF for varied currents .....	29
Figure 3.3. Schematic diagram for the experimental setup.....	31
Figure 3.4. Variable damping behaviour under varied internal damper current $I_1$ .....	32
Figure 3.5. Response to different amplitudes ( $I_1 = 1.0$ A, $f = 0.5$ Hz, $I_2 = 0$ A) .....	33
Figure 3.6. Response to different frequencies ( $A = 10$ degree, $I_1 = 0.5$ A, $I_2 = 0$ A) .....	33
Figure 3.7. Variable stiffness under the varied external damping current $I_2$ .....	34
Figure 3.8. Stiffness response to various amplitudes.....	36
Figure 3.9. Stiffness response to various frequency .....	37
Figure 3.10. Simultaneously working for internal and external damping units.....	38
Figure 3.11. Mathematic model of the proposed rotary MR damper.....	39
Figure 3.12. Modelled results compare to the experiment results of the variable damping tests ( $A = 10$ degree, $f = 0.5$ Hz).....	41
Figure 3.13. Modelled results compare to the experiment results of the variable stiffness tests ( $A = 10$ degree, $f = 0.5$ Hz) .....	42
Figure 3.14. Verification of the proposed model under co-working conditions by comparing the modelled results to the experimental results ( $A = 10$ degree, $f = 0.5$ Hz).....	43
Figure 4.1. Positioning control system of the robotic arm.....	45
Figure 4.2. Block diagram of the real-time control system .....	46
Figure 4.3. Two designed working signals .....	47
Figure 4.4. Schematic diagram of the proposed model for the VSVD damper .....	49
Figure 4.5. Comparison between the modelled results and experimental results .....	52
Figure 4.6. Simulation results under the step function excitation.....	53
Figure 4.7. Simulation results of customised function signal excitation .....	57
Figure 4.8. Experimental test results under the step function excitation .....	59
Figure 4.9. Experimental test results under the customised function excitation (left column: results during the whole period; right column: detailed results of the second top peak). .....	61
Figure 5.1. VSVD seat suspension.....	65
Figure 5.2. Schematic of VSVD MR damper. ....	66
Figure 5.3. Property test of the seat suspension. ....	68
Figure 5.4. Result of variable damping. ....	68
Figure 5.5. Result of variable stiffness ( $I_1 = 0$ A). ....	70



Figure 5.6. Stiffness control strategy demonstration. ....	72
Figure 5.7. The mathematic model of VSVD seat suspension. ....	72
Figure 5.8. The mathematic model of a VSVD damper. ....	73
Figure 5.9. Magnetic field simulation. ....	75
Figure 5.10. Model verification by comparing experimental and simulation results. ...	77
Figure 5.11. Simulated Transmissibility. ....	78
Figure 5.12. Simulated seat displacement and acceleration response.....	79
Figure 5.13. Bump signal excitation simulation results.....	80
Figure 5.14. Displacement response results of random signal excitation simulation ....	81
Figure 5.15. Acceleration response results of random signal excitation simulation.....	81
Figure 5.16. Vibration control performance compare.....	82
Figure 5.17. Experimental test setup.....	82
Figure 5.18. Transmissibility compare.....	83
Figure 5.19. Result of three typical harmonic signals.....	84
Figure 5.20. Bump excitation.....	85
Figure 5.21. Seat displacement response. ....	86
Figure 5.22. Seat acceleration in (a) time domain, (b) frequency domain.....	86
Figure 5.23. Vibration control performance comparison.....	87
Figure 6.1. Schematic of RMRSS.....	89
Figure 6.2. (a) Schematic of LMRSS; (b) mounted linear MR damper.....	92
Figure 6.3. Force response to different impact velocities of RMRSS and LMRSS.....	96
Figure 6.4. Mechanical model for the seat suspensions coupled with an occupant.....	97
Figure 6.5. Simulated time response of the seat suspension systems under impact loads .....	99
Figure 6.6. Velocity dependency analysis.....	101
Figure 6. 7. MTS test system for RMRSS. ....	102
Figure 6. 8. (a) Force–displacement loops and (b) equivalent damping coefficient of the RMRSS under different currents.....	103
Figure 6. 9. (a) Force–displacement response to impact at a constant velocity $V = 0.05$ m/s and (b) generated forces of the RMRSS under varied currents. ....	103
Figure 6. 10. Force-displacement response at velocities of 0.1 m/s (a) and 0.2 m/s (b); (c) force-displacement response at 2.5 and -2.5 A for impact velocities: 0.05, 0.1, and 0.2 m/s.....	105
Figure A.1. Schematic of the VSVD MR damper .....	122

Figure A.2. Experimental setup of the property test .....	123
Figure A.3. Experimental result of variable damping test .....	123
Figure A.4. Experimental result of variable stiffness test.....	124

## List of Tables

Table 3.1. Parameter identification results for the variable damping (the left half) and variable stiffness (the right half) at the conditions: $A = 10$ degree and $f = 0.5$ Hz .....	40
Table 3.2. Parameters used to verify the proposed model .....	42
Table 5.1. Dimensions of the working areas (mm).....	74
Table 5.2. Parameters for MR fluid (Lord MRF-132DG) [18].....	75
Table 5.3. Peak to peak displacement and acceleration .....	80
Table 5.4. Peak to peak displacement and acceleration (value/reduce proportion) .....	85
Table 6.1. Configurations of the rotary MR damper.....	89
Table 6.2. Parameters for MR fluid (Lord MRF-132DG) [18].....	91
Table 6.3. Configurations of LMRSS .....	93
Table 6.4. Parameters for the seat suspension model.....	97

# Chapter 1

## Introduction

### 1.1 Research background and motivation

Smart materials are defined as kinds of materials whose property is controllable under the excitation of external stimuli such as magnetic field, electric field, stress and heat [1]. Based on one kind of smart material: magnetorheological (MR) fluid, MR dampers have attracted significant research attention because of their merits of fast response, large controllable yield stress, simple mechanical structure and less power consumption. The applications of MRF dampers include the automotive industry [2-4], civil engineering [5-7], medical industry [8-10], aircraft industry [11-13].

For an MR damper, its damping force is controllable by regulating MR fluids' applied magnetic field through adjusting the applied current on the electromagnet. Owing to its variable damping characteristics, MR dampers are widely applied in vibration control scenarios as the vibration amplitude can be reduced by adjusting a system's damping. In addition, with advanced control technologies such as skyhook control, fuzzy control and sliding mode control, the vibration reduction performance can be further optimised. Apart from damping, stiffness is another important component of a vibration system. Varying a system's stiffness can change the transmissibility and shift its natural frequency away from the excitation frequency to avoid resonance. Hence, an MR damper with the capability of simultaneously varying damping and stiffness is very attractive as it can combine both the advantages of damping variability and stiffness variability and suppress the vibration to a large degree. Based on this idea, a series of linear MR dampers able to vary damping and stiffness have been developed [14-17], with rotary MR dampers with the same ability rarely reported. The rotary damper is inherently suitable in rotary-movement-based applications such as braking devices and angular joints. Hence, this research investigates the development of rotary MR dampers with the ability to vary damping and stiffness (rotary VSVD MR dampers) and their applications on robotic arms and seat suspensions on the topics of positioning control, vibration control and impact protection.

In terms of the robotic arm system, a fast and precise positioning control performance is critical for the operations like pick&place, drilling and boring. In these

operations, overshoot and vibrations during the setting time are two common problems of the robotic arm positioning system. To solve these issues, this research developed a positioning system for a robotic arm based on a rotary VSVD MR damper. Large damping can be applied to reduce the overshoot and reduce vibration amplitude during the settling time. Besides, a stiffness unit can restore the energy during the deceleration and apply the stored energy in the acceleration process to save energy. The stiffness unit also provides additional torque and reduce overshoot. The rotary VSVD MR damper is designed, prototyped and its feature of variable damping and stiffness is verified. With the proposed control strategy, the positioning system incorporated with a rotary VSVD MR damper was evaluated by both the mathematical simulation and experimental test under the excitations of step signal and customised signal.

Drivers of a heavy-duty vehicle such as an agriculture vehicle or a military vehicle often suffer long-term vibrations caused by road unevenness which poses a threat to their mental and physical health. One effective method to solve this problem is designing a seat suspension that is able to attenuate the vibration. To date, semi-active seat suspensions based on MR dampers have been researched to reduce the vibrations and protect drivers [18-21]. Most of the seat suspensions can only regulate their damping by controlling the damping of an MR damper to attenuate the vibration. However, stiffness variability can also help to reduce vibration. Considering the load capacity requirement and the danger of end-stop impact, commercial seat suspensions are normally designed with springs of large stiffness, which inherently possesses large transmissibility. To meet this conflict of small stiffness for small transmissibility and large stiffness for load requirements, a VSVD seat suspension based on rotary VSVD dampers was developed in this research. With the MTS Landmark test, the characteristic of variable damping and stiffness was validated. After designing a control strategy for the damping and stiffness variability, the vibration control performance of the proposed VSVD seat suspension was evaluated by both mathematical simulation and experimental tests.

Apart from the vibration, impacts such as the off-road induced shock for heavy-duty vehicles, the landmine blast-induced shock for military vehicles and the harsh- or crash- landing for helicopters may also cause severe injuries such as spinal fractures to drivers. Most of the seat suspensions based on the linear MR damper are with high velocity sensitivity which means the MR damper's output force will increase rapidly

with the increase of the impact velocity. Unlike linear MR dampers, of which the MR fluids will transfer from one chamber to another through a narrow gap and result in high velocity sensitivity, rotary MR dampers are less velocity dependent as its MR fluid works in shear mode. Therefore, the rotary MR damper can be a good candidate in the large velocity impact scenarios. Motivated by the above analysis, the impact protection performance of a rotary MR damper based seat suspension (RMRSS) is studied in this research. The rotary MR damper was designed and manufactured for RMRSS. The velocity dependency of RMRSS was numerically analysed and compared with a seat suspension based on a linear MR damper (LMRSS) with static analysis and dynamic simulation. Besides, the impact performance of the seat suspension also evaluated by experimental tests with small impact velocities.

## **1.2 Research objectives**

The overall aim of this research is to develop novel variable damping and stiffness magnetorheological dampers (VSVD MR dampers) and investigate their applications in robotic arms and seat suspension. The specific objectives of this research are:

- (1) Developing a rotary MR damper that can simultaneously vary its damping and stiffness. Building a mathematical model that can precisely describe and predict the behaviour of the VSVD damper.
- (2) Designing a positioning control system for a robotic arm based on a VSVD rotary MR damper to improve the positioning control performance.
- (3) Developing a VSVD seat suspension based on MR technology for improving the vibration control performance and protecting drivers.
- (4) Investigating the impact protection performance of a seat suspension based on a rotary magnetorheological damper

## **1.3 Outline**

Following the introduction, the rest of this thesis is organised as follows:

Chapter 2 presents a literature review related to the research topics. Specifically, the review includes topics of magnetorheological fluids and magnetorheological dampers, variable damping and stiffness dampers, positioning control of robotic arms, vibration control of seat suspensions, and impact protection of seat suspensions.

Chapter 3 introduces the development of a rotary MR damper with the capability of simultaneously varying its damping and stiffness. Its structural design and working

principle are presented. The characteristics of variable damping and stiffness were also verified by experimental tests. To precisely describe and predict damper's behaviour, a mathematical model is established and the parameters of the model were identified.

In Chapter 4, a positioning control system for a robotic arm based on a rotary VSVD MR damper was investigated. The system was designed, manufactured and assembled. With the planned control strategy for adjusting damping and stiffness, the positioning control system was evaluated by mathematical simulations and experimental tests under excitations of step signal and customised signal, respectively.

Chapter 5 focuses on the vibration control of a seat suspension based on a novel rotary VSVD MR damper. The VSVD damper that can be installed on the suspension's scissors structure was designed, prototyped. Incorporated with the VSVD damper, suspension's variable damping and stiffness capabilities were experimentally verified. Under the excitations of harmonical signal, bump signal and random signal, the vibration reduction performance of the suspension was experimentally and mathematically evaluated with the proposed control strategy.

Chapter 6 investigates the impact protection performance of a rotary MR seat suspension (RMRSS). Its velocity sensitivity was numerically compared with that of a linear MR seat suspension (LMRSS) by static analysis and dynamic simulation. Additionally, the impact protection of RMRSS was evaluated by experimental tests with small impact velocities.

## Chapter 2

### Literature review

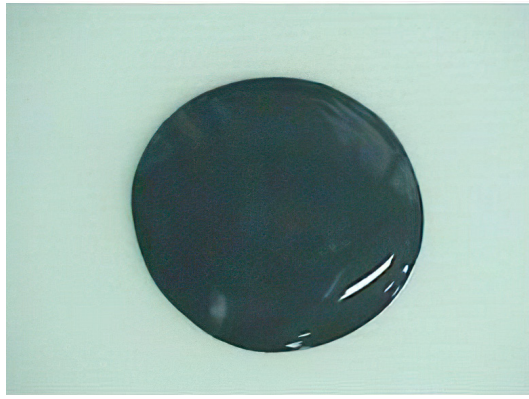
#### 2.1 Magnetorheological fluids and magnetorheological dampers

##### 2.1.1 Magnetorheological fluids

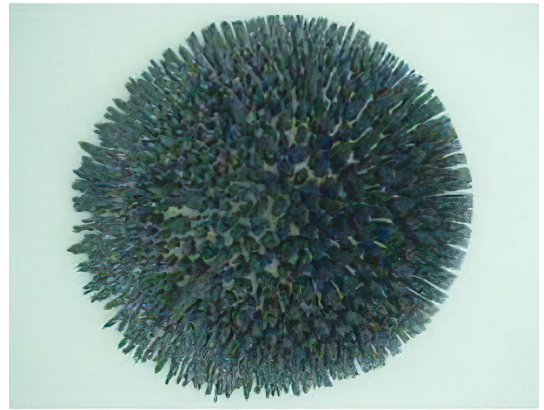
Smart materials are defined as kinds of materials whose properties can be controlled with external stimuli such as magnetic field, electric field, stress and heat [22]. Electro-rheological (ER) materials, magnetorheological (MR) materials, shape memory alloys, piezoelectric materials, and electroactive polymers are the popular smart materials that have drawn great attention of researchers. Among them, magnetorheological materials, known as MR materials, are smart materials whose rheological properties change rapidly (in milliseconds) with an external magnetic field. In MR materials, micro-sized (3-5  $\mu\text{m}$ ) ferrous or iron particles are dispersed in various types of carrier mediums like fluid, foam, elastomer, grease, polymer gel and plastomers [23]. MR materials can be classed as magnetorheological fluids (MRFs) [24, 25], magnetorheological elastomer (MRE) [26, 27], magnetorheological grease (MRG) [28, 29], magnetorheological polymer gels (MRPG) [30, 31], and magnetorheological plastomers (MRPs) [32, 33].

MRFs is a common type of MR materials, as shown in **Figure 2.1(a)**. It is a suspension of micron-sized, magnetically sensitive particles (carbonyl iron) in a carrying fluid such as silicone oil, ethylene glycol and water [24, 25, 34-36]. Without a magnetic field, MRFs is at a free-flowing state (off-state) like a normal liquid as demonstrated in **Figure 2.1(a)**. The carbonyl iron particles in the MRFs are randomly dispersed in the carrying fluid (**Figure 2.1(b)**), and the MRF behaves as Newtonian fluids of which the shear stress increases with the shear rate (**Figure 2.1(c)**). Once applied with a magnetic field, the MRFs will transfer from the previous free-flowing state to a half-solid state (on-state) in server milliseconds. **Figure 2.1(d)** presents a magnet with MRF form a thorns-shape on the surface. The carbonyl iron particles suspended in the carrying liquid are polarised and formed chains structures aligned with the magnetic flux, as shown in **Figure 2.1(e)**. These chains structures resist fluid flow and result in a phenomenon known as Bingham plastics which is non-Newtonian fluids capable of developing yield stress indicated in **Figure 2.1(f)**. This yield stress is related

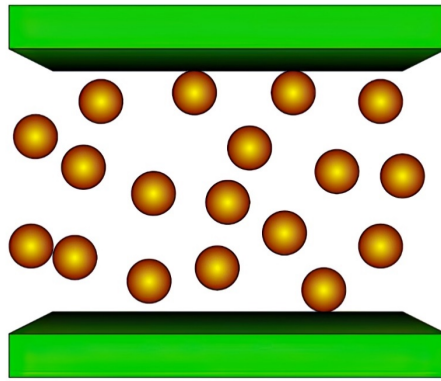




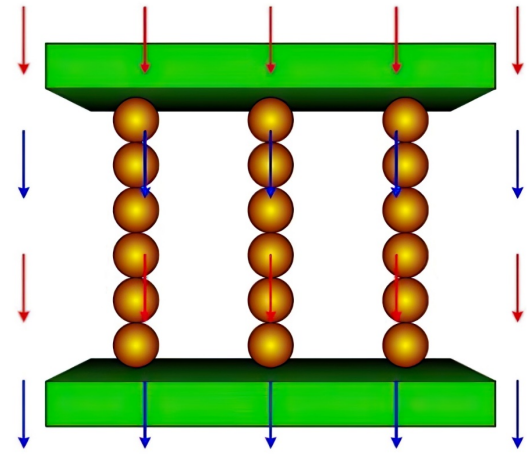
(a) MRF at a free-flowing state



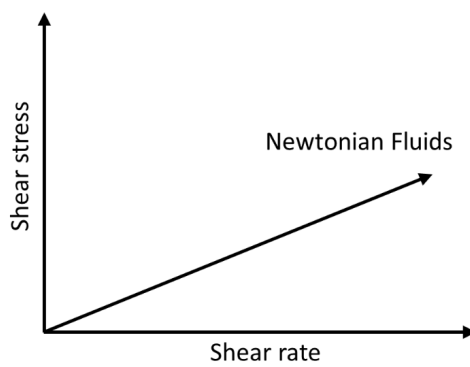
(d) MRF at a half-solid state



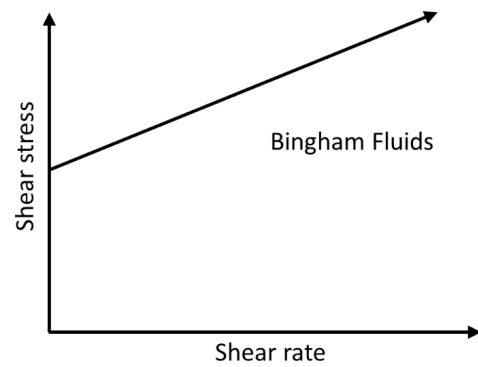
(b) iron particles are randomly distributed



(e) iron particles form linear chains



(c) Newtonian fluids behaviour



(f) Bingham fluids behaviour

Figure 2.1. MRF: (a)-(c) without a magnetic field. (b)-(f) with a magnetic field [37, 38]

to the applied magnetic field, and can change between 10 and 100 kPa [39]. When the external force exceeds the yield stress, the chains of particles will be breakdown under the fluid flow's force, and the MRFs will behave a non-linear shear stress/shear rate

characteristic. Once the applied magnetic field is removed, the MRFs can immediately recover from the half-solid state to the free-flowing state, indicating its good controllability.

Generally, the controllable MR fluids' operation modes are categorised as valve mode (i.e. Flow mode), shear Mode (i.e. clutch mode) and squeeze mode, as demonstrated in **Figure 2.2**. The valve mode involves the fluid flowing because of a pressure gradient between two stationary plates, which can be applied in the areas of hydraulic controls, servo valves, dampers, shock absorbers, and actuators. The shear mode involves fluids located between two plates that move relatively, and this kind of work mode is widely used in clutches, brakes and dampers. The last kind of work modes: squeeze mode involves the fluid running between two plates moving perpendicular to their planes. This work mode has less application and is only used in small-amplitude vibration and impact dampers. In addition, multiple fluid working modes that combined at least two basic operation modes has been alternatively developed in order to enlarge available damping force [40-42].

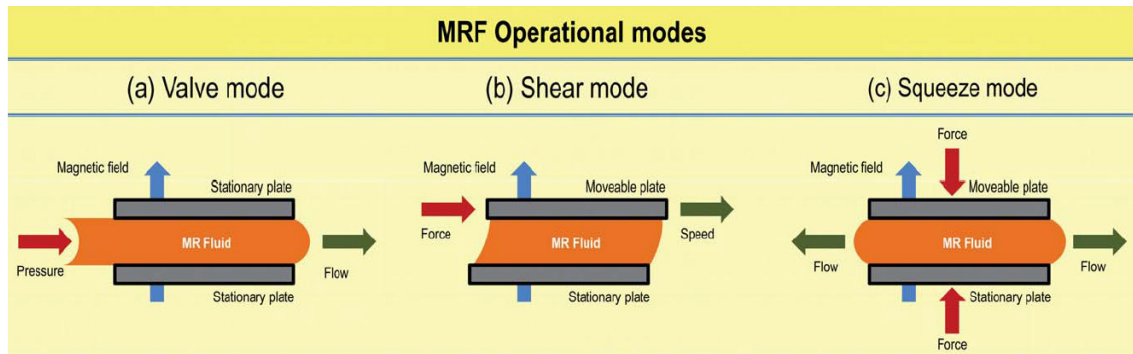


Figure 2.2. Working modes for MRF device [35]

### 2.1.2 Magnetorheological dampers

One of MRFs' applications is magnetorheological dampers (MR dampers). MR dampers are semi-active devices that can change their damping force by varying the magnetic field applied on the MRFs through regulating electromagnetic coils' current. Due to their advantages of large controllable damping force, low power consumption, rapid response and simplicity of design, MR dampers have been widely applied in the semi-active control in vehicle suspension systems [2, 43-45], landing gear systems [46, 47], and seismic protection systems [48, 49]. According to their mechanical structure design, MR dampers can be classed as linear MR dampers and rotary MR dampers.

### *Linear MR dampers*

As shown in **Figure 2.3**, a typical mono-tube linear MR damper consists of a cylinder, a piston rod, a piston head, MRFs and an air accumulator. MRFs are filled in the cylinder, and they can flow from one chamber to another through the MRF gap located between the cylinder and piston head. A magnetic coil is wound on the piston head. When applied with current, the magnetic coil can generate magnetic flux to energise the MRFs in the gap and transfer it from the free-flowing state to the half-solid state in milliseconds. Meanwhile, MRFs' yield stress increases, causing a pressure difference between the two chambers. Consequently, a damping force that is proportional to the applied magnetic field is generated. Other types of linear MR dampers: twin-tube structure, double-end damper, MR dampers with valve, bypass damper and so on have been developed to meet all kinds of requirement [4, 50-55].

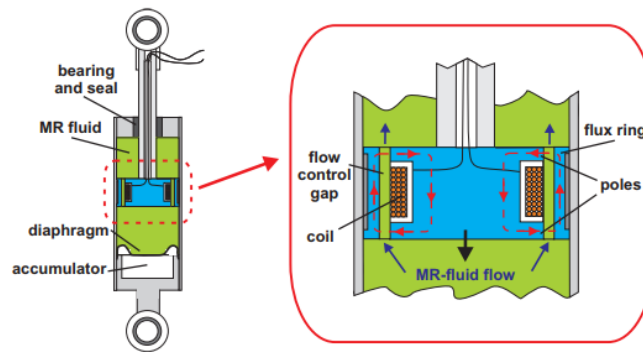


Figure 2.3. A typical linear MR damper [56]

### *Rotary MR dampers*

Apart from linear MR dampers, rotary MR dampers have been widely used in angular movement scenarios. Rotary MR dampers are devices that can reduce the angular speed of a rotating shaft immersed in the MR fluid. In most cases, rotary MR dampers are working at shear mode. Depending on the location where the shear mode occurs, rotary MR dampers can be classified as disc-type MR dampers and drum-type MR dampers, as illustrated in **Figures 2.4(a) and (b)**, respectively. For disc-type MR dampers, the effective area of shear mode occurs at the axial gap of the rotator. In contrast, for the drum-type MR dampers, the working area is located in the radial gap of the rotator. For both kinds of rotary MR dampers, the performance, normally the maximum output damping torque, is highly dependent on several parameters such as magnetic field strength, clearance gap, the size of effective working areas. Magnetic

field strength could be increased by optimising the magnetic flux paths using a combination of magnetic and non-magnetic materials and by increasing the number of the magnetic flux loop using multiple coils. Besides, magnetic saturation and leakage should be avoided by well designing the magnetic field path. For the clearance gap, it is prescribed according to specific cases, normally 0.5~1 mm.

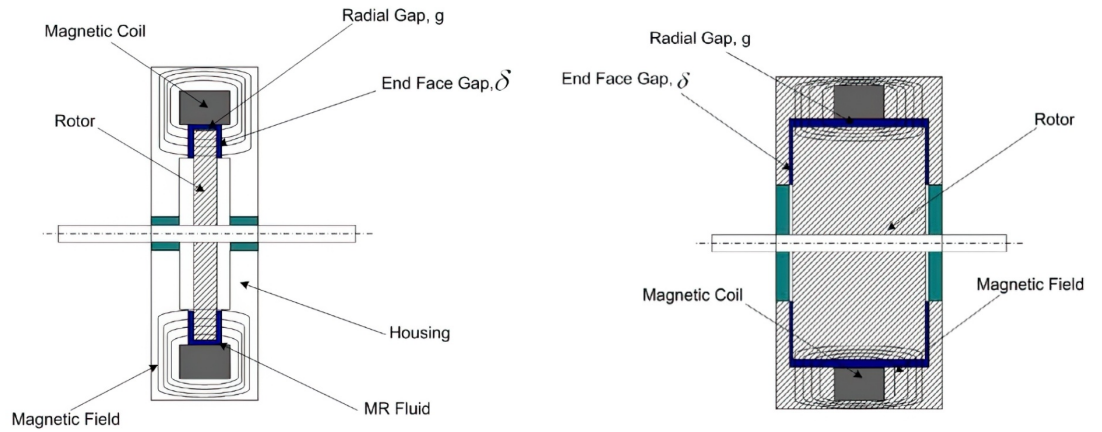


Figure 2.4. Typical Rotary MR dampers. (a) disc type and (b) drum type [57]

Huang *et al.* [58] are among the first to explain the theoretical design and analysis of drum type MR dampers. The MR damper has a very thick cylinder which increases the effective area of shear mode. However, this kind of design may involve a high inertial moment of the shaft, which is considered as an undesirable factor from a design point of view. A flux path optimisation approached was developed by Senkal and Gurocak [59], by designing a drum type MR damper with a serpentine flux path, which is obtained by placing magnetic and non-magnetic rings around the drum and casing (**Figure 2.5**). Kikuchi and Kobayashi [60] studied the involvement of multiple loops to enhance the magnetic field. Although the double coil configuration is not as compact as the serpentine flux path design, it has the advantages of easier assembling, easier maintenance and better hear release capability for the MRF.

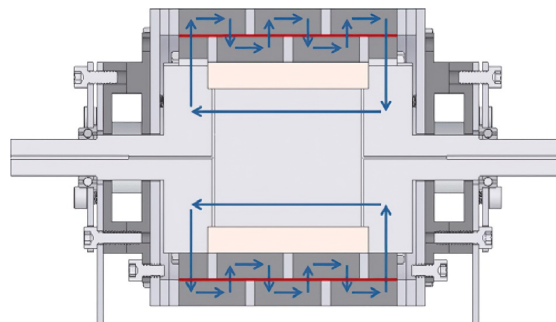


Figure 2.5. A drum type MR damper with a serpentine flux path [59]

In the research areas regarding to disk type MR dampers, Li and Du [61] are among the pioneers who demonstrate idea rotary MR dampers using a single disk. Their rotary MR damper has the advantages of simplicity, lightweight, thin structure and easy maintenance. However, the maximum torque of the damper is only less than 2 Nm, so that it is only suitable for low torque demand and applications. Following this research, Park *et al.* [62] introduced the concept of multi-disk MR brake as demonstrated in **Figure 2.6**. Using the Finite Element Method (FEM) simulation and optimisation, a multi-disk MR brake is designed, and its maximum braking torque could reach to 1013 Nm with a weight of 27.9 kg. In addition, many kinds of rotary MR dampers were developed for the purpose of enhancing the performance of them by using the methods such as coil placement modification [63], flux path optimisation [64, 65], and so on.

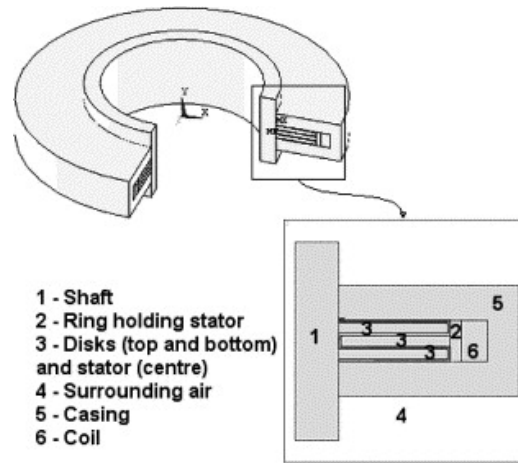


Figure 2.6. A multi-disk MR brake [62]

Following the study of the drum type and disk type rotary MR dampers, hybrid type MR dampers were developed after 2010 [66-68]. These new kind of rotary MR dampers combine the radial flux direction (usually in drum-type MR dampers) and axial flux direction (normally in disc-type MR dampers). One of the configurations is hybrid MR dampers with a single-coil configuration, as illustrated in **Figure 2.7**. The design of a single-coil hybrid MR damper looks like the typical MR damper shown in **Figure 2.4(b)**. However, it should point that there is a difference in the material selection for the housing. For a conventional drum type MR brake shown in **Figure 2.4(b)**, the housing is made of material with a very low permeability so that the magnetic flux will only go through the radial gap and not exist in the end face gaps. In contrast, in the case of hybrid MR dampers, the housing is made of magnetic material, which guiding the flux through the axial gap. Consequently, the single-coil configuration has the



disadvantage that the magnetic flux densities are different in the effective area between radial and axial sides. This is because the flux path lengths at the surface of radial and axial wall are different and the magnetic flux would take the shortest path to build a full magnetic loop. Thus, the magnetic flux density at the radial area is much higher than that at the axial area.

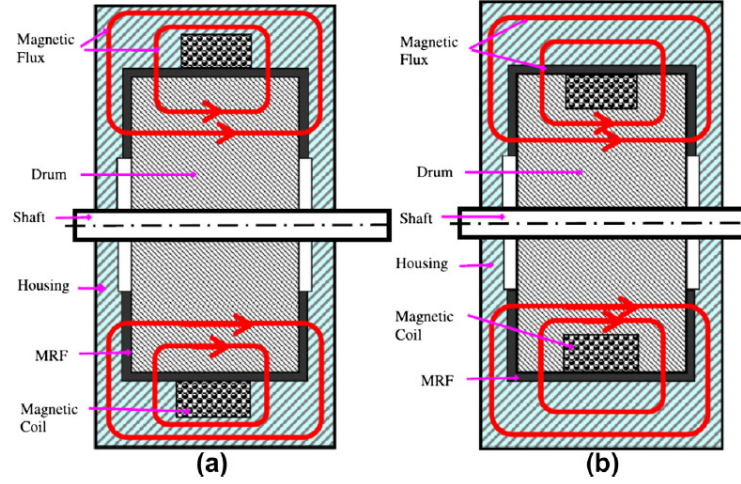


Figure 2.7. Typical single-coil hybrid type of MR dampers. (a) disc type and (b) drum type [57]

For the purpose of improving the uniformity of the single-coil, the configuration of double-coil hybrid MR dampers has been researched as shown in **Figure 2.8** [66-68]. Double coils are located in either the outer gap corner (**Figure 2.8(a)**) or the inner gap corner (**Figure 2.8(b)**). These two kinds of design have relative the same length for axial and radial directions, so that the magnetic flux located in the axial and radial direction is homogeneous. Other kinds of rotary MR dampers like T shape MR dampers [68], rotary MR dampers with a helical flow structure [69] have also been developed.

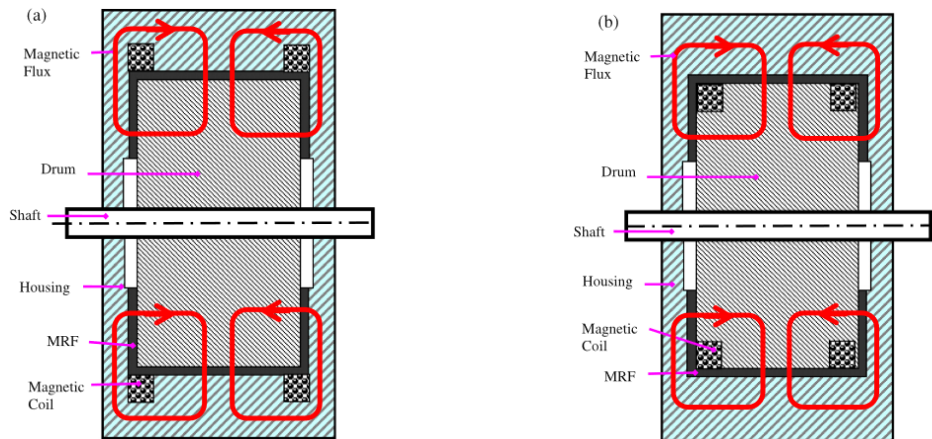


Figure 2.8. Rotary MR dampers with multi-coils structure [68]

## 2.2 Variable damping and stiffness

As the MR dampers are capable of varying damping by regulating the applied electromagnet current, they are widely utilised in the domain of vibration control [13, 70, 71]. For a vibration system, the quantity of vibration energy dissipated can be controlled by adjusting the system's damping, so that the vibration magnitude can be reduced. In addition, vibration can also be suppressed by varying the system's stiffness, as it can shift the natural frequency of the system away from the excitation frequency to avoid. Therefore, a semi-active device that is able to vary the damping and stiffness simultaneously can reduce the system vibration to the maximum. To this end, so far, the idea of variable damping and variable stiffness has drawn significant research attention.

Liu *et al.* [72, 73] built a variable damping and stiffness system with two MR dampers and two springs. One MR damper controls the damping, while the other one can decide whether a parallel spring is working or not to control the stiffness. In this system, the damping and the stiffness can be controlled by two MR dampers separately. However, the system is complicated and not compact. Hong *et al.* [74] designed a liquid spring shock absorber, as shown in **Figure 2.9**. It consists of a bypass MR valve to control the damping. Additionally, because the two rods in the left and right chambers have different diameters, the MR fluid will be compressed when it flows from the left chamber to the right one, and a concept of liquid spring component is realized so as to increase the stiffness of the system. The device is compact, but its stiffness can not be regulated like the damping.

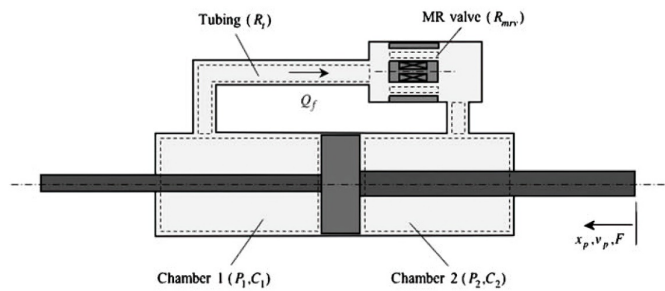


Figure 2.9. Configuration and hydromechanical model of the Compressible MR structure. [74]

To develop a compact device that is able to independently adjust stiffness and damping, Zhu *et al.* [75] proposed a vibration isolator that combined an MR damper with a pneumatic spring. The performance of the device was evaluated through simulation. Liao *et al.* [76] studied an isolator that incorporated a voice coil with four

Magnetorheological elastomer (MRE) elements. The voice coil was used as the tunable damping element, and it is controlled by the relative velocity feedback of the payload, while the four MRE elements were used as the tunable stiffness element, and it is controlled by varying the magnetic field.

Li and Zhang *et al.* [77, 78] developed a variable stiffness and damping MR isolator, which consists of an air spring, two connectors, an MR valve and an accumulator. The air spring and the accumulator work as the spring units. By regulating the MR valve, the air spring and accumulator can work together to provide a small stiffness, or the air spring works alone to provide a large stiffness. Sun *et al.* [14] combined the technology of MRF damper and MR elastomer (MRE) in the design of an isolator, as demonstrated in **Figure 2.10**. It has an MRF unit to control the damping and an MRE unit to control the stiffness.

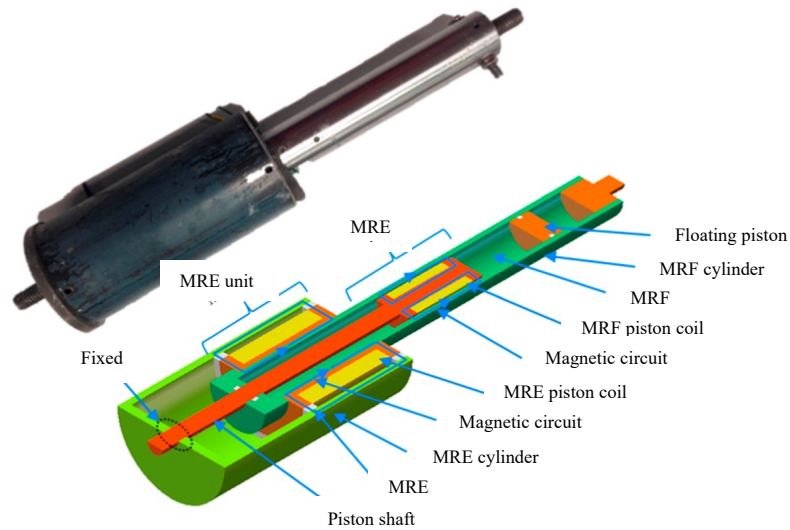


Figure 2.10. A linear VSVD MR damper with MRE unit and MRF unit. [14]

Sun *et al.* [79] designed a variable damping and stiffness suspension for the train. The system consists of an MR damper for varying damping and an air spring for varying stiffness. The simulation results indicated that the variable damping and stiffness suspension can suppress the vibration of the train to the best degree. Sun *et al.* [15] combined two MR damper units and a spring for the first time and developed a variable damping and stiffness (VSVD) MR damper as demonstrated in **Figure 2.11(a)**. The damper unit 1 can control the damping of the stiffness. As for the stiffness control, the spring will not work if damper unit 2 is not active, providing a small stiffness to the system (around 0); the spring will work if the damper unit 2 is active, providing a large stiffness to the system (equals to the stiffness of the spring). In other words, one damper



unit is working as a normal damper to control the damping, while the other damper unit is working as a ‘switch’ to control the working state of the spring, so as to control the stiffness. Based on Sun’s work, Huang *et al.* [16] developed a new compact VSVD damper. The schematic of the damper is presented in **Figure 2.11(b)**. The device integrated an inner damping unit to control damping and an outer damping unit to control stiffness. It combines the inner damper cylinder and the outer damper piston into one component to make itself a compact VSVD damper.

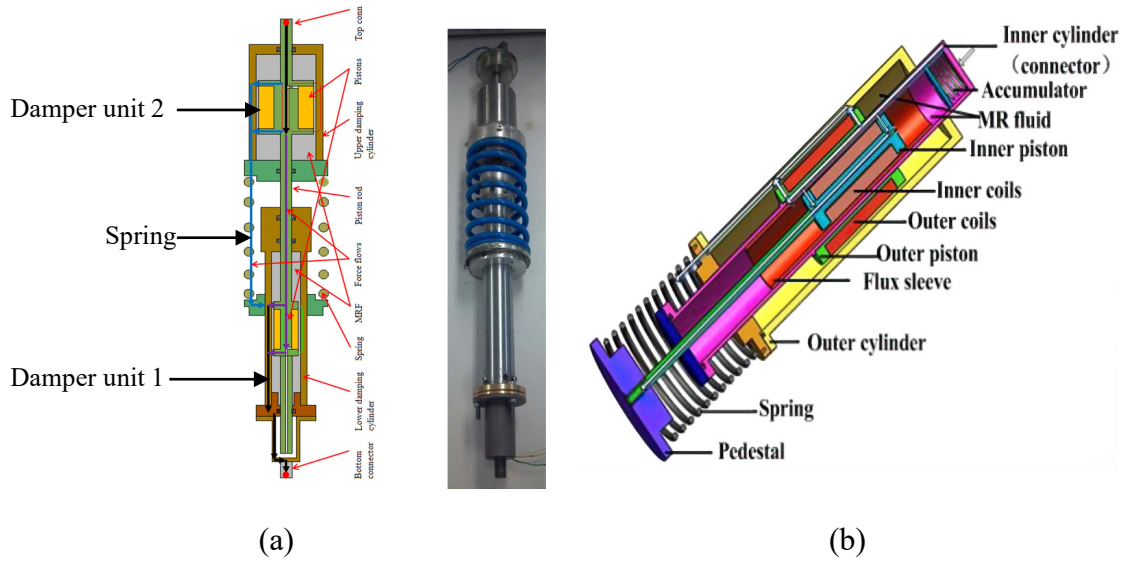


Figure 2.11. Design drawing and prototype of VSVD MR dampers with one spring. [15, 16]

For the above VSVD devices with one spring, the initial stiffness of them when no current applied is very small (can be regarded as zero) and can not meet the system's initial stiffness requirement. To solved this issue, Sun *et al.* [2, 17] introduced another spring based on the previous design. As illustrated in **Figure 2.12**, the device consists of two MR damper units: top damper unit and bottom damper unit, both of which have a piston and a cylinder, respectively. Two springs: spring 1 (with stiffness  $k_1$ ) and spring 2 (with stiffness  $k_2$ ) link the top MR cylinder to the end cap on one side and to the bottom MR cylinder on the other side. The bottom MR damper can control the damping of the device, and the top MR damper can control the stiffness of the device by controlling the working mechanism of the two springs. To be specific, if no current is applied to the top MR damper (case 1), the top damper's damping force is very small, allowing a relative motion between the top damper piston and the top damper cylinder. In this case, springs 1 and 2 work in series, and the stiffness of the device is the smallest with  $k_1 k_2 / (k_1 + k_2)$ . If

the applied current is relatively small (case 2), small relative motion between the top damper piston and the top damper cylinder is allowed. In this case, spring 1 will have a small deformation and spring 2 will have more deformation than the no current applied case. If the applied current is very large (case 3), no relative motion is allowed between the top MR cylinder and the piston so that spring 1 will not deform and only spring 2 is working and the device has the largest stiffness ( $k_2$ ). To sum up, by regulating the current applied to the top MR cylinder, the stiffness of the device can be varied from  $k_1 k_2 / (k_1 + k_2) \sim k_2$ .

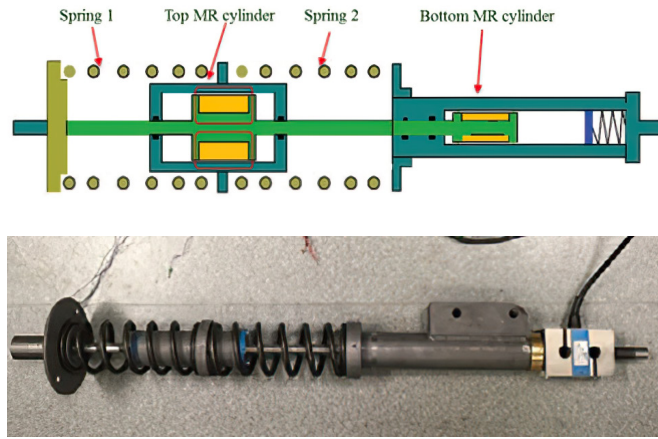


Figure 2.12. Design drawing and prototype of the VSVD MR damper with two spring.  
[17]

### 2.3 Positioning control of robotic arms

Positioning systems play an essential role in industrial processes such as machine tool movements, semiconductor manufacturing systems and robot controls. These positioning systems can control tool's movements during the manufacturing operations such as drilling, boring, and milling, or control point-to-point motions of a robot such as a pick & place robotic arm. Insufficiently rigid connections, low stiffness elements, and heavy loads cause problems of large overshoot and long time vibrations during settling, which have a severe impact on the performance of the positioning system and the whole manufacturing process.

One approach to address these undesirable problems is to develop advanced controllers. For instance, Verschuer *et al.* [80] investigated an  $H_\infty$ -based vibration controller for an industrial pick & place machine to reduce the vibration level and the settling time. The positioning performance was improved by incorporating a vibration controller into the motion control scheme. Wahyudi *et al.* [81] studied a nominal

characteristic trajectory following (NCTF) controller for a point-to-point positioning system. The simulations and experiments of the positioning system indicated that the proposed NCTF controller is much more accurate and robust to inertia and friction variations than a proportion-integral-derivative (PID) controller. Mohd *et al.* [82] investigated an improved NCTF controller for a two-mass rotary system, which has a notch filter working as a compensator to eliminate the vibration of the system due to mechanical resonance. The controller was proved to have a better performance than a conventional PID controller. Tang *et al.* [83] studied a point-to-point positioning control of a pneumatic muscle actuator based system with an improved PID controller, which consists of a conventional PID controller coupled with a pressure-displacement function and a linearizer unit.

Apart from developing controllers, another solution to reduce overshoot and vibrations is incorporating positioning control systems with smart mechanical structures such as magnetorheological (MR) dampers. Jolly [84] demonstrated that an MR braking device that is in parallel with pneumatic actuators enables the positioning system to reach a pre-set position quickly with a smaller overshoot.

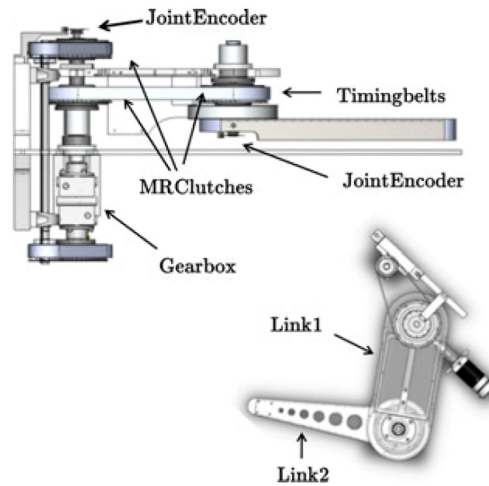


Figure 2.13. Set of gearbox and belt transmission for antagonistic actuation. [85, 86]

Bai *et al.* [87] developed a positioning servo system based on a pneumatic servo rotary actuator and an MR damper. Precision positioning under different loads with arbitrary speeds and points was realised. Yadmellat *et al.* [85] built a two-degree-of-freedom safe robot manipulator with MR clutches, as shown in **Figure 2.13**. The MR clutches contribute to the reduction of the manipulator's mass and inertia because they possess superior torque to mass/inertia ratio over the conventional motors. A promising

position tracking is achieved with the PID control of MR clutches. Sapiński *et al.* [86] developed a positioning system based on a rotary MR damper with self-power capability, as illustrated in **Figure 2.14**. The generator in the system can provide sufficient power for the MR damper to reduce the overshoot and fluctuation during the settling time.

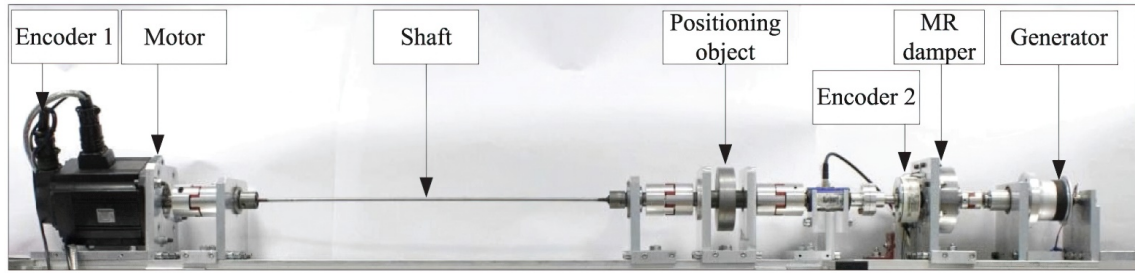


Figure 2.14. Positioning system based on magnetorheological damper with power generation [86]

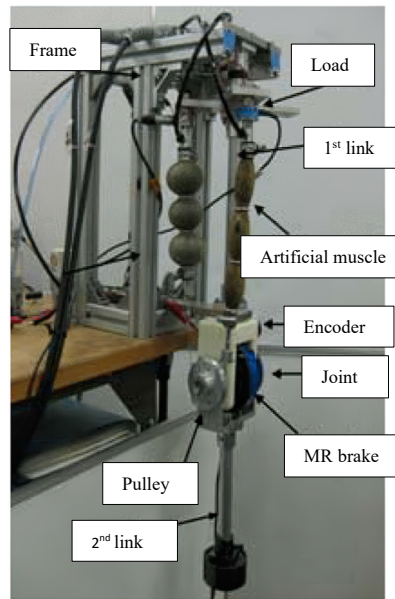


Figure 2.15. An artificial muscle manipulator based on MR brake [88]

To reduce the overshoot of a robot arm caused by the interaction between the robot links and flexible joints, Liam *et al.* [89] introduced MR brakes to the links of the arm. With the feedback control using hybrid actuators, DC motor, and MR brakes, the effectivity to control the position and behaviour of the flexible joints of the manipulator was numerically validated. Liam *et al.* [90] also studied a two-degree-of-freedom robotic arm design with flexible joints driven by a DC motor and controlled by an MR brake. The MR brake was utilised to provide variable constraints in the motion of a manipulator and compensate for overshoot of the system. Tomori *et al.* [91] developed a

one-degree-of-freedom manipulator using an artificial muscle and an MR brake. By regulating the apparent viscosity of the MR brake using an evaluation function, the vibration and overshoot of the manipulator were controlled. Nagai *et al.* [88] investigated an MR brake with an adjustable viscosity coefficient to improve the position and vibration control performance of an artificial muscle manipulator (**Figure 2.15**). The influence of the viscosity coefficients with different weight coefficients on the position and vibration control performance was studied.

## 2.4 Vibration control of seat suspensions

As reported in [92], Krajnak pointed out that whole-body vibration (WBV) may cause various diseases, including back and neck pain, neuropathy, cardiovascular diseases, even cancer. The driver of heavy-duty vehicles is a risky occupation that suffers low-frequency whole body vibration caused by road unevenness, engine vibration or car body vibration. Another research [93] indicated that a long-term operation of heavy commercial vehicles could cause diseases of the muscle, bones, digestion disorders, and even the visual system. To protect the driver's health and improve driving comfort, a seat suspension that can reduce the undesirable vibration transferred from the car body to the driver is required. To this end, numerous research on the seat suspension has carried out to meet this requirement. The seat suspension can be classified as passive seat suspension, semi-active seat suspension, and active seat suspension [94-96], and the development of these three kinds of seat suspensions is introduced as follows.

### 2.4.1 Passive seat suspension

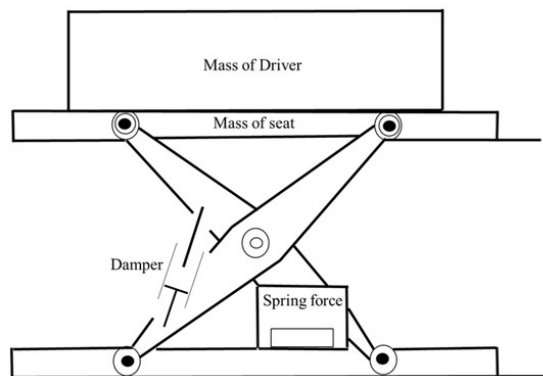


Figure 2.16. A typical passive seat suspension [97].

Passive seat suspension only utilises mechanical components such as spring, air cushion, or conventional vibration isolator. As its mechanical properties including

damping and stiffness are time-invariant, passive seat suspension can only attenuate the vibration at a limited frequency range. Compared with the other two kinds of seat suspension, passive seat suspension has advantages of simple structure and no power consumption; and disadvantages of lacking adaptability to different vibration conditions. **Figure 2.16** shows a typical passive seat suspension containing an air-spring and a hydraulic damper which was designed by Maciejewski et al. [97]. The suspension performs better than the conventional suspension in the 0-4 Hz frequency range, and it has nearly identical performance as the conventional suspensions at the larger frequency range. With the resonance frequency, the proposed suspension has the largest improvement than the conventional suspension. Holtz and Van Niekerk [98] studied an air-spring suspension for articulated and rigid-frame dump trucks with an air-spring and an auxiliary volume.

Le and Ahn [99] developed a negative stiffness suspension that uses two symmetric negative stiffness structures parallel to a positive stiffness structure. The developed negative stiffness suspension achieved a good vibration control performance in the low-frequency range. Tu *et al.* [100] proposed a negative stiffness magnetic spring for vehicle seat suspensions to reduce the vibration of vehicle drivers. The designed magnetic spring is beneficial to the low dynamics stiffness and can reduce the resonance frequency without compromising loading capacity.

#### 2.4.2 Active seat suspension

Active seat suspension consists of sensors to acquire motion and force data, processors such as NI myRIO to analyse the data and calculate designed force/torque according to specific control schemes, and actuators to generate force for attenuating the vibration. This kind of suspension possesses an excellent vibration reduction performance as it can regulate the mechanical properties according to different working conditions. Compared to the passive seat suspension, the active seat suspension has more sophisticated and expensive mechanical and electrical structures. Besides, as the actuators could not provide force once the control system failed, the worse fail-safety performance becomes one shortage of the active seat suspension.

**Figure 2.17** shows an active seat suspension designed by Ning *et al.* [101] for heavy-duty vehicles. The proposed seat suspension system applies a rotary motor and a gearbox on a scissors suspension to provide active actuation. An  $H_\infty$  control strategy with friction compensation was designed to attenuate the seat vibration actively. The

experimental tests proved that the proposed active seat suspension can perform better ride comfort in the frequency range of 2-6 Hz than a passive seat suspension. Ning *et al.* also designed the observer-based terminal sliding mode control [102], disturbance observer-based Takagi-Sugeno fuzzy control [103],  $H_\infty$  controller with friction compensation [104] for the active seat suspension.

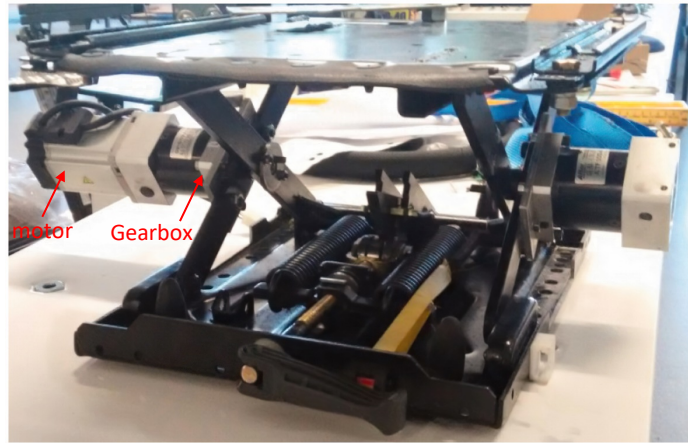


Figure 2.17. An active seat suspension with a rotary motor and gearbox [101].

As illustrated in **Figure 2.18**, Gan *et al.* [105] developed an active seat consists of two electromagnetic linear actuators in parallel with a spring and damper system. The results showed that the periodic vibration containing single and multiple frequencies can be reduced substantially. The robustness and stability of the control system were also validated.

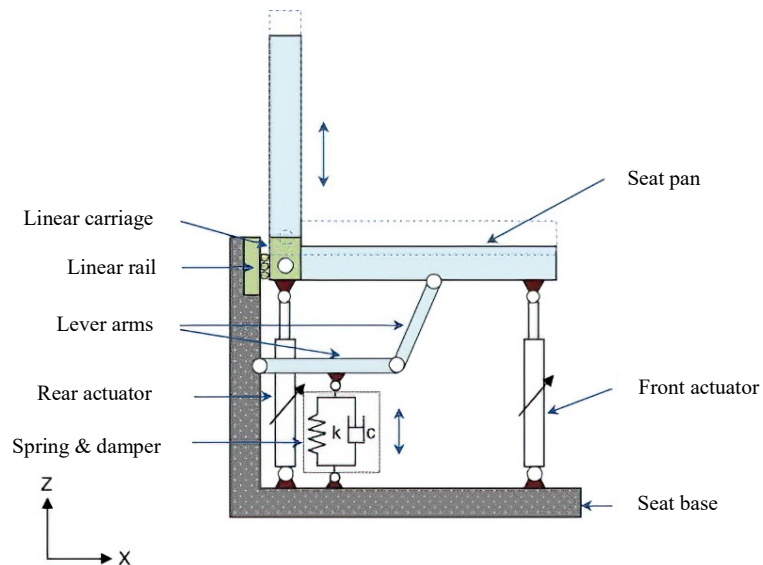


Figure 2.18. An active seat suspension with two linear actuators [105]

Kieneke *et al.* [106] designed an active seat suspension with Two-DOF for military



vehicles. As demonstrated in **Figure 2.19**, The seat suspension was mounted on a vehicle body through a rigid link console that only allows translational movements between the seat and the console in vertical and lateral directions. A linear motor was used to reduce the vibration in the horizontal direction, and another linear motor together with an air spring were used to attenuate the vertical vibration. Compared with a passive seat suspension, the designed active seat can improve the ride comfort by 39% for vertical dynamics and by 16% for lateral dynamics.

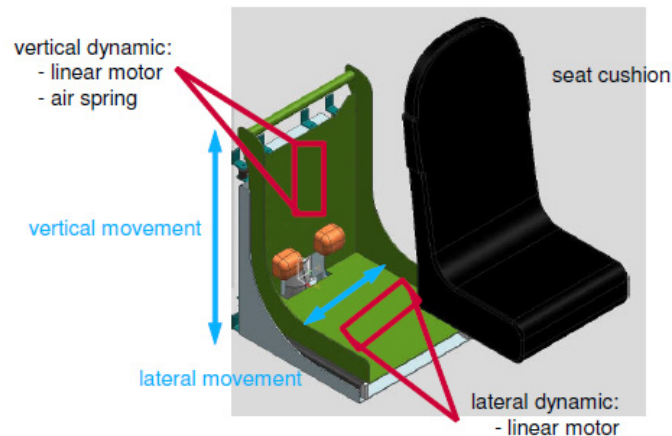


Figure 2.19. An active seat suspension with Two-DOF for military vehicles [106]

#### 2.4.3 Semi-active seat suspension

Semi-active seat suspension is quite similar to active seat suspension. It has sensors to acquire real-time data, and processors to analyze data and to give commands. The difference is that semi-active seat suspension utilises smart devices such as magnetorheological or electrorheological dampers [107, 108] instead of motors. By controlling the smart devices' properties, the damping or stiffness of the seat suspension can be regulated according to different external excitation. Therefore, semi-active seat suspension is more adaptable to various external excitations than passive suspension. Compared with active seat suspension, semi-active seat suspension has simpler mechanical and electrical structures with less power consumption. Semi-active seat suspension also has better fail-safety performance than active seat suspension as an MR damper can still work as passive dampers if the semi-active control failed. Therefore, semi-active seat suspension featuring MR dampers for vibration control has been extensively researched in recent decades.

Choi *et al.* [109, 110] firstly studied the MR seat suspension for vibration control. An MR damper was designed for the seat suspension. The performance of this



suspension was validated through a hardware-in-the-loop-simulation methodology. Park and Jeon [111] researched the vibration control of an MR seat suspension with a Lyapunov type robust control considering time delay. MacManus *et al.* [112] used MR seat suspension to reduce both vibration and end-stop impacts. The experimental results indicate the MR seat suspension performs superior to the conventional seat suspension in reducing vibration and end-stop impact, especially under high-magnitude excitations.

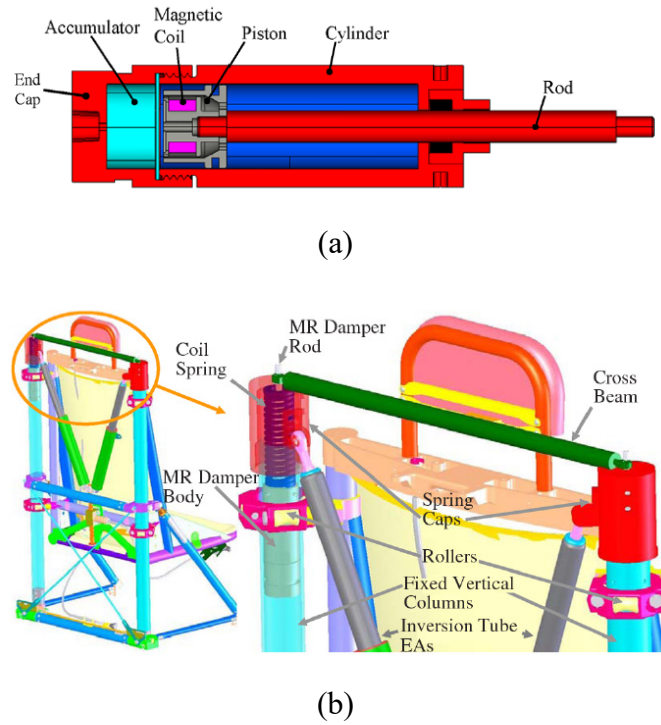


Figure 2.20. Schematic of an MR seat suspension for helicopters: (a) MR damper (b) seat suspension [19].

Wereley's group has done an extensive and profound study on the MR seat suspension for helicopters. Choi and Wereley numerically studied the mitigation of biodynamic response to shock and vibration using MR helicopter crew seat suspensions [20, 21]. As follows, Hiemenz *et al.* [113] investigated a simple load limiting control algorithm for an MR suspension applied to a helicopter crew seat. They also designed and manufactured an MR seat suspension for a helicopter [19], with the schematic shown in **Figure 2.20**. Two linear MR dampers indicated in **Figure 2.20(a)** are mounted within two fixed vertical columns to which the seat rollers attach. A skyhook control algorithm was implemented for this system. The experimental results proved that the seat suspension can significantly reduce the dominant rotor-induced vertical vibration and vertically induced seat rocking. Singh and Wereley [114] studied the effect of the

occupant's compliant body for vertical shock events response to sink rates from 5 to 10 m/s.

Du *et al.* [115] designed a magnetorheological elastomer (MRE) isolator capable of variable stiffness for a vehicle seat suspension. A sub-optimal  $H_\infty$  controller that offers a continuously variable stiffness control strategy for the MRE isolator was proposed for the MRE isolator. The numerical simulation indicated that the proposed controller works better than conventional on-off control.

In the above research on MR damper seat suspension, most of them are utilized linear type MR dampers. Considering rotary MR dampers have the merits of low sealing requirements and lower costs, Sun *et al.* [18] firstly applied a rotary MR damper to the seat suspension for heavy-duty vehicles. As illustrated in **Figure 2.21**, the proposed MR damper was installed at the scissors' intersection beams to provide the damping force for the seat suspension. Utilising a fuzzy control, both the numerical and the experimental results demonstrated that the semi-active seat suspension significantly attenuated the vibration under harmonic and random excitations.

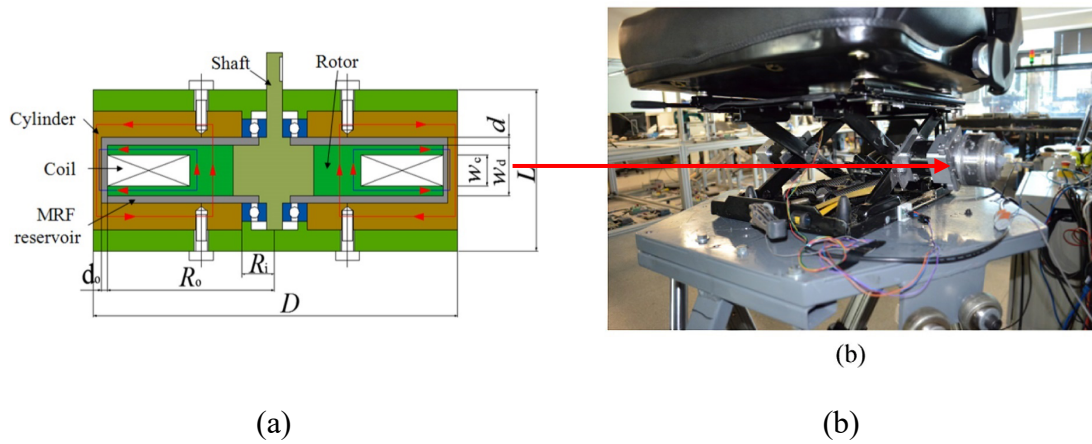


Figure 2.21. Structure of an MR seat suspension. (a) rotary MR damper (b) seat suspension. [18]

Sun *et al.* [116] also developed an MR seat suspension with self-powered generation capability using an MR damper and an EMI device as illustrated in **Figure 2.22**. The MR damper can control the seat suspension's damping, while the EMI device is responsible for harvesting the vibration energy and powering the MR damper. With this arrangement, no external power is required to control the MR damper, and the seat suspension is more cost-efficient.

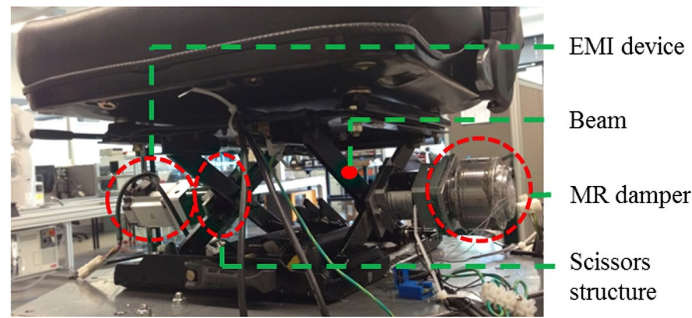


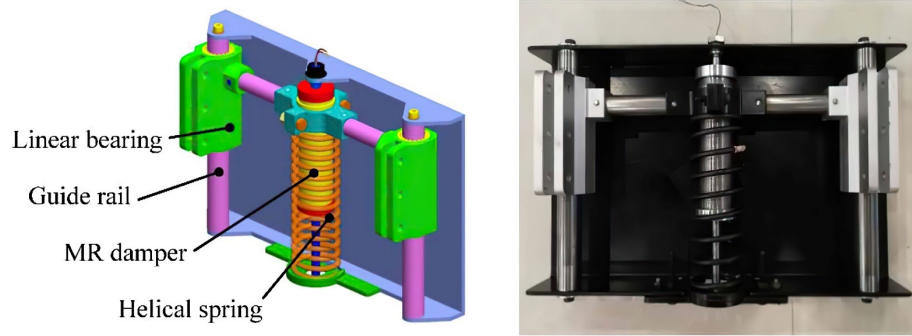
Figure 2.22. Structural schematic of a self-powered MR seat suspension [116]

## 2.5 Impact protection of seat suspension

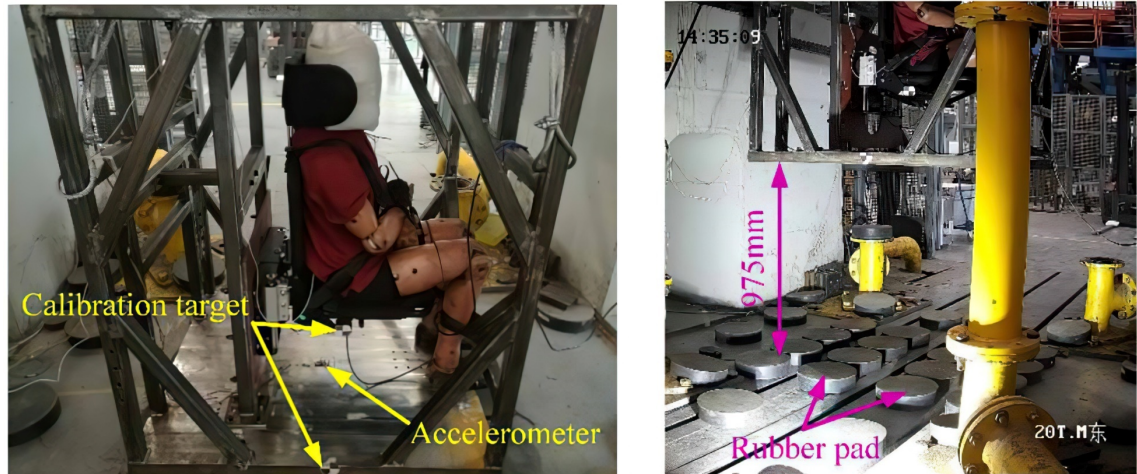
Apart from the vibration introduced in the last section, impacts such as the off-road induced shock for heavy-duty vehicles, the landmine blast-induced shock for military vehicles and the harsh- or crash-landings for helicopters may also cause severe injuries such as spinal fracture or health problems to occupants. Therefore, the high impact protection capability is also an important design requirement besides vibration control performance for seat suspensions.

With the merits of fast response, large damping force variation range, and low power consumption, magnetorheological (MR) dampers have been utilised for semi-active seat suspension on impact protection. McManus *et al.* [112] compared the end-stop impact protection and the vibration attenuation performance of a seat equipped with an MR damper with a seat installed with a conventional damper. Choi and Wereley studied the biodynamic response of an MR-damper helicopter crew seat to shock loads due to a vertical crash landing [20], and investigated an MR-damper military seat suspension subjected to vibratory and blast-induced shock loads [21]. In order to enhance the crashworthiness of an MR damper helicopter seat suspension, Hiemenz *et al.* [113] developed a load-limiting control algorithm that can automatically adjust the constant stroking load according to the crew weight. Singh and Wereley [117] investigated the effects of compliance of an occupant seated in an MR helicopter crew seat and exposed to intense vertical shocks. Bai and Wereley [118] investigated the frontal crash mitigation for ground vehicles with a semi-active MR damper seat suspension installed to improve both ride comfort and vertical safety of the driver. In addition, Bai and Yang [119] built a hybrid controller that incorporated a skyhook control strategy to realise vibration control and a ‘soft-landing’ control strategy for an MR energy absorber based semi-active seat suspension system to achieve shock control. As demonstrated in **Figure 2.23**, Jiang *et al.* [120] developed an MR seat suspension for

military vehicles. Apart from simulation, a systematic experiment of the prototyped seat suspension with a 50th percentile male hybrid III dummy are also conducted. Both the simulation and the systematic experiment indicated that the proposed MR seat suspension can provide favourable vibration reduction performance and impact resistance.



(a) Structural schematic of the MR seat suspension



(b) Impact experiment of seat suspension with a 50th percentile male hybrid III dummy.

Figure 2.23. An MR seat suspension for military vehicles. [120]

## 2.6 Conclusion

This chapter reviewed the current development of magnetorheological technology and its applications on robotic arms and seat suspensions. The background of MRFs and MR dampers was presented. One specific kind of MR dampers with the capability of variable damping and stiffness was introduced in detail. On the application of robotic arms, approaches include advanced controller design and MR dampers structural involvement for improving the positioning control performance were reviewed. On the

other application of seat suspension, cutting-edge technologies to achieve vibration control and impact protection were introduced, respectively.

## Chapter 3

### Design, testing and modelling of a rotary variable damping and stiffness magnetorheological damper

#### 3.1 Introduction

With the development of the magnetorheological damper, magnetorheological dampers capable of variable damping have been widely applied to attenuate vibration [13, 70, 71, 121-124]. In the vibration control system, the quantity of vibration energy dissipated in a system could be controlled by adjusting the damping, such that the vibration magnitude would be reduced. In addition, vibrations could also be suppressed by varying the system's stiffness, as it can shift the resonant frequency of the system away from a given excitation frequency. Linear MR dampers with the capability of variable damping and stiffness have been developed [14-16, 79], with the rotary MR dampers with similar characteristics rarely reported. Considering the importance of both the stiffness variability and the damping variability and the possible applications in angular rotation movement, a new rotary MR damper capable of simultaneously controlling its damping and stiffness was designed, manufactured, modelled and tested.

The proposed novel rotary MR damper assembled a set of two magnetorheological (MR) damping units, one of which being placed in series with a rubber spring. This allows the damping and stiffness to be controlled independently by the internal damping and the external damping units, respectively. Following the Introduction, the mechanical structure design, working principle and magnetic field simulation of the proposed VSVD damper are presented in Section 3.2. Then, its feature of variable damping and stiffness is verified by experimental tests in Section 3.3. To describe the behaviour of the VSVD damper, Section 3.4 provides its mathematic model and corresponding parameters identification. Finally, a conclusion is drawn in Section 3.5.

#### 3.2 Structural design and analysis of the VSVD rotary damper

##### 3.2.1 The structure of the MR VSVD rotary damper

As shown in **Figure 3.1**, the proposed VSVD damper consists of a set of two damper structures: a drum-type internal damper, and a disk-type external damper. The shaft is connected to the internal damper rotor and the plate. A motor can be mounted to



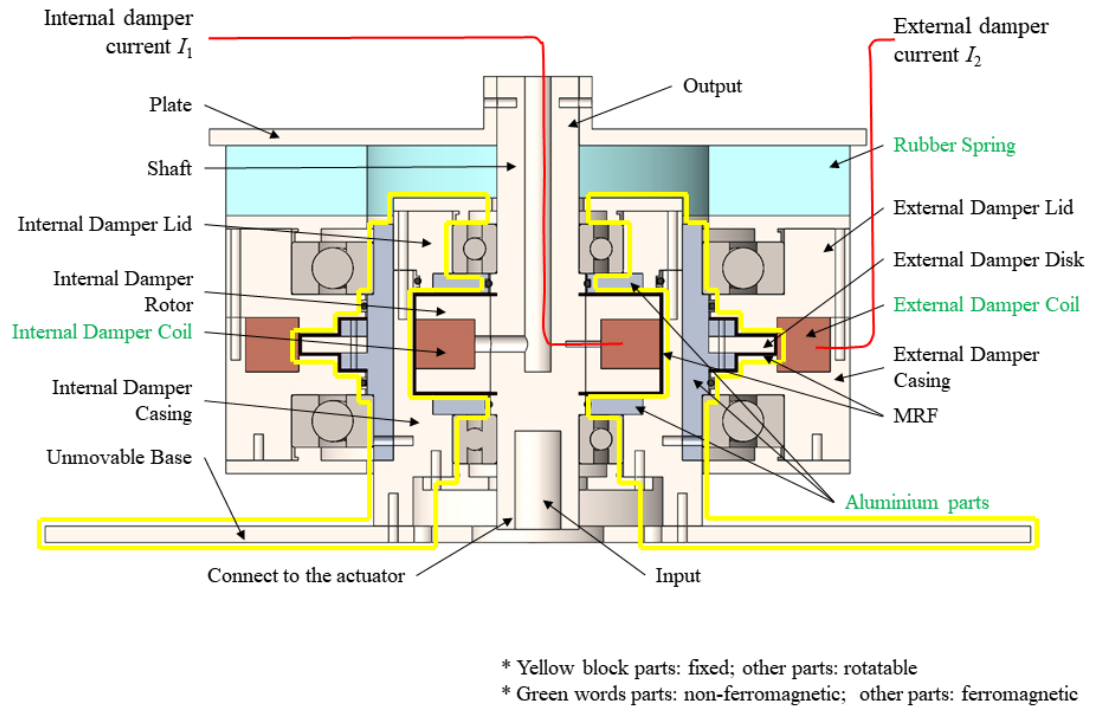


Figure 3.1. Variable stiffness and damping rotary MR damper structure

the base to drive the proposed damper from the bottom, with the plate on the top serving as the output. A cylindrical rubber spring made of silicone rubber (M4601A/B, Barnes corp.) is mounted between the plate and the external damper casing. As the internal damper casing is connected to the unmovable (fixed) plate and the external damper disk, both the internal damper casing and the external damper disk keep still while the internal damper rotor and the external damper casing may spin, following the shaft. Basically, all the parts in the yellow block are fixed and cannot rotate, while other parts are able to rotate following the shaft. Magnetorheological fluid (MRF-122EG, Lord corp.) is filled in the two 0.8 mm gap chambers of both internal and external dampers. The internal damper coil is seated in the internal damper rotor, while the external damper coil is mounted to the external damper casing. Both of these two coils can generate magnetic flux to control the yield stress of the MR fluids contained inside. Here, internal damper current and external damper current are assigned as  $I_1$  and  $I_2$ , respectively. In order to optimise the magnetic flux path, the part connecting the internal and the external damper was made of aluminium 7075 with a low magnetic permeability while other parts are made of low carbon steel with high magnetic permeability. In addition, aluminium was also used for both the internal damper lid and the casing to guide the magnetic flux to pass through MRF gap for the purpose of realising a high magnetic flux density across MRF working area. As shown in **Figure**

**3.1**, the captions of the rubber spring, the internal and the external damper coil, and the aluminium parts are in green, indicating non-ferromagnetic, while other parts with black caption are ferromagnetic and made of low carbon steel 1020. The VSVD damper has a axial height of 120 mm and a radial diameter of 190 mm.

### 3.2.2 Working principle

If no current is applied to both the internal damper coil and the external damper coil, all the parts except the ones in the yellow block in **Figure 3.1**: the internal damper rotor, the plate, the rubber spring, and the external damper casing can rotate freely with the shaft. The rubber spring will only experience a small strain due to the inertial torque of the external damper. By providing current  $I_1$  to the internal damper coil, variable damping is realised, with the relative movement between the internal damper rotor and the casing restrained by the semi-solid MR fluid between them. If even a small current  $I_2$  is given to the external damper coil, the external damper casing would not be able to freely rotate from the external damper disk, due to the braking torque induced by the MR fluid. However, the plate is able to always move simultaneously with the shaft. As a result, the rubber spring would be stretched, which largely increases the stiffness of the entire device. As such, damping variability is achieved through the regulation of the internal damper current  $I_1$ , while the external damper current  $I_2$  can control the stiffness of the device.

### 3.2.3 Magnetic field simulation

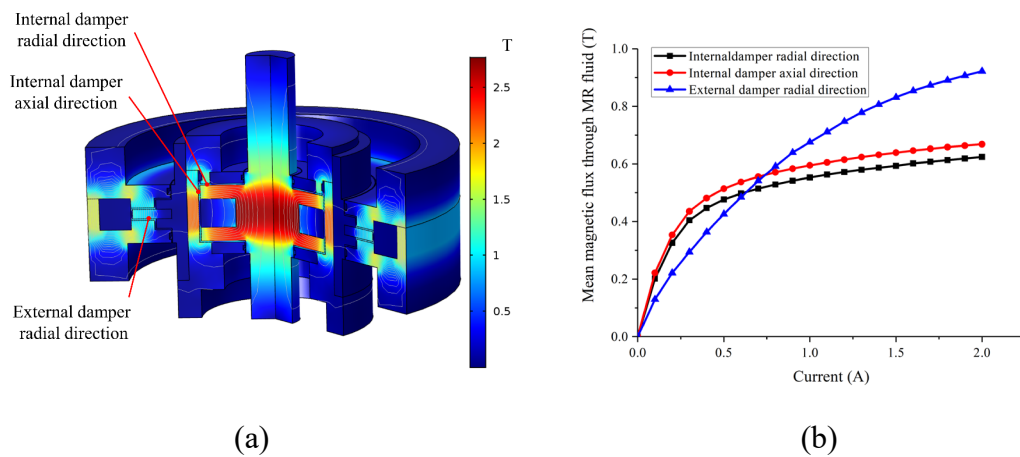


Figure 3.2. Magnetic field simulation: (a) modelled damper, and (b) average flux through the MRF for varied currents

In order to provide guidance to the damper design, the induced magnetic field of the proposed damper was simulated using COMSOL Multiphysics with a 2D



axisymmetric study, with the results being shown in **Figure 3.2(a)**. The internal damper coil has 500 turns with 0.5 mm diameter and 7.8  $\Omega$  resistance copper wire, while the external damper coil has 200 turns with 0.5 mm diameter, 10.9  $\Omega$  resistance copper wire. **Figure 3.2(a)**, it can be noticed that the aluminium part connecting the external damper disk and the internal damper casing effectively builds a barrier between the internal magnetic circulation and the external magnetic circulation, so the magnetic field interference between the two damping units is minimised. For the same reason, additional aluminium parts were added to the internal damper to guide the magnetic flux where desired. Thus, the magnetic flux of each can be separately controlled by the internal current  $I_1$  and external current  $I_2$ , without mutual interference.

For the internal damper, the working area of the MR fluid is on the upper and lower gaps (i.e. the surfaces in the radial direction) and the small gaps between the drum and the internal damper casing (in the axial direction). As for the external damper, the upper and lower gaps between the disk and the casing (in the radial direction) serve as the working area. Thus, the relationship between the mean magnetic flux in these working areas and the current is plotted in **Figure 3.2(b)**. The magnetic flux of the MR fluid in both the internal damper and external damper increase continuously with the increasing current. The maximum mean flux of the external damper was found to be 0.918 T at 2.0 A. Given this appears sufficient for the MR fluid selected, the current range of 0~2.0 A was set for the external damper coil. In contrast, the magnetic flux of the internal damper shows saturation when current above 0.6 A, with the maximum mean fluxes at 1.0 A being 0.552 and 0.594 T for the radial and axial directions, respectively. As a result, the current range of 0 ~ 1.0 A was chosen to be used in the tests of the internal damper coil.

### 3.3 Experimental testings and analysis

#### 3.3.1 Experiment setup for property test

In order to verify the variable damping and stiffness features of the designed rotary MR damper, a test system was established to characterise the device. As it is shown in **Figure 3.3**, the device is mounted on an unmovable base connecting to the test bench frame. The damper is driven by an AC servomotor and drive system (Panasonic 1.3 N·m, MBDKT2510CA1 200 V) with a 40:1 planetary gearbox (After ATF 60S-40). This servomotor is controlled using an NI myRIO to provide the position control signal, through a LabVIEW program prepared for this testing. The myRIO is also connected to

a PC to provide the user interface for testing. When running the tests, the measured signals including displacement and torque, are recorded by the myRIO, serving as both the controller and the data acquisition (DAQ) device. In addition, a DC power supply (GW INSTEK GPC – 3030D) is used to provide currents at different levels to both the internal damper coil and external damper coil.

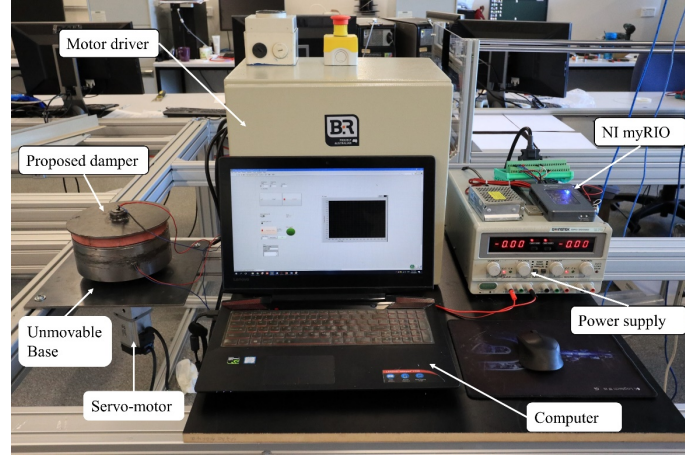


Figure 3.3. Schematic diagram for the experimental setup

The testing cases consist of damping variability and stiffness variability. For each case, sufficient tests were measured in order to ensure performance stability and uniformity. As the damping variability is controlled by the internal damper current  $I_1$ , the external damper current  $I_2$  was set as 0 A in the damping variability test case. Similarly, for the stiffness variability test cases, the internal damper current  $I_1$  was set as 0 A. The test input is selected as the sinusoidal signal  $\varphi = A \sin(2\pi ft)$  to characterise both the damping and the stiffness of the device.  $\varphi$ ,  $A$ ,  $f$  and  $t$  represent the angular displacement, amplitude, frequency and time, respectively. At the same time, the signals of displacement and the torque generated on the shaft were recorded through the motor driver. In addition, the co-working of the internal and external damping units were also conducted to further characterise the behaviour of the device.

### 3.3.2 Testing results and analysis

#### 3.3.2.1 Damping variability

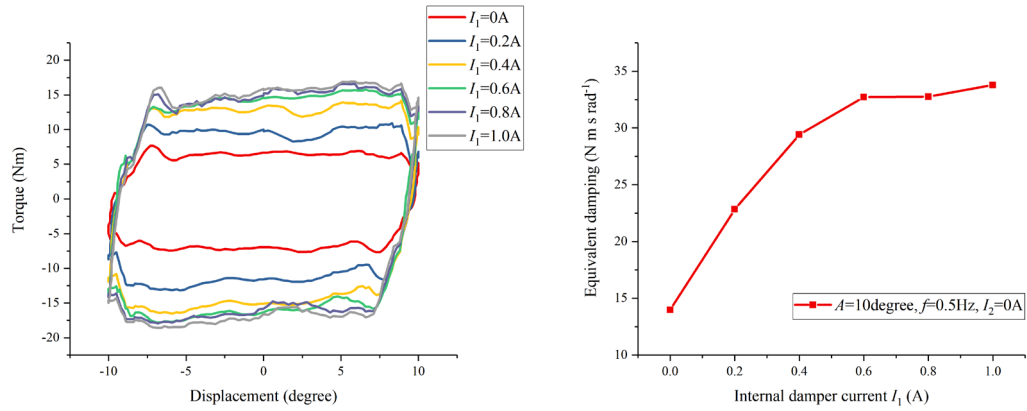
##### *Current dependent response*

**Figure 3.4** shows the damping variability in response to various internal damper currents:  $I_1 = 0, 0.2, 0.4, 0.6, 0.8$  and  $1.0$  A, along with an amplitude  $A = 10$  degree, frequency  $f = 0.5$  Hz external damper current  $I_2 = 0$  A. The calculated equivalent damping coefficient as plotted in **Figure 3.4(b)** was found using the following equation

[125]:

$$C_{t,eq} = \frac{EDC}{2\pi^2 f A^2} \quad (3-1)$$

where  $C_{t,eq}$  is the equivalent damping coefficient, EDC is the energy dissipated per cycle, being the enclosed area of each torque-displacement loop,  $f$  is the sinusoidal frequency in Hz, and  $A$  is the sinusoidal amplitude.



(a) Torque-displacement relation ( $A = 10$  degree,  $f = 0.5$  Hz,  $I_2 = 0$  A) (b) Equivalent damping coefficient to internal currents  $I_1$

Figure 3.4. Variable damping behaviour under varied internal damper current  $I_1$

As shown in **Figure 3.4(a)**, the enclosed area of torque-displacement loops, EDC, increases with the increase of the internal damper current  $I_1$  from 0 to 1.0 A. The calculated equivalent damping coefficient in **Figure 3.4(b)** increases proportionally with all other variables held constant. This equivalent damping showed an increase of 141.6% from 13.98 to 33.78 N.m.s.rad<sup>-1</sup> with the increase of current from 0 to 1.0 A. The peak torque, shown in **Figure 3.4**, begins to saturate when the applied current is larger than 0.6 A, which is consistent with the magnetic field saturation phenomenon in the magnetic field studies conducted, as shown in **Figure 3.2**.

#### *Amplitude dependent response*

The amplitude-dependent response of the damping variability at three amplitudes:  $A = 5, 10$  and  $15$  degree under the combined conditions of internal damper current  $I_1 = 1.0$  A, frequency  $f = 0.5$  Hz and external damper current  $I_2 = 0$  A is illustrated in **Figure 3.5(a)**. The peak torque is almost the same for all the amplitude cases. Even though the energy dissipated in each loop, EDC, increases with the increasing current, the equivalent damping coefficient shows a decreasing trend in **Figure 3.5(b)** because the

equivalent damping coefficient is inversely proportional to the square of the amplitude, as shown in **Equation (3-1)**.

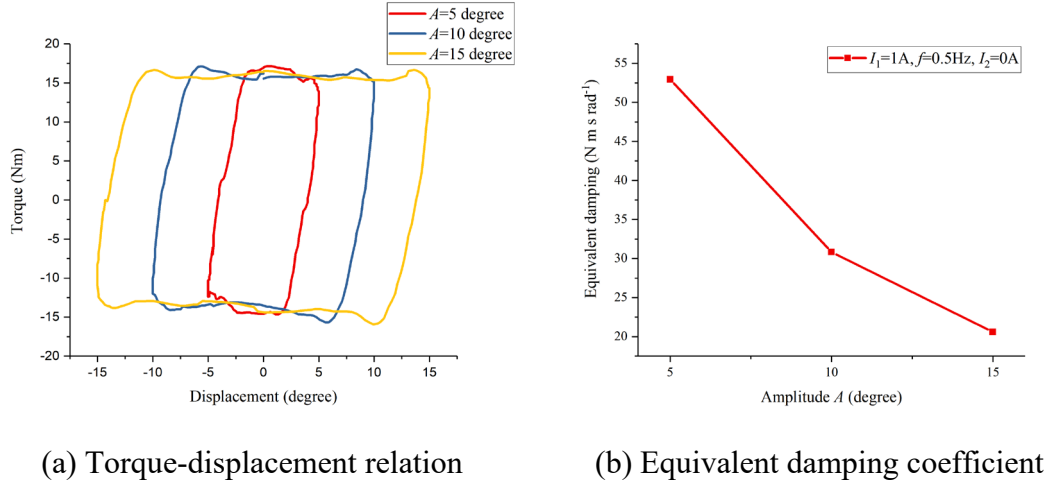


Figure 3.5. Response to different amplitudes ( $I_1 = 1.0\text{ A}$ ,  $f = 0.5\text{ Hz}$ ,  $I_2 = 0\text{ A}$ )

#### Frequency dependent response

**Figure 3.6** shows the response of the MR damper under the various loading frequencies:  $f = 0.5, 0.75$  and  $1.0\text{ Hz}$ , with the combined conditions of amplitude  $A = 10$  degree, internal damper current  $I_1 = 0.5\text{ A}$  and external damper current  $I_2 = 0\text{ A}$ . It is noticed that the peak torque of the enclosed area, EDC, is almost the same at three frequencies for all test cases. However, as it is indicated in **Figure 3.6(b)**, the equivalent damping coefficient is decreasing with the increase of frequency  $f$  because the equivalent damping coefficient is inversely proportional to this.

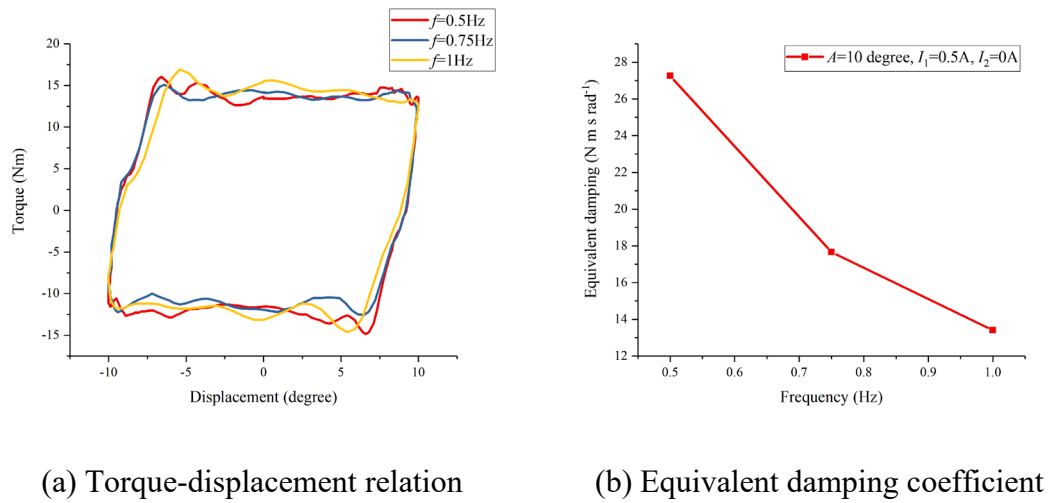


Figure 3.6. Response to different frequencies ( $A = 10$  degree,  $I_1 = 0.5\text{ A}$ ,  $I_2 = 0\text{ A}$ )

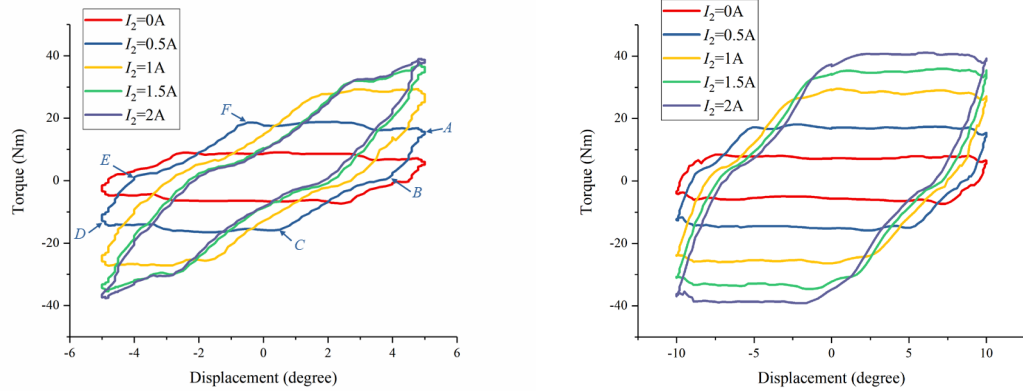
### 3.3.2.2 Stiffness variability

In this section, the stiffness variability of the designed damper is tested. Effective stiffness was calculated for all the test cases using the equation [125]:

$$K_{\text{eff}} = \frac{T_{d,\text{max}} - T_{d,\text{min}}}{A_{\text{max}} - A_{\text{min}}} \quad (3-2)$$

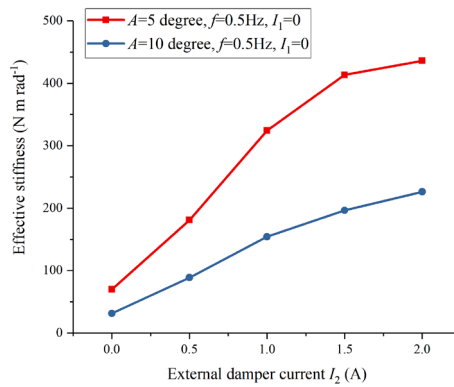
where  $T_{d,\text{max}}$  and  $T_{d,\text{min}}$  are the maximum and minimum torques at the maximum and the minimum amplitude displacements,  $A_{\text{max}}$  and  $A_{\text{min}}$ , respectively.

#### *Current dependent response*



(a) Torque-displacement relation at small amplitude  $A = 5$  degree ( $f = 0.5$  Hz,  $I_1 = 0$ )      (b) Torque-displacement relation at large amplitude  $A = 10$  degree ( $f = 0.5$  Hz,  $I_1 = 0$ )

A) A)



(c) Effective stiffness response for amplitude conditions:  $A = 5$  degree and 10 degree

Figure 3.7. Variable stiffness under the varied external damping current  $I_2$

**Figure 3.7** presents the stiffness variability of the damper under different levels of external damper current:  $I_2 = 0, 0.5, 1.0, 1.5$  and  $2.0$  A. Two sets of combined conditions: ' $A = 5$  degree,  $f = 0.5$  Hz,  $I_1 = 0$  A' and ' $A = 10$  degree,  $f = 0.5$  Hz,  $I_1 = 0$  A'

were selected to illustrate the current dependent behaviour for varied amplitudes.

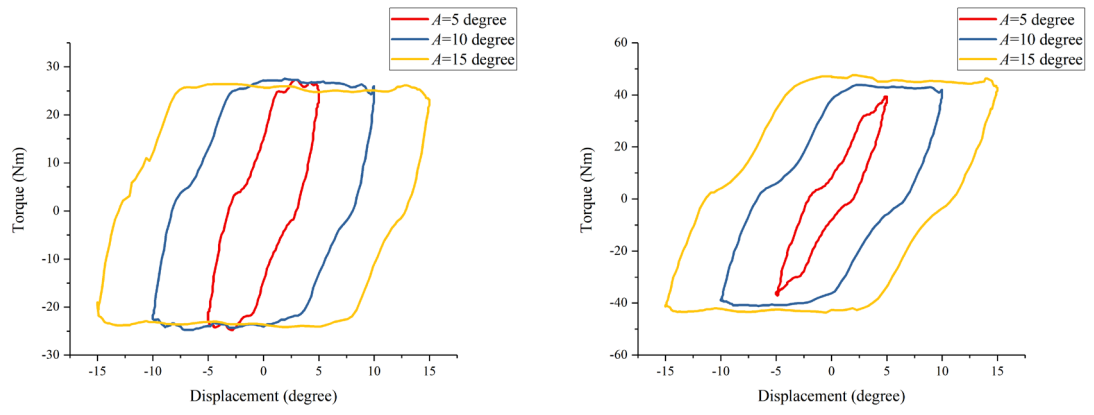
As shown in **Figure 3.7(a) and (b)**, the torque follows piecewise behaviour in response to a displacement input, with these loops being generated in a clockwise direction. Taking the test case of ' $A = 5$  degree,  $f = 0.5$  Hz,  $I_1 = 0$  A,  $I_2 = 0$  A' in **Figure 3.7(a)** as an example, letters are placed about the figure at its vertices in a clockwise direction, starting with A at the maximum positive amplitude. Considering loading for  $A \rightarrow D$ , starting with the section of AB, a torque is generated as the torque from the actuator overcomes the initial damping of the internal damper in order to allow the shaft to rotate. Then, focusing on section BC, if a current  $I_2$  is applied to the external damper coil, this tends to stretch the rubber, through the engagement of the external damper. As the motor continues to actuate the device, the spring becomes loaded, with its stiffness defining the slope of section BC. After the point at which the spring torque exceeds the braking torque of the external damper, occurring at some displacement level, the rubber spring will stop stretching further and the external casing will move together with the plate without relative motion. This process describes the loop segment of CD, which is almost parallel to the x-axis, at which stage the stiffness in this process could be regarded as zero. The reverse process represented by  $D \rightarrow A$  is symmetrical to the regular process  $A \rightarrow D$ , as the segments of DE, EF and FA are parallel to the segments of AB, BC and CD, respectively. It should also be noted that in **Figure 3.7(a)**, the segments CD and FA tend to reduce in size until they are non-existent when the current is high enough. This is due to the external damper tending to not yield as damping torque becomes relatively large when compared to the spring torque. In contrast, under the  $A = 10$  degree amplitude, no level of current tested is sufficient to prevent such yielding.

The effective stiffness of the damper is shown in **Figure 3.7(c)**, as calculated using **Equation. (3-2)**, which is simply the slope of the line AD. As illustrated, the stiffness of the designed damper increases with the increase of the external damper current  $I_2$  for both test cases: ' $A = 5$  degree,  $f = 0.5$  Hz,  $I_1 = 0$  A' and ' $A = 10$  degree,  $f = 0.5$  Hz,  $I_1 = 0$  A'. For the smaller amplitude  $A = 5$  degree condition, the stiffness is increased 524% from 69.88 to 436.02 N·m·rad<sup>-1</sup> as the current is increased from 0 A to 2 A. In the case of  $A = 10$  degree, a 618.1% increase of effective stiffness from 31.51 to 226.26 N·m·rad<sup>-1</sup> was achieved. The effective stiffness for the smaller amplitude  $A = 5$  degree is larger than that of the  $A = 10$  degree condition in general. This is simply due to the

stiffness being an average across the entire displacement of the device, which includes more ‘zero-stiffness’ yielding of the external damper as displacement amplitude increases.

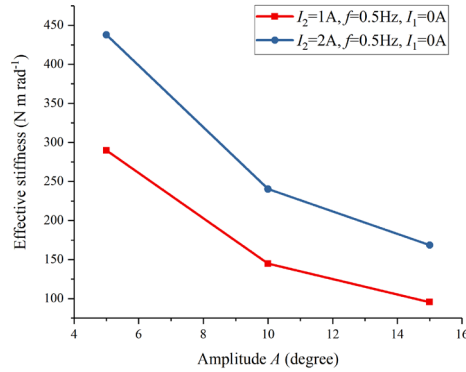
#### *Amplitude dependent response*

**Figure 3.8** illustrates the amplitude dependency of the damper for the three amplitude conditions  $A = 5, 10$  and  $15$  degree. The results of two sets of the combined conditions: ‘ $I_2 = 1$  A,  $f = 0.5$  Hz,  $I_1 = 0$  A’ and ‘ $I_2 = 2$  A,  $f = 0.5$  Hz,  $I_1 = 0$  A’ are presented.



(a) Torque-displacement relation at small current  $I_2 = 1$  A ( $f = 0.5$  Hz,  $I_1 = 0$  A)

(b) Torque-displacement relation at big current  $I_2 = 2$  A ( $f = 0.5$  Hz,  $I_1 = 0$  A)



(c) Amplitude response of effective stiffness at current conditions:  $I_2 = 1$  A and 2 A

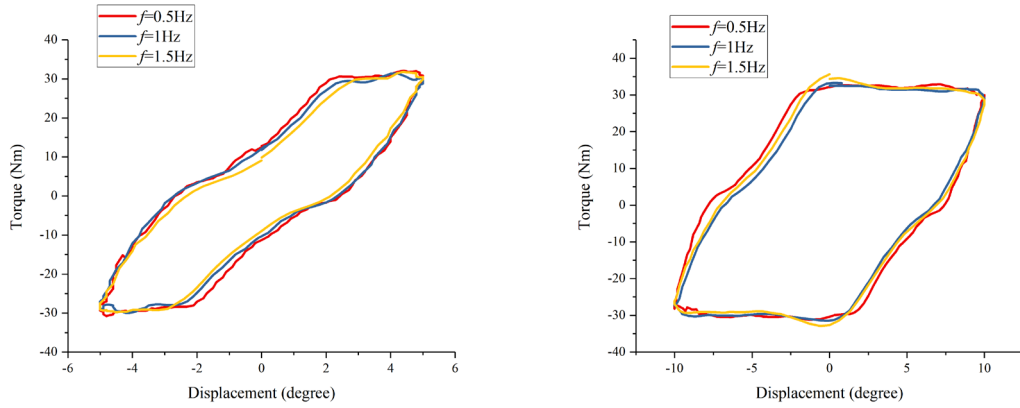
Figure 3.8. Stiffness response to various amplitudes

In **Figure 3.8(a)**, the external damper is yielded for all the amplitude cases at the lower current  $I_2 = 1$  A. The damping torque generated by the low current  $I_2 = 1$  A is not sufficient to prevent yielding even for the smallest amplitude  $A = 5$  degree. In contrast, as shown in **Figure 3.8(b)**, the external damper is not yielded for the amplitude  $A = 5$

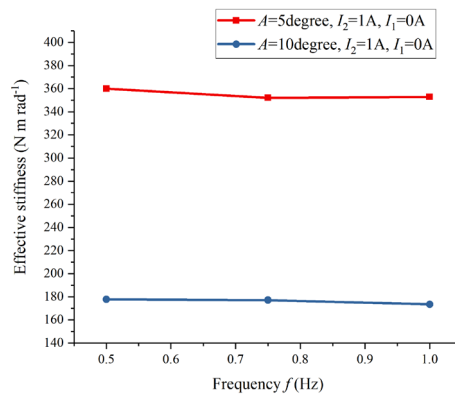
degree case when a higher current  $I_2 = 2$  A is applied until the amplitude increased to  $A = 10$  degree. Consequently, the maximum torque of the amplitude  $A = 5$  degree is slightly smaller than that of  $A = 7.5$  and  $10$  degree, as in this case the constant yielding torque of the damper was not reached by the spring for this given external damper current and test frequency.

The effective stiffness for these tests are illustrated in **Figure 3.8(c)**, which reveals a declining trend with increasing amplitude. Under a constant amplitude, because the maximum torque of the larger external damper current condition  $I_2 = 2$  A is larger than that of the smaller current condition  $I_2 = 1$  A, the effective stiffness of the large current conditions are larger than that of the smaller current conditions.

#### *Frequency dependent response*



(a) Torque-displacement relation at small amplitude  $A = 5$  degree ( $I_2 = 1$  A,  $I_1 = 0$  A) (b) Torque-displacement relation at big amplitude  $A = 10$  degree ( $I_2 = 1$  A,  $I_1 = 0$  A)



(c) Frequency response of effective stiffness at two amplitude conditions:  $A = 5$  degree and  $10$  degree

Figure 3.9. Stiffness response to various frequency



**Figure 3.9** provides the frequency-dependent response of the proposed damper. Three frequencies  $f = 0.5, 0.75$  and  $1.0$  Hz are prescribed for the test cases of ' $I_2 = 1$  A,  $A = 5$  degree,  $I_1 = 0$  A' and ' $I_2 = 1$  A,  $A = 10$  degree,  $I_1 = 0$  A'. Relative movement between the external damper casing and external damper disk exists at both amplitude conditions. The torque-displacement loops are almost the same at the three frequency conditions for both the smaller and larger amplitude test cases. Thus, the effective stiffness is also almost the same for all the frequency conditions, as illustrated in **Figure 3.9(c)**.

### 3.3.2.3 Simultaneous working of internal and external damping units

**Figure 3.10** presents the test results when the internal damper unit and external damper unit work together. The external damper current  $I_2$  is set as 0 and 2 A for two groups of test separately. In each group, internal damper current  $I_1$  is applied with three levels of currents: 0, 0.5 and 1 A. When the external damper current  $I_2 = 2$  A, the maximum torque shows an increase from 42.3 to 52.08 Nm as the internal damper current  $I_1$  increases from 0 to 1 A. This increasing trend is quite similar to that of the reference group in which the external damper current  $I_2 = 0$  A.

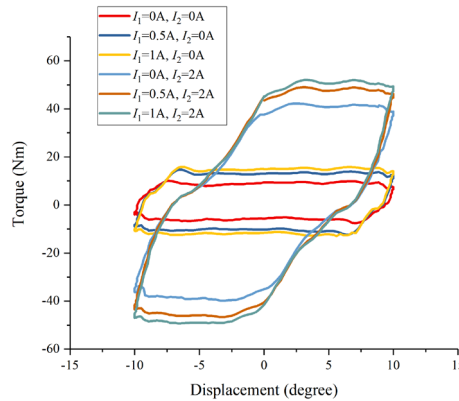


Figure 3.10. Simultaneously working for internal and external damping units

## 3.4 Modelling and parameter identification

In order to predict the variable damping and stiffness behaviour of the designed MR damper, a mathematical model is established in this section. The parameters for both the internal damping unit and the external damping unit were also identified as followed.

### 3.4.1 Model establishment

As it is shown in **Figure 3.11**, a mathematical model which incorporates two

Bingham components [126] is built to predict the damping and the stiffness variation of the designed MR damper. A coulomb friction element  $T_1$  in parallel with a dashpot with viscous damping coefficient  $c_1$  is used to describe the internal MR damper unit. Similarly, the external damper unit is characterised by another coulomb friction element  $T_2$  in parallel with a dashpot with viscous damping coefficient  $c_2$ . In addition, a stiffness  $k_r$  represents that of the rubber spring. For these parameters,  $T_1$  and  $c_1$  are controlled by the applied current to the internal damper  $I_1$ , while  $T_2$  and  $c_2$  vary in value due to the change of external damper current  $I_2$ . The angular displacements of the shaft or plate and the external damper casing are prescribed as  $\phi_1$  and  $\phi_2$ , respectively.

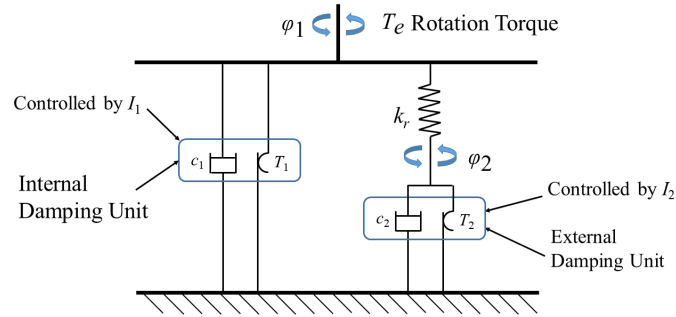


Figure 3.11. Mathematic model of the proposed rotary MR damper

The rotation torque  $T_e$  can be written as

$$T_e = T_{in} + T_r \quad (3-3)$$

$$T_{in} = c_1 \dot{\phi}_1 + T_1 \text{sign}(\dot{\phi}_1) \quad (3-4)$$

$$T_r = k_r (\phi_1 - \phi_2) \quad (3-5)$$

where  $T_{in}$  is the torque generated by the internal damper, and  $T_r$  represents the rubber spring torque. The external damper torque can be calculated by

$$T_{ex} = c_2 \dot{\phi}_2 + T_2 \text{sign}(\dot{\phi}_2) \quad (3-6)$$

The damper torques  $T_{in}$  and  $T_{ex}$  increase with the increase of currents  $I_1$  and  $I_2$ , respectively. As illustrated of the segment BC and EF in **Figure 3.7(a)**, during the loading of the rubber, the external damper casing keeps still. After the external damper torque yields due to that of the rubber, the external damper casing would move simultaneously with the plate without relative movement until the shaft reaches the minimum or maximum displacement. This process is represented by the segments of FA

and CD in **Figure 3.7(a)**. The torque of the rubber spring then stops increasing as the rubber elongation becomes constant. Thus,

If  $|T_r| < |T_{ex}|$

$$\dot{\phi}_2 = 0 \quad (3-7)$$

elseif  $|T_r| = |T_{ex}|$

$$\dot{\phi}_2 = \dot{\phi}_1 \quad (3-8)$$

### 3.4.2 Model establishment

After building the model of the system, four parameters in the model:  $c_1$ ,  $T_1$ ,  $c_2$ ,  $T_2$  should be identified using the experimental data to predict the behaviour of the device. The procedure follows the least-square method in combination with the trust-region-reflective algorithm which is available in MATLAB & Simulink. The goal of this method is to minimise the difference between the modelled results to the experimental results by adjusting the four parameters as shown in the following equation:

$$S = \sum_N^{i=1} \sqrt{\frac{(T_{ei} - T_{mi})^2}{N}} \quad (3-9)$$

where the  $S$  is the root mean square between the predicted and the experimental results,  $T_{ei}$  and  $T_{mi}$  are the  $i^{\text{th}}$  experimental torque and the modelled torque, and  $N$  is a neighbourhood which is defined as the trust region that could represent the behaviour of **Equation (3-9)**. Obviously, by using this method, the model results will be approximate the experimental results to the greatest degree only if  $S$  reaches its minimum value.

Table 3.1. Parameter identification results for the variable damping (the left half) and variable stiffness (the right half) at the conditions:  $A = 10$  degree and  $f = 0.5$  Hz

Parameter (variable damping)	$T_1$	$c_1$	$T_2$	$c_2$	Parameter (variable stiffness)	$T_1$	$c_1$	$T_2$	$c_2$
$I_1 = 0$ A, $I_2 = 0$ A	2.8	0.8	3.8	1.8	$I_1 = 0$ A, $I_2 = 0$ A	2.8	0.8	3.8	1.8
$I_1 = 0.5$ A, $I_2 = 0$ A	8.5	1.5	3.8	1.8	$I_1 = 0$ A, $I_2 = 1$ A	2.8	0.8	21.7	4.2
$I_1 = 1$ A, $I_2 = 0$ A	11.2	2.2	3.8	1.8	$I_1 = 0$ A, $I_2 = 2$ A	2.8	0.8	35.6	5.8

As the damping variability and the stiffness variability are separately controlled by the internal damper current  $I_1$  and the external damper current  $I_2$ , the internal damper parameters  $c_1$ ,  $T_1$  at different currents are identified with the fixed external damper parameters  $c_2$  and  $T_2$  for the damping variable part, and vice versa. Adopting the experimental data of variable damping tests:  $A = 10$  degree,  $f = 0.5$  Hz,  $I_1 = 0, 0.5$  and  $1$  A, and the data of variable stiffness tests:  $A = 10$  degree,  $f = 0.5$  Hz,  $I_2 = 0, 1$  and  $2$  A, the parameters are identified using the built model in the Simulink as shown in **Table 3.1**. The modelled results compared with the experiment results are also shown in **Figures 3.12 and 3.13**.

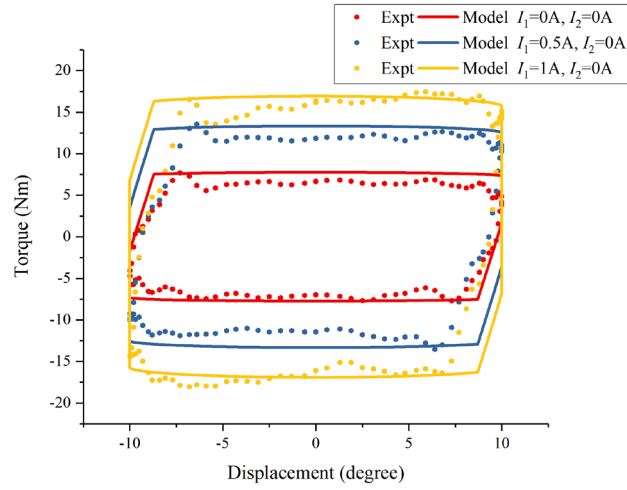


Figure 3.12. Modelled results compare to the experiment results of the variable damping tests ( $A = 10$  degree,  $f = 0.5$ Hz)

As illustrated in the left half part of **Table 3.1**, the external damper parameters  $T_1$  and  $c_1$  increase with an increasing internal damper current  $I_1$ , while  $T_2$  and  $c_2$  are constant with the constant zero external damper current  $I_2$ . Plotting the simulated result against the experimental result, the modelled variable damping behaviour in **Figure 3.12** shows a good fit with the experimental data at various levels of  $I_1$ . For the modelled results, the area enclosed by the torque-displacement loop increases with the increasing current, which predicts the variable damping ability very well. The parameters of the external damper,  $T_2$  and  $c_2$ , also show a positive relationship with the increase of  $I_2$ . At the same time, the internal damper parameters  $T_1$  and  $c_1$  do not change for the fixed  $I_1$ . The variable stiffness capability is also well modelled for the effective stiffness increases with the increasing of  $I_2$ , as shown in **Figure 3.13**.

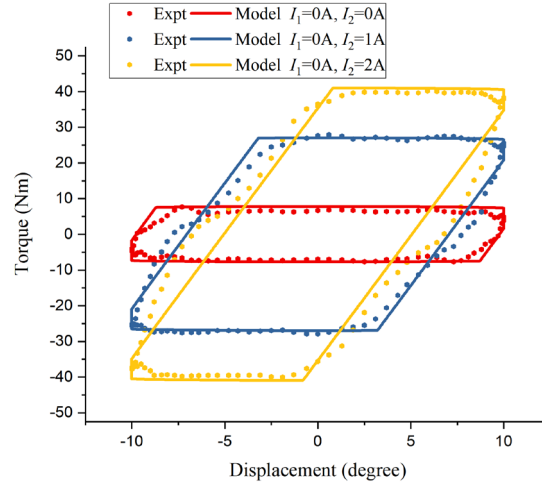


Figure 3.13. Modelled results compare to the experiment results of the variable stiffness tests ( $A = 10$  degree,  $f = 0.5\text{Hz}$ )

To verify that the proposed model with the identified parameters could predict the behaviours of the device. Two modelled results for the conditions: ' $I_1 = 0.5$  A,  $I_2 = 1$  A' and ' $I_1 = 1$  A,  $I_2 = 2$  A' were plotted in **Figure 3.14** by using the parameters as shown in **Table 3.2**. The values of  $T_1$  and  $c_1$  are obtained from the cases with the same internal damper current  $I_1$  while the values of  $T_2$  and  $c_2$  are obtained from the cases with the same external damper current  $I_2$ . For instance, within the parameters for the modelled case ' $I_1 = 0.5$  A,  $I_2 = 1$  A', ' $T_1 = 8.5$ ,  $c_1 = 1.5$ ' and ' $T_2 = 21.7$ ,  $c_2 = 4.2$ ' are separately obtained from the corresponding parameters of the test cases of ' $I_1 = 0.5$  A,  $I_2 = 0$  A' and ' $I_1 = 0$  A,  $I_2 = 1$  A' as listed in **Table 3.1**. As it is shown in **Figure 3.14**, the modelled results have very good accordance to the experimental data, which means the proposed model with the parameters in **Table 3.2** could predict the behaviour of the device very well, facilitating future control efforts for such a device.

Table 3.2. Parameters used to verify the proposed model

Modelled cases	$T_1$	$c_1$	$T_2$	$c_2$
$I_1 = 0.5$ A, $I_2 = 1$ A	8.5	1.5	21.7	4.2
$I_1 = 1$ A, $I_2 = 2$ A	11.1	2.2	35.6	5.8

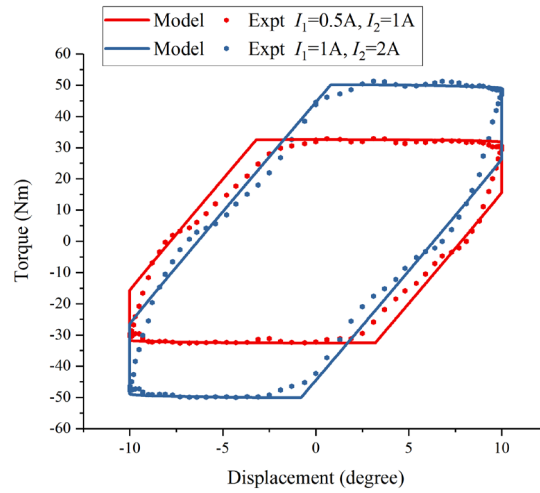


Figure 3.14. Verification of the proposed model under co-working conditions by comparing the modelled results to the experimental results ( $A = 10$  degree,  $f = 0.5$  Hz)

### 3.5 Conclusion

This chapter includes the design of a novel MR damper with variable damping and stiffness capabilities based on a rotary MR damper. Experimental tests were conducted to verify such performance, and the test results show that the damping increased 141.6% from 13.98 to 33.78 N.m.s.rad<sup>-1</sup> as the current is increased from 0 to 1.0 A with a 10 degree amplitude. In addition, a maximum of 618% increase of effective stiffness from 31.51 to 226.26 N·m·rad<sup>-1</sup> is achieved with the current shift from 0 to 2 A at the amplitude of 10 degree. The accuracy of the established mathematical model in predicting the variable damping and stiffness characteristics of the damper was also verified with the identified parameters of internal and external MR dampers.

## **Chapter 4**

### **Positioning control system of a robotic arm using a VSVD rotary damper**

#### **4.1 Introduction**

Positioning system controlling tool's movements during the manufacturing operations play an important role in industrial manufacturing processes such as machine tool movements, semiconductor manufacturing systems and robot controls. The insufficiently rigid connections, low stiffness elements and heavy loads cause problems of large overshoot and long time vibrations during settling, which have a severe impact on the performance of the positioning system and the whole manufacturing process. Two main methods to solve the overshoot and vibration problems are developing advanced controllers and incorporating positioning control systems with smart materials and structure. One is applying advanced controllers with an active control system using motors. Another one is utilising a semi-active control system based on magnetorheological dampers. Compared with active control, the semi-active control system has the merits of simple mechanical and electrical structure, less power consumption, good cost-efficiency and less power consumption. Hence, in this chapter, the positioning control performance of a robotic arm system installed with a variable stiffness and damping (VSVD) magnetorheological (MR) damper was investigated. The damper was modified based on the VSVD MR damper introduced in Chapter 3 with a new internal damper shaft&coils and new rubber to fit the robotic arm system.

The proposed VSVD damper can reduce the overshoot and vibrations during the settling time of the robotic arm system to improve its positioning performance. Furthermore, the energy consumption of the system can be reduced as well. The rest of this chapter is organised as follows. Section 4.2 presents the structure of the proposed positioning control system for the robotic arm and its working principle. Then, the positioning performance of the robotic arm system is evaluated numerically in Section 4.3. Experimental tests are also presented in Section 4.4 to evaluate the positioning performance. Finally, the conclusion is drawn in Section 4.5.

#### **4.2 The proposed positioning system of a robotic arm and its working principle**

As shown in **Figure 4.1**, the proposed positioning control system of a robotic arm

consists of mechanical components and electronic devices. The mechanical components include a robotic arm, a VSVD MR damper, an unmovable base and a gearbox with a gear ratio of 20:1. The robotic arm is made of aluminium extrusions with a 10 kg mass fixed to one end of it, representing a heavy load carried by the arm. Because the maximum output of the servo motor is only 1.3 Nm, a gearbox is installed between the motor and the unmovable base to amplify the torque output and drive the robotic arm. A VSVD damper modified based on the damper presented in Chapter 3 and reported in [127] was installed between the gearbox and the robotic arm. It has an internal damper to control the damping by regulating the internal damper current  $I_1$ , and an external damper to control stiffness by regulating the external damper  $I_2$ . As the mechanical structure, working principle, and experimental testing of the new damper are similar to the damper presented in Chapter 3, they are introduced in the Appendix to avoid repetitions. The electronic devices consist of a computer, a myRIO, an AC servo driver, a servo motor, and two amplifiers. The computer can communicate with myRIO via a Labview program. Torque commands can be passed to the servo motor through myRIO and the AC servo driver to drive the robotic arm. Current commands are also sent to the amplifiers for regulating the currents applied to the internal and external MR dampers, so as to control the damping and the stiffness of the VSVD damper. The servo motor has a built-in encoder that can record both real-time position and torque output feedback signals of the motor and send these signals to the computer.

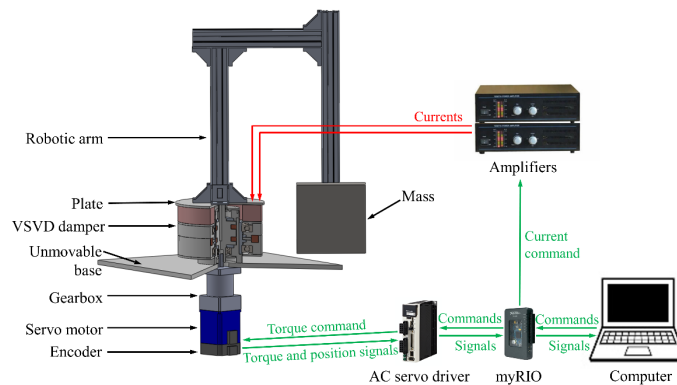


Figure 4.1. Positioning control system of the robotic arm

The control block diagram of the system is presented in **Figure 4.2**. For a conventional positioning control system, only the motor control unit that consists of a proportional-integral-derivative (PID) control and friction compensation is working. After a designed position signal is prescribed, the motor control unit will calculate the



real-time motor torque command for the servo motor based on the position error of the designed position signal and the real-time position feedback signal from the encoder. The motor torque is the sum of the calculated PID control output and the friction compensation output. Then the robotic arm is driven by the motor and the output torque acting on the arm is the motor torque only. In this control mode, the robotic arm is totally controlled by the motor alone. For the proposed control mode, a VSVD control unit also works in parallel apart from the motor control unit. The VSVD control unit can provide additional damper torque. In this case, the output torque acting on the arm is the combination of the motor torque and the damper torque. Therefore, the robotic arm is controlled by the motor unit and the VSVD control unit together. With the VSVD damper, additional damping and stiffness can be added to the system to realise a better positioning control performance. When the robotic arm working on the conditions of constant velocity or acceleration, small damping is required to ensure a fast response of the system. In contrast, large damping can help under the condition of deceleration. Besides, for a robotic arm carried with a heavy load, overshoot will happen when moving from one position and stop at another because of the inertia of the heavy load. In this case, large damping can be applied after the overshoot to reduce the amount of it. Moreover, large stiffness can also reduce overshoot because the system becomes stiffer. Large stiffness can save kinematics energy during the deceleration of the robotic arm and applied it to accelerate the robotic arm when required as well. During the constant-speed operation of the robotic arm, the stiffness of the joint is controlled to be small to avoid movement obstruction.

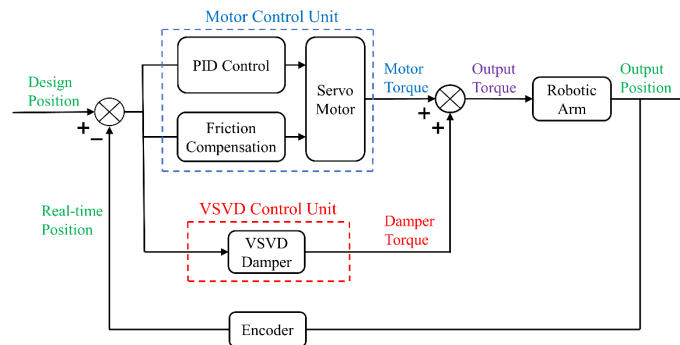


Figure 4.2. Block diagram of the real-time control system

To evaluate the performance of the proposed positioning control system, two kinds of signals are designed. One is a step function signal (**Figure 4.3(a)**): a 10-degree step is

commanded at the initial moment  $t = 0$  s. The arm will move from 0 to 10 degree, and be settled at 10 degrees. The step function signal can test the response of the proposed positioning system under an instant command. In order to evaluate the positioning control performance of the system under a back-and-forth movement, a customised function signal as shown in **Figure 4.3(b)** was also designed; this signal is based on a sinusoid wave with an amplitude of 10 degrees and frequency of 1.3 Hz. 2-second dwells are added at the positions of 10 and -10 degrees. Namely, the robotic arm moves back-and-forth between -10 and 10 degrees following half-sinusoid signals with 2 seconds of dwells at the position of  $\pm 10$  degrees. Compared to a rectangular function signal, the designed customised function signal incorporated with half-sinusoid signals allows the system to accelerate and decelerate gradually during the back-and-forth movement. Therefore, the designed customised function signal was utilised instead of a rectangular function signal.

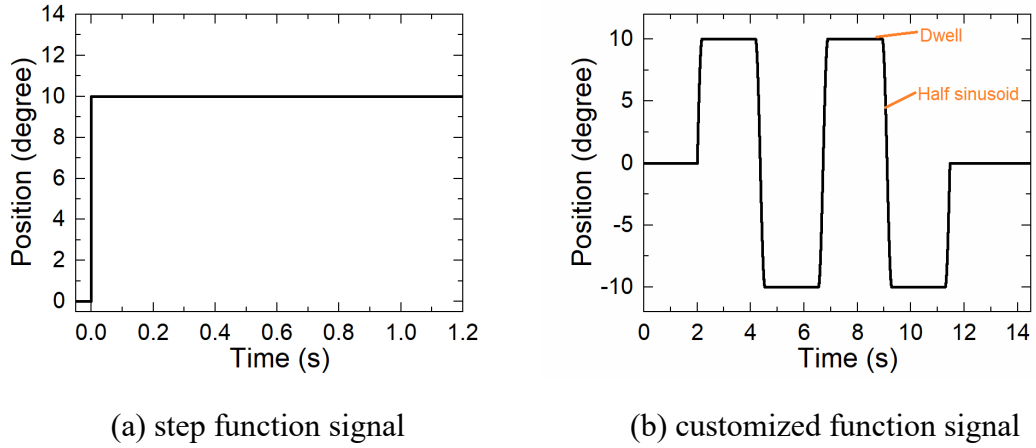


Figure 4.3. Two designed working signals

To improve the positioning control performance under these two working signals, the control strategy of the VSVD damper is designed. For the step signal, VSVD will be turned on once the real-time position reaches the pre-set position of 10 degrees ( $I_1 = I_2 = 3.0$  A), after which the overshoot will happen. For the customised signal, VSVD will be turned on once the real-time position reaches 10 and -10 degree, namely the dwell periods ( $I_1 = I_2 = 3.0$  A). Over the periods of sinusoid when the motor drives the robotic arm to move from one end to another, the VSVD is turned off to avoid obstructing movement. It is noted that the motor control unit works in the whole period of movement to drive the arm. Under the conditions of these two signals, the performance of the positioning control system is evaluated numerically in Section 4.3 and

experimentally in Section 4.4.

### 4.3 System Modeling and Parameter Identification

In this section, the performance of the positioning control system incorporated with a VSVD damper is evaluated by mathematical simulation. The governing equation for the robotic arm positioning system is expressed as

$$J\ddot{\phi}_1(t) = 20T_m(t) - T_{VSVD}(t) \text{sign}(\dot{\phi}_1(t)) - T_f \text{sign}(\dot{\phi}_1(t)) \quad (4-1)$$

where  $J = 1.0875 \text{ kg m}^2$  represents the moment of inertia of the rotational parts: the mass, the robotic arm, the plate, the shaft, the internal damper rotor and the internal damper coils.  $T_m(t)$  is the output torque of the motor determined by PID control and friction compensation. It is magnified 20 times by the 20-time gearbox before being transferred to the shaft. It is known that gear flexibility, friction, and loading have an influence on gearbox efficiency. However, for the reason of simplicity, the gearbox efficiency was ignored here. Namely, a 20-time gearbox was assumed to both amplify the torque and diminish the rotation angle in 20 times.  $T_{VSVD}(t)$  is the torque output of the VSVD damper.  $T_f$  represents the friction of the sealing components like O-rings and bearings, and its value was assumed as 4.235 N m from experiment experience.  $\phi_1(t)$  is the position of the shaft that can represent the real-time position of the robotic arm. As both  $T_{VSVD}$  and  $T_f$  are in the reverse direction of the robotic arm's movement, they are multiplied with ' $-\text{sign}(\dot{\phi}_1(t))$ '.

For the motor output  $T_m(t)$ , it is determined by a PID controller and a friction compensation:

$$T_m(t) = T_{PID}(t) + T_{fc}(t) \quad (4-2)$$

$$\text{and } T_m(t) \leq T_{m\_max}$$

where  $T_{m\_max}$  is the output limitation of the motor. Considering that the continue rated torque for the motor is 1.3 N·m and that it can perform 1.5 N·m for a short period,  $T_{m\_max}$  is set as 1.5 N·m.

$T_{PID}(t)$  is the output calculated by the PID controller:

$$T_{PID}(t) = k_p \phi_{error}(t) + k_i \int_0^t \phi_{error}(t) dt + k_d \frac{d(\phi_{error}(t))}{dt} \quad (4-3)$$

where  $k_p = 1.2$ ,  $k_i = 0.001$  and  $k_d = 0.001$  are parameters of the PID controller. These

parameters are determined by experimental experiences.  $\varphi_{error}(t) = \varphi_{design}(t) - \varphi_1(t)$  denotes the displacement error between the design position  $\varphi_{design}(t)$  and the real-time position of the robotic arm  $\varphi_1(t)$ . The real-time position is acquired by the feedback signal from the built-in encoder of the servo motor.

$T_{fc}(t)$  in Equation. (4-2) represents the friction compensation, and it is expressed as

$$T_{fc}(t) = k_f \dot{\varphi}_1(t) \quad (4-4)$$

and  $T_{fc}(t) \leq T_{fc\_max}$

where  $k_f$  and  $T_{fc\_max}$  are the friction coefficient and the assumed maximum friction, respectively. According to the experiment experience,  $k_f$  was set as 0.003 and  $T_{fc\_max}$  was set as 0.2 N m.

Following the above system modelling, the mathematical model of the VSVD damper should also be built to describe its behaviour. The proposed model was demonstrated in **Figure 4.4**.

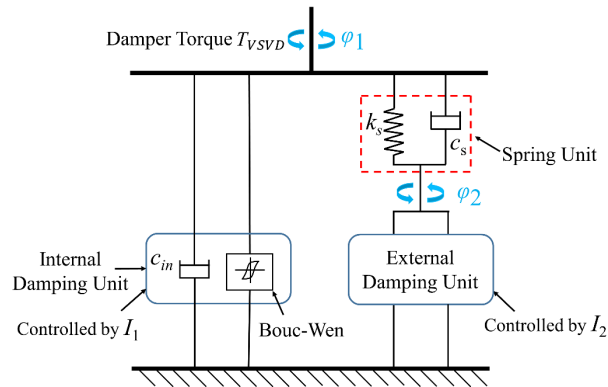


Figure 4.4. Schematic diagram of the proposed model for the VSVD damper

$\varphi_1$  and  $\varphi_2$  in the figure represent the angular displacement of the internal damper shaft & plate and the external damper casing, respectively. The output torque of the VSVD damper  $T_{VSVD}(t)$  is expressed as the sum of the internal damper torque  $T_{in}(t)$  and the spring torque  $T_s(t)$ :

$$T_{VSVD}(t) = T_{in}(t) + T_s(t) \quad (4-5)$$

Bingham model and Bouc-Wen model are two of the most popular models to describe the behaviour of MR damper [126, 128]. Bingham model was utilized in

Chapter 3 for modelling the VSVD MR damper. Considering Bouc- Wen model is better in predicting the force-displacement and force-velocity behaviour of MR dampers, it was chosen here to model the modified VSVD MR damper. Therefore,  $T_{in}(t)$  can be written as

$$T_{in}(t) = c_{in}(I_1)\dot{\phi}_1(t) + \alpha_{in}(I_1)z(t) \quad (4-6)$$

where  $c_{in}(I_1)$  is the viscous coefficient and  $\alpha_{in}(I_1)$  is a scaling factor. Their relations to  $I_1$  will be confirmed in the following parameter identification.  $z(t)$  is an evolutionary variable representing a function of the time history of the displacement. Its governing equation is expressed as

$$\dot{z}(t) = -\gamma|\dot{\phi}_1(t)|z(t) - \beta\dot{\phi}_1(t)z(t)^2 + A\dot{\phi}_1(t) \quad (4-7)$$

where  $A$ ,  $\beta$  and  $\gamma$  are parameters used to describe the hysteresis behaviour.

The rubber spring served as a stiffness unit is characterised by a spring unit  $k_s$  and a damping coefficient  $c_s$ , so the spring torque  $T_s(t)$  is calculated by:

$$T_s(t) = k_s(\phi_1(t) - \phi_2(t)) + c_s(\dot{\phi}_1(t) - \dot{\phi}_2(t)) \quad (4-8)$$

where  $\phi_1(t) - \phi_2(t)$  means the displacement difference of the plate and the external damper casing. As the rubber spring was installed between the plate and the external damper casing,  $\phi_1(t) - \phi_2(t)$  also represents the twisted angle of the rubber spring. Accordingly,  $\dot{\phi}_1(t) - \dot{\phi}_2(t)$  indicates the twisting velocity of the rubber spring.

When the plate starts to rotate with the shaft, the rubber spring will be twisted at the first stage. At this stage, the spring torque is smaller than the yield torque of the external damper ( $T_s(t) < T_{ex\_yield}(I_2)$ ), so the external damper casing keeps still ( $\dot{\phi}_2(t) = 0$ ). As the increases of the twisting angle, the spring torque will increase until it yields the external damper torque ( $T_s(t) = T_{ex\_yield}(I_2)$ ) and an equilibrium state is reached. At this equilibrium state, the spring torque remains the same as the external damper torque. The external damper casing will also rotate at the same velocity as the plate ( $\dot{\phi}_2(t) = \dot{\phi}_1(t)$ ) and the twisting angle of the rubber spring and the spring torque output will not change. This equilibrium is held until the shaft changes its rotation direction. The external damper casing will keep still again until the external damper torque is yield. Here must state that the aforementioned process is a simplified description of the physical phenomenon for the mathematic modelling. Factors such as

the inertial of the external casing are neglected here for simplicity. As the direct relation between  $T_{ex\_yield}(I_2)$  and  $I_2$  can be established by the following parameter identification, the external damper is not modelled here. To sum up, the governing equations for  $\varphi_2$  is built as:

$$\begin{aligned} \text{If } k_s |\varphi_1(t) - \varphi_2(t)| < T_{ex\_yield}(I_2) \\ \dot{\varphi}_2(t) = 0 \end{aligned} \quad (4-9)$$

$$\begin{aligned} \text{elseif } k_s |\varphi_1(t) - \varphi_2(t)| = T_{ex\_yield}(I_2) \\ \dot{\varphi}_2(t) = \dot{\varphi}_1(t) \end{aligned} \quad (4-10)$$

In order to characterise and predict the behaviour of the VSVD damper, parameters in the **Equations (4-4) – (4-10)** were identified using the parameter estimation tool in the Matlab/Simulink (Matlab 2016b). The main goal of this tool is to find the best set of parameters that can match the modelled results with the experimental data to the greatest degree. **Table 4.1** presents the identified parameters. Parameters  $A$ ,  $\beta$ ,  $\gamma$ ,  $k_s$ , and  $c_s$  are set as constants. In contrast,  $\alpha_{in}(I_1)$  and  $c_{in}(I_1)$  increase as the increase of  $I_1$ , and  $T_{ex\_yield}(I_2)$  increases as the increase of  $I_2$ .

Table 4. 1. Identified parameters of the proposed model

Parameter	Variable damping ( $I_1$ changed)				Variable stiffness ( $I_2$ changed)			
	$\frac{I_1=0}{A, I_2=}$	$\frac{I_1=1}{A, I_2=}$	$\frac{I_1=2}{A, I_2=}$	$\frac{I_1=3}{A, I_2=}$	$\frac{I_1=0}{A, I_2=}$	$\frac{I_1=0}{A, I_2=}$	$\frac{I_1=0}{A, I_2=}$	$\frac{I_1=0}{A, I_2=}$
	0 A	0 A	0 A	0 A	0 A	1.0 A	2.0 A	3.0 A
$A$	0.3484 7	0.3484 7	0.3484 7	0.3484 7	0.3484 7	0.3484 7	0.3484 7	0.3484 7
$\beta$ ( $rad^{-2}$ )	441.53	441.53	441.53	441.53	441.53	441.53	441.53	441.53
$\gamma$ ( $rad^{-2}$ )	9467.8	9467.8	9467.8	9467.8	9467.8	9467.8	9467.8	9467.8
$k_s$ ( $Nm/rad$ )	385.31	385.31	385.31	385.31	385.31	385.31	385.31	385.31
$c_s$ ( $Nm \cdot s/rad$ )	7.591	7.591	7.591	7.591	7.591	7.591	7.591	7.591
$\alpha_{in}$ ( $Nm/rad$ )	441.53	2451.3	3635.7	4456.0	441.53	441.53	441.53	441.53
$c_{in}$ ( $Nm \cdot s/rad$ )	1.0734	1.4235	1.8643	2.3565	1.0734	1.0734	1.0734	1.0734
$T_{ex\_yield}$ ( $Nm$ )	6.011	6.011	6.011	6.011	6.011	27.280	46.237	54.136

**Figure 4.5** plots the comparison between the modelled results and the experimental data. As illustrated in the figure, the modelling results (solid lines) using the established mathematic model with the identified parameters can fit the experimental data (dash lines) very well for both variable damping (**Figure 4.5(a)**) and variable stiffness (**Figure 4.5(b)**) cases. To valid the predictive accuracy of the built model and the identified parameters, at the condition of ‘ $I_1 = 1.0$  A and  $I_2 = 1.0$  A’, modelling result (solid line) is compared with experimental data (dash line) in **Figure 4.5(c)**. The modelling result in the figure is plotted by using the values of  $\alpha_{in}(I_1 = 1.0$  A),  $c_{in}(I_1 = 1.0$  A) and  $T_{ex\_yield}(I_2 = 1.0$  A). It is seen that the modelling result can fit the experimental result very well, indicating a good prediction performance of the proposed model.

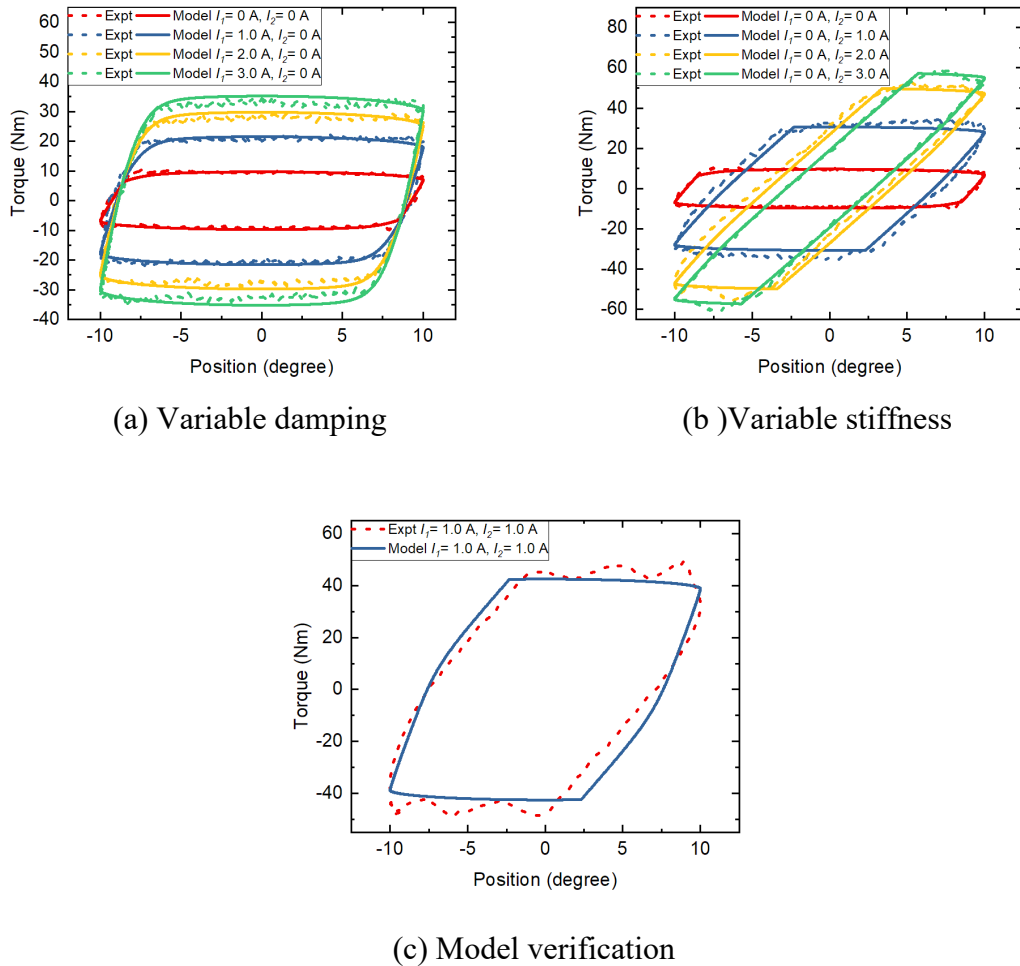


Figure 4.5. Comparison between the modelled results and experimental results

For the simulation of the positioning control system in the next section, polynomial fitting equations for  $\alpha_{in}(I_1)$ ,  $c_{in}(I_1)$ , and  $T_{ex\_yield}(I_2)$  are obtained as:

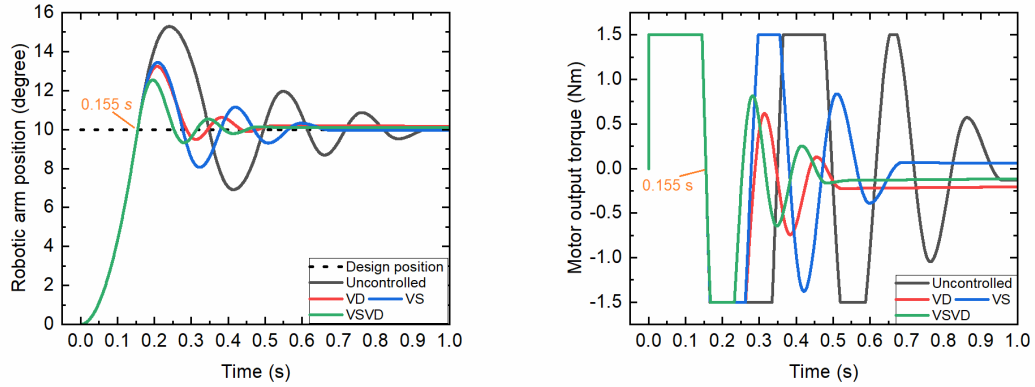
$$\alpha_{in}(I_1) = -303.60I_1^2 + 2241.05I_1 + 440.92 \quad (4-11)$$

$$c_{in}(I_1) = 0.0355I_1^2 + 0.3224I_1 + 1.0714 \quad (4-12)$$

$$T_{ex\_yield}(I_2) = -3.3425I_2^2 + 26.3607I_2 + 5.5737 \quad (4-13)$$

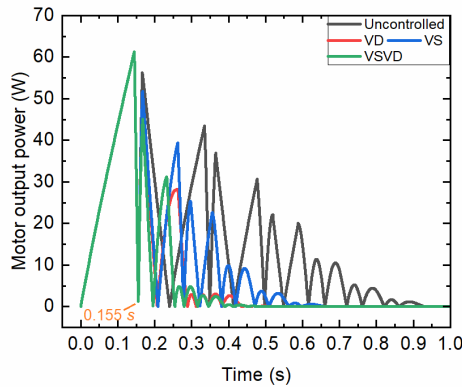
#### 4.4 Numerical evaluation of the positioning control system

##### 4.4.1 Step function signal simulation



(a) Time history of robotic arm position

(b) Time history of motor output torque



(c) Time history of the motor output power

Figure 4.6. Simulation results under the step function excitation

After the establishment of the mathematical model, the performance of the positioning control under the designed step and customised function signals is evaluated by mathematical simulations using Matlab/Simulink module. Four control modes are evaluated and compared to prove the effectiveness of VSVD: ‘Uncontrolled’ means the positioning control is achieved only by the motor control unit; ‘VD’ means the internal damper that controlling the damping is working; ‘VS’ means the external damper that



controlling the stiffness is working; ‘VSVD’ means both of them are working. It is noted that the motor control unit is always working for all four control modes to drive the robotic arm. For the step function excitation, VS, VD, and VSVD will be turned on once the real-time position reaches the pre-set position: 10 degree. For the customised function excitation, VS, VD, and VSVD will be turned on once the real-time position reaches +10 degree or -10 degree, but they will be turned off over the periods of sinusoid signals to avoid obstruction.

The simulation result of the step function signal is illustrated in **Figure 4.6**. **Figure 4.6(a)** demonstrates the time history of the robotic arm position, which is represented by the shaft position  $\varphi_1(t)$ . The motor output torque  $T_m(t)$  is plotted in **Figure 4.6(b)**. Additionally, the motor output power  $P(t)$  is illustrated in **Figure 4.6(c)** and it is calculated by

$$P(t) = |20 T_m(t) (\varphi_1(t) - \varphi_1(t-1/f_s)) f_s| \quad (4-14)$$

where  $f_s = 2000$  Hz is the sample rate of the data recording. 20 represents the magnification factor of the 20:1 gearbox.  $(\varphi_1(t) - \varphi_1(t-1/f_s))$  means the displacement difference of the robotic arm in the sampling period  $1/f_s$ . As each data group of the time, arm position and motor torque is recorded in every sampling period of  $1/f_s$ , the real-time motor power can be calculated as the energy consumed in each period  $(20 T_m(t) (\varphi_1(t) - \varphi_1(t-1/f_s)))$  divided by the time period  $1/f_s$ .

The case of ‘uncontrolled’ is chosen as an example to illustrate the whole positioning control process. As shown in **Figure 4.6**, when the robotic arm moves from 0 degree ( $t = 0$  s) to 10 degree ( $t = 0.155$  s), the motor torque is positive to drive the robotic arm to move towards the pre-set position. After overshoots occurred at  $t = 0.155$  s, the motor torque changed to negative to pull back the arm to the pre-set position. Both the arm position and the motor torque are oscillating after  $t = 0.155$ , with the amplitudes of them gradually reduced to zero. Then, the arm position and the motor torque are settled at  $t = 1.0$  s, with the motor power settled as well. It is seen from **Figure 4.6** that, the time histories of the arm position, the motor torque and the motor power are the same for all the four control modes before  $t = 0.155$  s because only the motor control unit is working in this period. In contrast, these three values are different for the four control modes after  $t = 0.155$  s when different control strategies are applied. If VD works after  $t = 0.155$  s, damping torque that always works in the reverse direction

of the movement will act on the system, which helps to reduce the overshoot and the settling time. If VS works after  $t = 0.155$ s, spring torque works towards the pre-set position (10 degrees) will increase the stiffness of the system. Therefore, the overshoot is reduced, and the settling time is also reduced with a smaller vibration frequency.

Two evaluation indexes are selected to estimate the performance of the positioning system. One is the overshoot denoting the difference between the maximum arm position and the pre-set arm position. The other one is the settling time, which is defined as the time period from the initial to the time at which the oscillation is not exceeding  $\pm 1\%$  of the pre-set position [86]. A smaller overshoot and a shorter settling time mean a better positioning performance. The overshoot and the settling time for all the control modes of the simulation results are summarised in **Table 4.2** and **Table 4.3**, respectively.

Table 4. 2. Overshoot of the robotic arm

	Uncontrol	VD	VS	VSVD
Overshot (degree)	5.28	3.24	3.43	2.54
Reduction proportion	NA	38.64%	35.04%	51.90%

Table 4. 3. Settling time of the robotic arm

	Uncontrol	VD	VS	VSVD
Settling time (s)	0.918	0.499	0.646	0.459
Reduction proportion	NA	45.64%	29.63%	50.00%

Compared with the Uncontrolled case, it is found that overshoot was largely reduced in the cases of VD (38.64%) and VS (35.04%). Furthermore, more than 51.9% of overshoot is reduced in the case of VSVD. Similarly, VSVD has the shortest settling time of 0.459 s, with 50% reduction. The cases of VD and VS also shown improvement in settling time.

By integrating the real-time power output  $P(t)$  over time, the energy worked by the motor in the whole period is given in **Table 4.4**. For the four cases, the calculated energy worked in the period from 0 to 0.115 s is the same as 4.96 J. The energy differences lie in the period after  $t = 0.155$  s, so the energy worked after  $t = 0.155$  s is

also presented together with that in the whole period. If only the energy worked after  $t = 0.155$  s is considered, VD and VS have 69.81% and 48.85% reduction in energy compared to that of Uncontrolled case. VSVD has the largest reduction proportion: 76.62%. If compared in the whole period, VSVD also has the largest energy reduction of 51.17%.

Table 4.4. Energy consumed by the motor

	Uncontrol	VD	VS	VSVD
Energy consumed after $t = 0.155$ s (J)	9.97 J	3.01 J	5.10 J	2.33 J
Energy consumed in the whole period (J)	14.93 J	7.97 J	10.06 J	7.29 J
Reduction proportion (after /whole)	NA	69.81%/4 6.61%	48.85%/32. 62%	76.62%/51. 17%

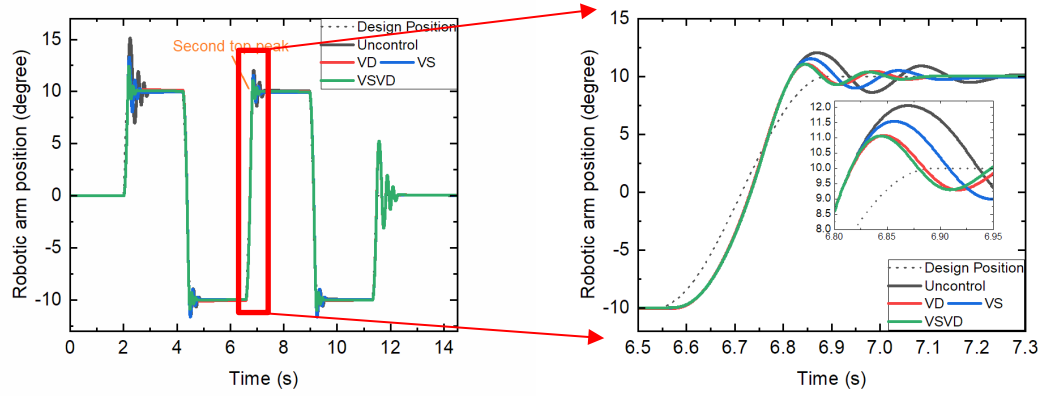
It is concluded from the above analyses that the performance of the positioning system is improved in the cases of VD, VS and VSVD. The VSVD mode works best among them under the step function excitation.

#### 4.4.2 Customised function signal simulation

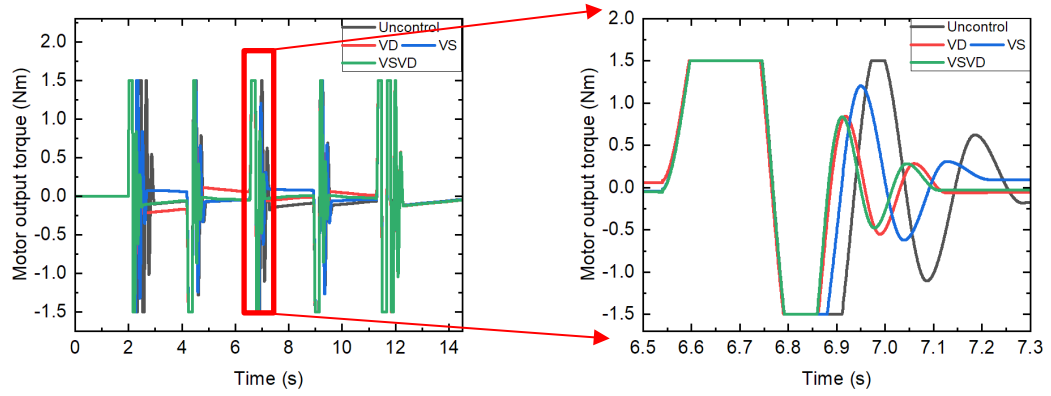
Following the evaluation under step function excitation, the performance of the positioning control under customised function excitation is also simulated, with the results presented in **Figure 4.7**. The figures in the left column (**Figure 4.7(a)-(c)**) demonstrate the results under the whole period of the step function signal. To further analyse the results at the peaks, the response of the second top peak from 6.5s to 7.3s is also enlarged and illustrated in the right column (**Figure 4.7 (d)-(f)**).

It is seen from **Figure 4.7(a)** that the first top peak has the largest overshoot over the whole period. Besides, the last period when the robotic arm returned to zero also has the large overshoot for all the cases, as only a motor control unit is applied in this period. Among all the peaks, the first peak has the largest differences in motor torque output (**Figure 4.7(b)**) and power output (**Figure 4.7(c)**) as well.

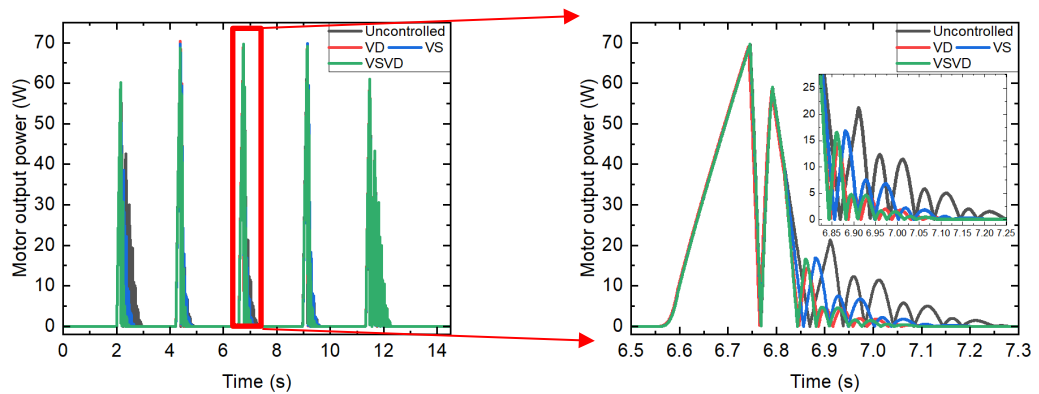
As shown in **Figure 4.7(d)** that the overshoot and the fluctuation during settling time are reduced at the second top peak in the cases of VD and VS. VSVD has the smallest overshoot and the shortest settling time among all cases, even though VD has very comparable performance. Regarding the motor output torque and the output power



(a) Time history of robotic arm position (the whole period) (d) Time history of robotic arm position (the second top peak)



(b) Time history of motor torque output (the whole period) (e) Time history of motor torque output (the second top peak)



(c) Time history of the motor output power (the whole period) (f) Time history of the motor output power (the second top peak)

Figure 4.7. Simulation results of customised function signal excitation

(Figure 4.7(e) and (f)), results before the overshoot ( $t \approx 6.816$  s) are almost the same, as only the motor control unit is working in this period. After the overshoot, the VSVD has the best performance with relative smaller motor torque and power.

To further evaluate the positioning control performance of all cases, average overshoot, settling time, and the energy consumed by the motor in the whole working period are summarised in Table 4.5, 4.6, and 4.7, respectively. Because the last re-zero movement is the same for all cases, it is excluded in the calculation of the average overshoot and settling time. As indicated in the Tables, VSVD has the best performance as respect to average overshoot (47.60% reduced), average settling time (28.87% reduced), and the energy consumed by the motor (28.87% reduced). Cases of VD and VS also illustrate improvements in these three indexes.

Table 4.5. Average overshoot

	Uncontrol	VD	VS	VSVD
Average overshoot (degree)	2.5455	1.6448	2.0195	1.3338
Reduction proportion	NA	35.38%	20.66%	47.60%

Table 4.6. Average settling time

	Uncontrol	VD	VS	VSVD
Average settling time (s)	0.7815	0.5720	0.6740	0.5559
Reduction proportion	NA	26.81%	13.76%	28.87%

Table 4.7. Energy worked by the motor

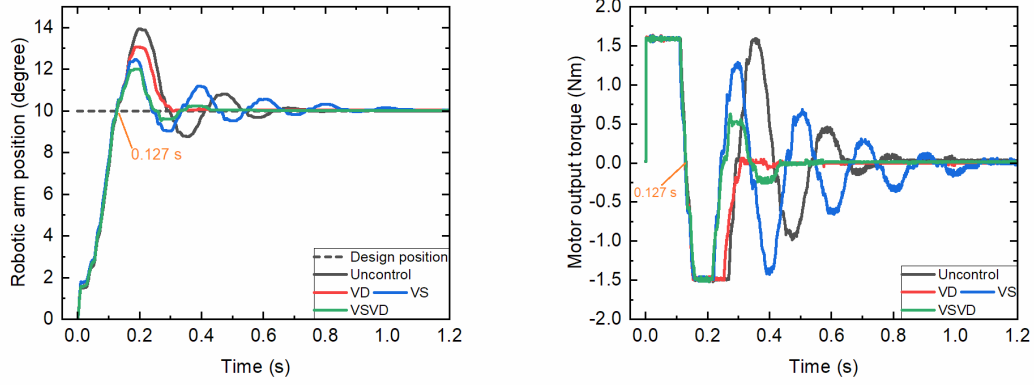
	Uncontrol	VD	VS	VSVD
Total Energy (J)	62.65	53.22	57.09	51.86
Reduction proportion	NA	15.05 %	8.87%	17.22%

#### 4.5 Experimental evaluation of the positioning control system

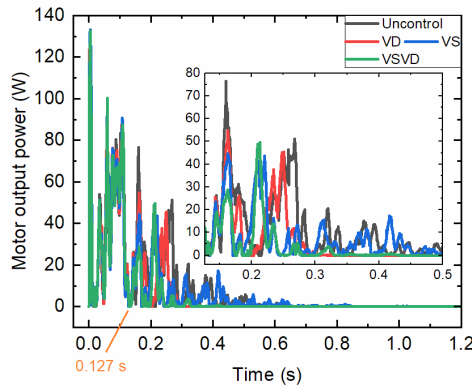
After established the experimental set-up demonstrated in Figure 4.1, the positioning control performance of the robotic arm system is evaluated experimentally

under the step function signal and the customised function signal, respectively. Corresponding test results and analyses are presented in this section.

#### 4.5.1 Step function signal simulation



(a) Time history of the robotic arm position (b) Time history of motor torque output



(c) Time history of the motor power output

Figure 4.8. Experimental test results under the step function excitation

Under the step function signal, the recorded time history results of the robotic arm position, motor torque output, and the calculated power output are presented in **Figure 4.8**; the average overshoot, average settling time, and the energy consumed by the motor are summarised in **Table 4.8**, **4.9**, and **4.10**, respectively. Vibrations occurred before 0.05 s for all the cases as a consequence of a sudden torque command of PID output at the initial, which was triggered by a significant difference between the designed position and the real-time position. Before overshoot happened at 0.127 s, the results of robotic arm position, motor torque output, and motor output power of the four cases are almost the same. After 0.127 s, the VSVD has the smallest overshoot of 2.008 with a reduction of 49%, and the shortest settling time of 0.4230 with a reduction of 40.30%

compared with Uncontrolled case (**Table 4.8** and **4.9**). VS has a smaller overshoot but a longer settling time than Uncontrolled case. As shown in Tab. 10 on the energy consumed by motor, VD and VS have reduced 19.84% and 20.04% in the whole period, respectively; VSVD has the largest reduce proportion of 29.74%. If only consider the period after the pre-set position in which different control methods applied, the VSVD can reduce 65.68% of the motor output power of Uncontrolled case. In addition, VS and VD also have improvement regarding these three indexes.

Table 4.8. Overshoots of the robotic arm

	Uncontrol	VD	VS	VSVD
Overshot (degree)	3.937	3.051	2.463	2.008
Reduction proportion	NA	22.5%	37.44%	49.00%

Table 4.9. Settling time of the robotic arm

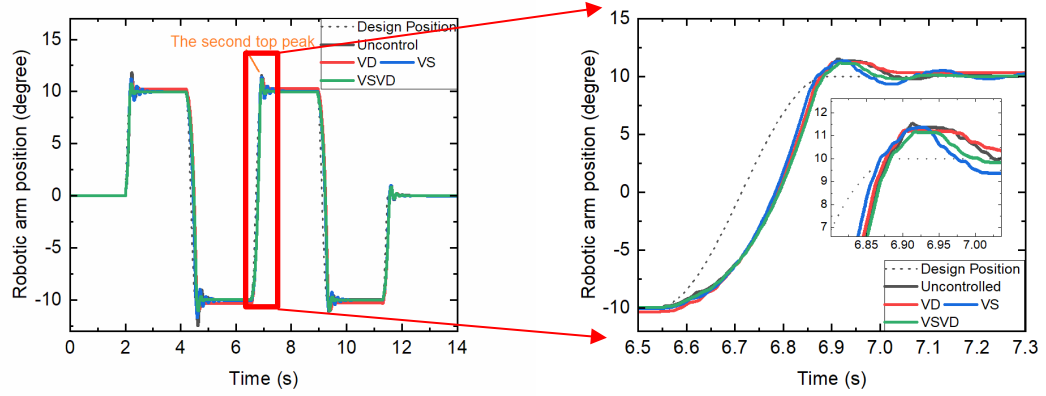
	Uncontrol	VD	VS	VSVD
Settling time (s)	0.7085	0.3010	1.0905	0.4230
Reduction proportion	NA	57.52%	-53.92%	40.30%

Table 4.10. Energy consumed by the motor

	Uncontrol	VD	VS	VSVD
Total energy (J)	9.7549	7.8198	8.5806	6.8530
Energy consumed in the whole period (J)	4.4423	2.4640	3.2242	1.5248
Reduction proportion (whole/after)	NA	19.84%/44.53%	12.04%/27.42%	29.74%/65.68%

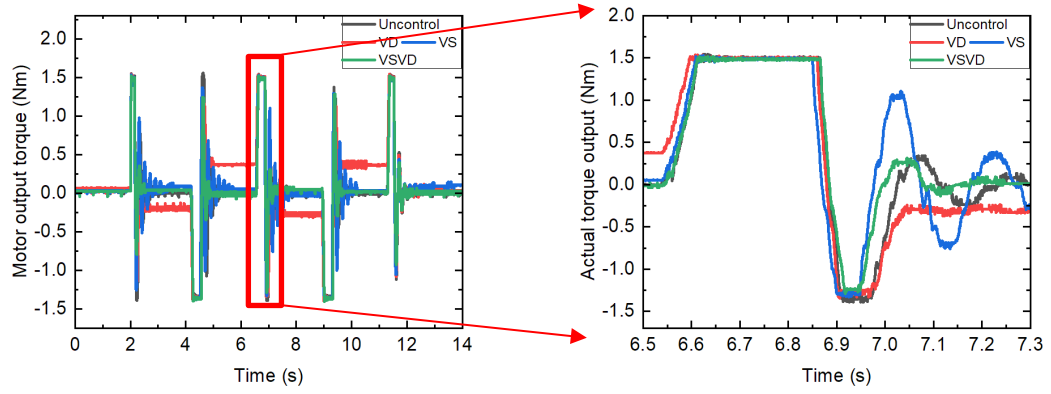
#### 4.5.2 Customised function signal simulation

The experimental test results under the customised function signal are presented in **Figure 4.9**. Different control methods are applied in the dwell period where overshoots happened, while only the motor control works in the periods consist of harmonic signals



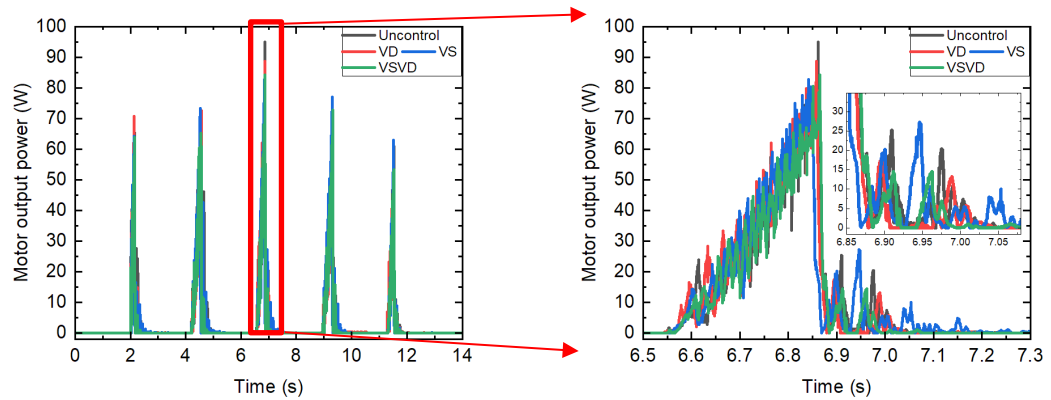
(a) Time history of robotic arm position  
(the whole period)

(d) Time history of robotic arm position  
(the second top peak)



(b) Time history of motor torque output (the whole period)

(e) Time history of motor torque output  
(the second top peak)



(c) Time history of the motor output power  
(the whole period)

(f) Time history of the motor output power  
(the second top peak)

Figure 4.9. Experimental test results under the customised function excitation (left column: results during the whole period; right column: detailed results of the second top



peak).

for all cases. Similar to the simulation results presented in **Figure 4.7**, the experimental results are demonstrated in the left column (**Figure 4.9(a)-(c)**), and the results of the second top peak from 6.5s to 7.3s are illustrated in the right column (**Figure 4.9(d)-(f)**) for further analyses.

As shown in **Figure 4.9(a)**, the overshoot at the first top and bottom peaks are larger than other peaks. VSVD has the smallest overshoot as well as the vibration during the settling time at the second top peak, given that the results are very close for all cases (**Figure 4.9(d)**). VSVD also has the smallest motor output torque (**Figure 4.9(e)**) and motor output power (**Figure 4.9(f)**) after the overshoot ( $t \approx 6.88$  s).

To better evaluate the positioning performance, average overshoot, average settling time, and the total energy consumed by the motor are summarised in **Table 4.11**, **4.12**, and **4.13**, respectively. **Table 4.11** demonstrates that both VD and VS can reduce the overshoot, and VSVD works best among them with 42.63% reduction of the overshoot compared with Uncontrolled case. Meanwhile, VSVD also has the largest settling time reduction of 24.90% (**Table 4.12**). It is noticed that VS has a longer settling time but smaller overshoot than Uncontrolled case. VD also showed improvement of the overshoot and settling time. As illustrated in **Table 4.13**, VD and VS reduced by 4.98% and 1.136 % of the energy consumed by the motor, respectively, compared with Uncontrolled case. VSVD saved 9.044% of energy, which is the best among them.

Table 4.11. Average overshoot

	Uncontrol	VD	VS	VSVD
Average overshoot (degree)	1.724	1.046	1.309	0.989
Reduction proportion	NA	39.33%	24.07%	42.63%

Table 4.12. Average settling time

	Uncontrol	VD	VS	VSVD
Average settling time (s)	0.998	0.701	1.048	0.694
Reduction proportion	NA	29.76%	-1.36%	30.46%

Table 4.13. Energy consumed by the motor

	Uncontrol	VD	VS	VSVD
Energy (Total) (J)	43.046	40.901	42.557	39.153
Reduction proportion	NA	4.98%	1.14 %	9.04%

#### 4.6 Conclusion

A positioning control system of a robotic arm that utilises a VSVD MR damper is studied in this chapter. To evaluate the proposed positioning control system, a step function excitation and a customised function excitation were designed. For the step function excitation, VSVD control is numerically proved to be able to reduce overshoot by 51.90%, settling time by 50.00% and energy consumption by 51.17%. The experimental results also validated a 49.0% reduction of overshoot, 40.30% reduction of the settling time, and 29.74% reduction of the energy cost by using VSVD control. Similarly, for the customised function signal, the mathematical simulation indicated a 47.63% reduction of overshoot, 28.87% reduction of settling time, and 17.22% reduction of energy cost by using VSVD control. Additionally, experimental results also proved that VSVD control is able to reduce overshoot by 42.63%, settling time by 30.46%, and energy consumption by 9.04%. To sum up, by adopting VSVD control strategy, the positioning control performance of the proposed robotic arm positioning system was significantly improved with less energy consumption.

## Chapter 5

### Vibration control of a seat suspension using VSVD magnetorheological damper

#### 5.1 Introduction

Drivers of heavy-duty vehicles such as mining vehicles, freight trucks and agriculture vehicles are usually exposed to long-term serve vibration caused by road surface unevenness, which significantly threatens their mental and physical health. The drivers tend to lose their concentration, be fatigue and decrease driving performance. Long-term suffering of vibration can lead to diseases such as lumbago, backache and low back pain. Passive suspensions [129, 130], semi-active suspensions [131, 132] and active suspensions [101, 102] have been developed to attenuate the vibration and protect the drivers. Compared to passive suspensions, semi-active suspensions are controllable with fast response for different vibration conditions. Additionally, they possess a simpler mechanical structure, with less pow consumption and better fail-safety than active suspensions. Hence, semi-active suspensions based on smart materials such as electromagnetical (ER) fluids and magnetorheological (MR) fluids are very popular.

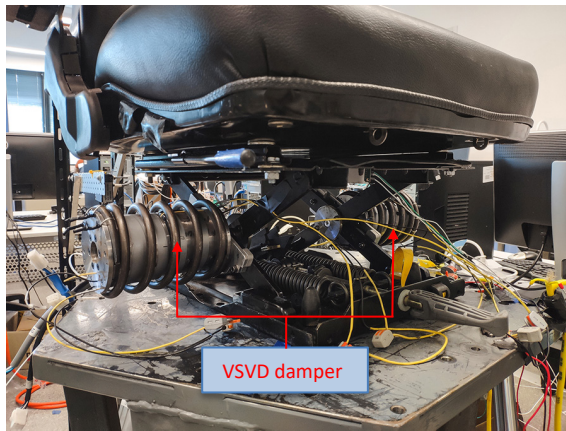
Normally, a semi-active suspension based on MR dampers can reduce the vibration amplitude by regulating its damping. Apart from damping variability, changing the stiffness of a seat suspension will shift its natural resonant frequency away from excitation frequency to avoid resonance. A low stiffness also means the vibration at the high frequency will also be attenuated due to the small transmissibility. However, to meet the loading requirement and avoid end-stop impact when the limited stroke is used out, the seat suspensions must be built with large stiffness. Out of these motivations, this chapter presents a study of semi-active seat suspension based on variable damping and stiffness (VSVD) dampers. The proposed seat suspension can change its damping and stiffness according to different vibration excitations. The suspension is able to remain small transmissibility with a small stiffness in the small stroke range, and prevent end-stop impact by applying a large stiffness in the large stroke range. Besides, the stiffness can also reduce the vibration by absorbing the energy and dissipating it through a spring unit. The remainder of this chapter is organised as follows. Section 5.2 presents the mechanical structure and property tests of the VSVD seat suspension

together with the VSVD dampers specially designed for the seat suspension. The control strategy for regulating the damping and stiffness is provided in Section 5.3. To validate the vibration reduction performance of the proposed VSVD seat suspension, mathematical simulation and experimental test evaluations are provided in Section 5.4 and Section 5.5, respectively, under harmonic signal, bump signal and random signal. Finally, the conclusion is drawn in Section 5.6.

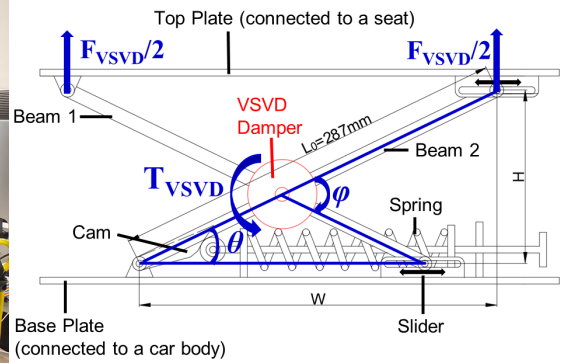
## 5.2 Prototype and working principle of the VSVD seat suspension

### 5.2.1 VSVD seat suspension

A VSVD MR seat suspension demonstrated in **Figure 5.1** is designed and manufactured. This prototype is a modification of a commercial seat suspension, with an original linear damper removed and two identical VSVD MR dampers installed on its scissors structure. As indicated in the side view (**Figure 5.1(b)**), the top plate and the bottom plate are supposed to connect with the seat and the car body, respectively. A scissors structure consists of beam 1 and beam 2 connecting the two plates. The right joints of beam 1 and beam 2 are sited respectively in two sliders mounted on the plates, and they can move simultaneously in the horizontal direction. A spring-cam system provides initial soft stiffness to the suspension. Through the scissors structure, the plates' relative vertical movement is transferred to the angular rotation of the VSVD damper on one hand. On the other hand, VSVD damper's output torque  $T_{VSVD}$  is also transferred to the suspension's vertical damper force  $F_{VSVD}$ . Hence, by regulating the damping and the stiffness of the VSVD damper, the damping and stiffness of the seat suspension can be controlled.



(a) photo of the seat suspension



(b) working mechanism

Figure 5.1. VSVD seat suspension.

### 5.2.2 VSVD MR damper for the seat suspension

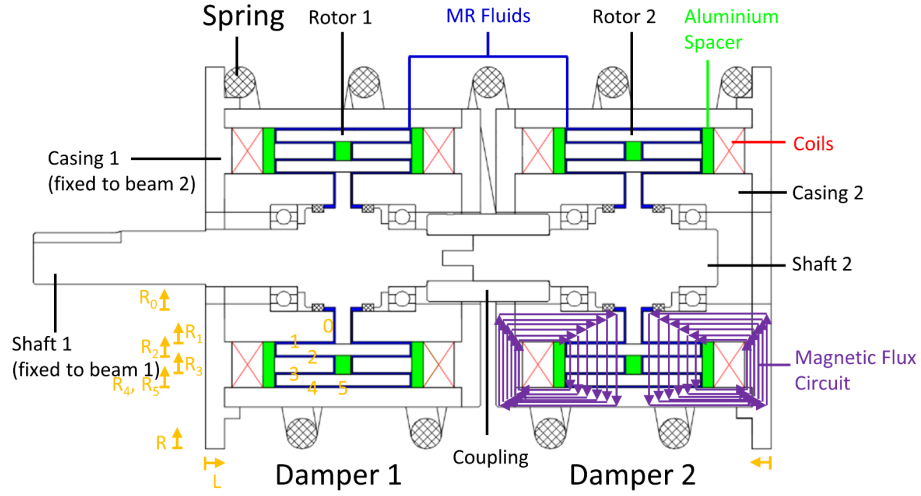


Figure 5.2. Schematic of VSVD MR damper.

In previous research on seat suspension [18, 101, 104, 133], gearboxes are required to be installed between an MR damper or actuator and the suspension's scissor structure. This is because the output torque of an MR damper or actuator is too small for the vibration control so the gearbox is needed to amplify the output torque. However, the introduction of gearboxes increases the complexity of the mechanical structure and the cost of the seat suspension. Besides, the mechanical wear of gear will decrease the efficiency of the gearbox and impair the vibration control performance of the seat suspension. To avoid the introduction of the gearbox, the VSVD MR damper should have a large torque output. One method to increase the damper's output torque is expanding the working area of MRFs as a T-type MR damper developed by Nguyen and Choi [68]. Motivated by this idea, this thesis designed a VSVD MR damper with two double-layer T-type MR damper, as illustrated in **Figure 5.2**. The proposed VSVD MR damper consists of two rotary dampers with identical double-layer T structure and one coil spring between them. Each damper has a shaft, a casing, and a rotor with two circular rings. The shafts are fixed with their corresponding rotors, and one set of shaft and rotor can rotate from the matched casings. Shaft 1 and casing 1 are fixed to scissors structure's beam 1 and beam 2, respectively. Meanwhile, shaft 1 is also fixed to shaft 2 by a coupling seated between two dampers, and casing 1 is fixed to casing 2 by a spring (10 mm in diameter, 4 turns) as well. MR Fluids are filled in the 0.5 mm gaps between rotors and the casings. With aluminium spacers (denoted by the green components) utilised for optimising the magnetic flux, two electromagnet coils (copper wire, 0.5mm,

200 turns) wound in reverse directions can generate magnetic circuits in reverse directions, as indicated in **Figure 5.2**. The working areas for a damper are numbered from 0-5.

When the electromagnetic coils are applied with current, the MR fluids in a rotary damper will transfer from free-flow state to semi-solid state and restrict the relative motion between the casing and the rotor, so that damping torque in the reverse direction of the relative motion will be generated. For the proposed VSVD damper, its the output torque is the torque between shaft 1 and casing 1, and its damping and stiffness are provided by damper 1 and the spring, respectively. To be specific, by regulating  $I_1$ , the damping torque of damper 1 can be controlled so that the damping of VSVD damper is controlled. If  $I_2 = 0$  A, rotor 2 can rotate freely from casing 2 and the spring is not stretched/working with casing 2 keeps still. If  $I_2 > 0$  A, casing 2 will rotate together with rotor 2 at the initial state, and the spring is stretched/working, so the stiffness of the VSVD damper is increased consequently. As the increase of the stretching angle, the spring torque increases. Once it equals the yield damping torque of damper 2, an equilibrium state reached. At this equilibrium state, casing 2 keeps still, and the spring stop further stretched. The equilibrium will be held until the rotor changes its rotate direction. Hence, the damping and the stiffness of the VSVD damper can be controlled by regulating damper 1 and damper 2, respectively. As damper 1 and damper 2 are respectively regulated by  $I_1$  and  $I_2$ , and the suspension's damping and stiffness are determined by VSVD damper, it is easy to deduce that the damping and stiffness of the seat suspension are controlled by  $I_1$  and  $I_2$ , respectively.

### 5.2.3 Property test of the VSVD seat suspension

After the design and prototype, the proposed VSVD seat suspension was characterized by a property test, as shown in **Figure 5.3**. The VSVD seat suspension was put on a computer-controlled MTS test frame (Load frame machine, Type: 370.02, MTS systems corp.) and fixed between the upper and lower clamps. A load cell under the lower clamp can record the real-time force. On the one hand, specific displacement signals were prescribed to drive the upper clamp to move in the vertical direction through the interaction of a computer. On the other hand, the data of displacement and force of the seat suspension are recorded. Meanwhile, a power supply was utilised to provide the currents of  $I_1$  and  $I_2$ . The seat suspension was firstly compressed to the middle of the stroke, and then a harmonic signal was prescribed for the test. With the

stoke limit considered, a harmonic displacement signal with a maximum amplitude of 20 mm with a frequency of 0.5 Hz was set for the property test.

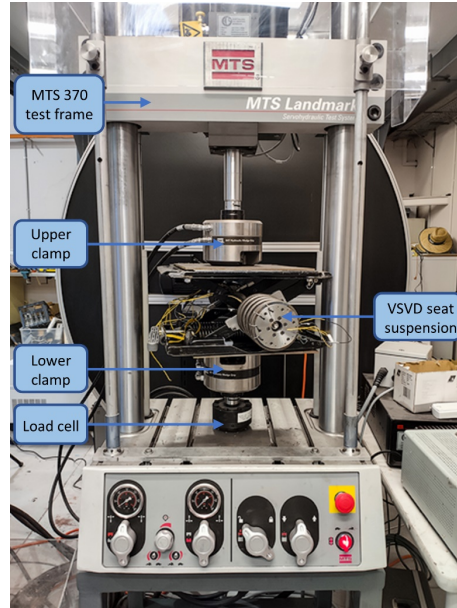
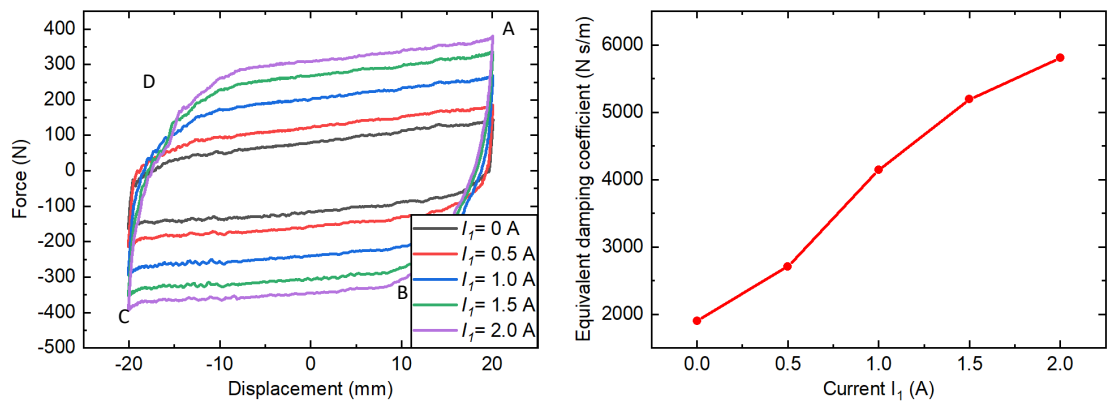


Figure 5.3. Property test of the seat suspension.

As  $I_1$  and  $I_2$  separately control the damping and stiffness of the seat suspension, the current input of  $I_1$  ranging from 0 to 2.0 A with an increment of 0.5 A and  $I_2 = 0$  A were prescribed for the damping variability test, and the current input of  $I_2$  varying from 0 A to 2.0 A with an increment of 0.5 A and  $I_1 = 0$  A was given to test the stiffness variability. The test results of damping and stiffness variabilities are presented in **Figure 5.4 and 5.5**, respectively. Here should be mentioned that the data is generated in the clockwise direction in time series for each force-displacement loop.



(a) force- displacement response ( $I_2 = 0$  A)

(b) equivalent damping coefficient

Figure 5.4. Result of variable damping.

**Figure 5.4(a)** shows the force-displacement response of the damping variation

tests. **Figure 5.4(b)** gives the equivalent damping coefficient  $C_{t,eq}$  at different current levels of  $I_1$ , which is calculated by [125]:

$$C_{t,eq} = \frac{EDC}{2\pi^2 f A^2} \quad (3-1)$$

where  $EDC$  is the energy dissipated per cycle, namely the enclosed area of the force-displacement loops.  $f$  and  $A$  are the frequency and the amplitude of the prescribed harmonic signal, respectively.

As shown in **Figure 5.4(a)**, the enclosed area of the force-displacement loop increases as the increase of  $I_1$ . The damping force is a constant and displacement-independent force determined by damper 1, contributing to the force differences in AB and BC, where the displacement changes direction. Its magnitude is decided by  $I_1$ , and the direction is in the reverse direction of the motion. In contrast, the stiffness force is a displacement-dependent force generated by the spring on the seat suspension and the spring of the VSVD damper, and it is denoted by the ratio of force/displacement in BC and DA. If  $I_2 = 0A$ , the spring of the VSVD damper is not activated so that the stiffness force is only contributed by the seat suspension's spring; if  $I_2 > 0A$ , the spring of the VSVD damper is activated and the stiffness force is caused by both the seat suspension's spring and the VSVD damper's spring. As  $I_1$  is increased from 0 to 2 A and  $I_2$  is remained as 0A, the force differences of AB and BC increase as the increase of  $I_1$  while the force differences of BC and DA remain the same. The equivalent stiffness in the vertical direction of the seat suspension's spring can be calculated by the ratio of sections BC and DA as 1468.686 N/m. As shown in **Figure 5.4(b)**, the equivalent damping coefficient increased 3 times from 1903.89 to 5806.61 N s/m as  $I_1$  increased from 0 to 2 A.

**Figure 5.5** presents the results of the stiffness variability test. It is noticed that the damping force remain the same while the stiffness force increases as the increase of  $I_2$ . In AB of the case  $I_2 = 0.5 A$ , the damping force changes its direction and generates a force difference when the displacement changes direction at 20 mm. As the displacement decreases from 20 to -10 mm (from B to C), the spring of the VSVD damper is continuously stretched, and the force decreases in numerical. In this period, the spring torque increases but still smaller than the yield torque of damper 2, so that casing 2 and rotor 2 are move together without any relative motion. At point C, spring torque yields the yield torque of damper 2, and relative movement between casing 2 and



rotor 2 happens. In the section of CD, the spring of the VSVD damper stopped further stretched. The stiffness in BC is the sum stiffness of the seat suspension's spring and the VSVD damper's spring. In contrast, the stiffness in CD is the stiffness of seat suspension's spring only. When  $I_2 > 0.5$  A, the yield torque of damper 2 are very large so that the VSVD damper's spring can not yield it within the limited stretch range. Hence, the stiffness in the range of 20 to -20 mm is consistent for all the cases of  $I_2 = 1$  A, 2 A and 3 A, and the data results for these cases are overlapped. Considering the control current of  $I_2$  is set as either 0 or 2 A in the following sections and damper 2 can not be yield, effective stiffness represented by the ratio of sections from 20 to -20 mm is adopted here. As  $I_2$  increased from 0 to 2 A, the calculated effective stiffness for the seat suspension increased 5.34 times from 1468.686 to 7844.471 N/m.

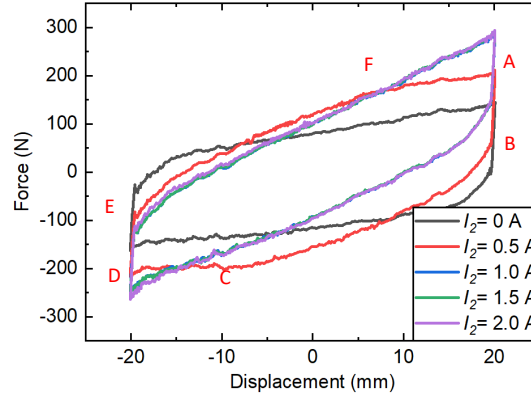


Figure 5.5. Result of variable stiffness ( $I_1 = 0$  A).

### 5.3 Control strategy design

To realise an excellent vibration control performance, a control strategy for varying the damping and stiffness is designed in this section.

For the damping control, a no-jerk skyhook control strategy [134] that can achieve a smooth dynamic response and eliminate the damping-force discontinuity is adopted:

$$I_1 = \begin{cases} k * V_s V_{sp}, & V_s V_{sp} > 0 \\ 0, & V_s V_{sp} \leq 0 \end{cases} \quad (5-1)$$

where  $V_s$  and  $V_{sp}$  are the seat's velocity and relative velocity to the vehicle body, namely the top plate's velocity and the relative velocity between the top and base plates, respectively.  $k = I * E^{-5}$  is a constant gain of the skyhook control, which is decided by the experimental experience.

Regarding stiffness control, large stiffness should be prescribed to prevent end-stop

impact. At the same time, seat suspension's stiffness should remain a low level to extend the vibration attenuation range and lower the transmissibility. To meet these contradictory requirements, an on-off control is designed as follows

$$I_2 = \begin{cases} 2A, & V_{sp} > 0 \text{ and } D_{sp} > D_T \\ 2A, & V_{sp} < 0 \text{ and } D_{sp} < -D_T \\ 0A, & \text{others} \end{cases} \quad (5-2)$$

where  $D_{sp}$  is the seat's relative displacement to the platform represented by the relative displacement between the top and base plates.  $D_T = 10$  mm is a threshold displacement of which the value is tuned by the experimental experience. **Figure 5.6** demonstrates the control strategy for stiffness. It is known from the experiment that the stroke range of the suspension is  $D_{sp} = -40 \sim 40$  mm, and the end-stop impact at -40 and 40 mm should be avoided to protect the driver. Therefore, when  $D_{sp}$  moves towards 40 mm ( $D_{sp} > 0$ ) and is larger than  $D_T = 10$  mm (denoted by sections A and C), large stiffness is applied ( $I_2 = 2A$ ). Similarly, when  $D_{sp}$  moves towards -40 mm ( $D_{sp} < 0$ ) and is smaller than  $-D_T = -10$  mm (denoted by sections B and D), large stiffness is also applied ( $I_2 = 2A$ ). For the rest sections except A, B, C and D, small stiffness is prescribed with  $I_2 = 0A$ . On the one hand, small stiffness is given in the small stroke when  $D_{sp} < |D_T|$  so that a small vibration transmissibility is realized in the small stroke range. On the other hand, small stiffness is also prescribed for those with displacement larger than the threshold displacement  $D_{sp} \geq |D_T|$  but moves towards the neutral position 0 mm. With the arrangement in the large stroke displacement range: giving large stiffness when displacement moves towards  $\pm 40$  mm while prescribing small stiffness when displacement moves towards neutral position 0 mm, energy can also be dissipated by the VSVD dampers' spring at a large stroke displacement range. For instance, damper 2 will be powered at the beginning of section A, after which casing 2 moves together with rotor 2 and the VSVD dampers' spring is continuously stretched. Meanwhile, energy is stored in the stretched spring. Then at the end of section A, damper 2 is not powered, and casing 2 can move relative to rotor 2. Therefore, the stretched spring will be loosed. As the spring force is not acting on the VSVD dampers after the end of section A, the stored energy in section A is dissipated. Hence, the proposed stiffness control strategy not only can provide a small stiffness in the small stroke ranges to ensure small transmissibility but also can dissipate vibration energy in the large stroke range.

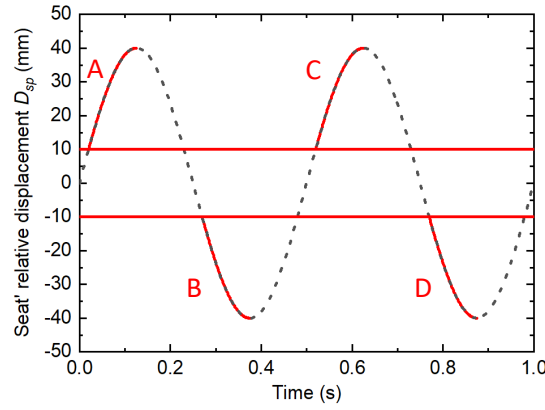


Figure 5.6. Stiffness control strategy demonstration.

#### 5.4 Numerical evaluation of the VSVD seat suspension

In this section, the mathematical model of the proposed seat suspension is established at first, and then the seat suspension's vibration control performance is evaluated by the mathematical simulation.

##### 5.4.1 Mathematical modelling of the seat suspension.

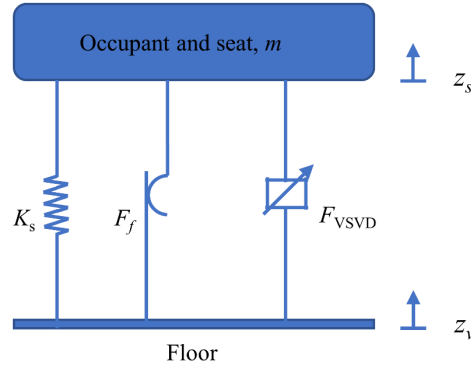


Figure 5.7. The mathematic model of VSVD seat suspension.

**Figure 5.7** shows the VSVD seat suspension model coupled with occupant and seat. The top plate of the seat suspension connects the occupant on the top side, and the base plate connects the vehicle floor on the bottom side. The governing equation for the system is expressed as:

$$m\ddot{z}_s = -K_s(z_s - z_v) - F_{VSVD} - F_f \quad (5-3)$$

where  $m$  is the total mass of the occupant and the seat, and it is set as 86.6 kg according to the experiment setup.  $K_s$  denotes the equivalent stiffness of the suspension's spring.  $z_s$  and  $z_v$  represent the displacements of the seat and the floor, respectively.  $F_f = 24$  N is the

structure's friction, and  $F_{VSVD}$  means the damper force in the vertical direction which is transferred from two VSVD dampers' torque output  $T_{VSVD}$  through the scissors structure.

According to the geometrical relationship indicated in **Figure 5.1(b)** and two VSVD dampers are working,

$$(F_{VSVD}/2) \times w = 2T_{VSVD} \quad (5-4)$$

Therefore,  $F_{VSVD}$  can be expressed as

$$F_{VSVD} = 4T_{VSVD}/w = 4T_{VSVD}/\sqrt{L_0^2 - H(t)^2} \quad (5-5)$$

where  $L_0 = 287$  mm is the length of beam 2;  $H(t)$  is the vertical length of the two joints of beam 2 in real-time;  $w$  is the vertical displacement of beam 2's two joints.  $T_{VSVD}$  is the torque output of one VSVD dampers.

The mathematical model for a VSVD damper was shown in **Figure 5.8**. When rotor 1 has a relative rotation  $\varphi_1$  to casing 1 with  $I_1$  applied on damper 1, a damping torque  $T_{damper 1}$  is generated. Additionally, if current  $I_2$  is applied on damper 2, casing 2 will rotate following rotor 1 & rotor 2. Meanwhile, casing 2 will also have a relative rotation  $\varphi_2$  to casing 1, so the spring is stretched with a spring torsion torque  $T_s$  generated. Therefore  $T_{VSVD}$  is the combination of the damper 1's output torque  $T_{damper 1}$  and the spring's output  $T_s$ , and it is expressed as

$$T_{VSVD} = T_{damper 1} + T_s \quad (5-6)$$

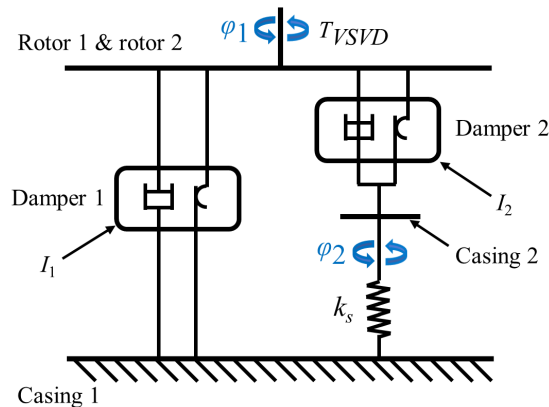


Figure 5.8. The mathematic model of a VSVD damper.

The VSVD damper contains two MR dampers with identical structural design. For one MR damper, damping torque is generated due to the shear motion between the rotor

and casing. As shown in **Figure 5.1**, the areas where such shear motion happens in damper 1 are marked and numbered 0 to 5, considering the symmetric structure of the damper. Refer to equations (8)- (12) in [68], the output torque of one damper, either damper 1 or damper 2, can be calculated as:

$$T_0 = \frac{4\pi\mu_{eq}R_4^4}{(n_0+3)d} \left(1 - \left(\frac{R_0}{R_4}\right)^{n_0+3}\right) \Omega + \frac{4\pi\tau_0}{3} (R_4^3 - R_0^3) + 4\pi\tau_0 R_i^2 L_i + 4\pi k_0 \left(\frac{\Omega}{d}\right)^{n_0} R_i^{2+n_0} L_i \quad (5-7)$$

$$T_i = \frac{4\pi\mu_{eq}R_4^4}{(n_0+3)d} \left(1 - \left(\frac{R_0}{R_4}\right)^{n_0+3}\right) \Omega + \frac{4\pi\tau_0}{3} (R_4^3 - R_0^3) + 2T_1 + 2T_2 + 2T_3 + 2T_4 + T_5 \quad (5-8)$$

$$T_i = 2\pi R_i^2 L_i \left( \tau_{yi} + K_i \left( \frac{\Omega R_i}{d} \right)^{n_i} \right), i=1, 2, 3, 4, 5$$

where  $T_0$  and  $T_i$  are outputs for one damper without- and with- magnetic field applied.  $d$  denotes the MRF gap and it is 0.5 mm.  $R_i$  and  $L_i$  are the radius and the length of  $i$ -th working areas shown in **Figure 5.2** and the value for them are given in **Table 5.1**.

Table 5.1. Dimensions of the working areas (mm)

L <sub>1</sub>	L <sub>2</sub>	L <sub>3</sub>	L <sub>4</sub>	L <sub>5</sub>	R <sub>0</sub>	R <sub>1</sub>	R <sub>2</sub>	R <sub>3</sub>	R <sub>4</sub>	R <sub>5</sub>
15	15	15	15	4	14	22	26	30	34	34

The rheological properties  $K_i$ ,  $\tau_{yi}$ , and  $n_i$ , are the consistency, yield stress, and the behaviour index of the MR fluids in the  $i$ th working area, respectively. These three parameters can be estimated by the Hershel-Bulkley (H-B) model [135]

$$Y = Y_\infty + (Y_0 - Y_\infty)(2e^{-B\alpha_{sY}} - e^{-2B\alpha_{sY}}) \quad (5-9)$$

where  $Y$  represents these terms.  $Y_0$  and  $Y_\infty$  represent the values of these rheological properties at the zero-field state and the magnetic saturation state, respectively. As for the exponential terms, within the indices,  $\alpha_{sY}$  is the saturation moment index. Referenced from [18], the values of  $Y_0$ ,  $Y_\infty$  and  $\alpha_{sY}$  of the MR fluid (Lord MRF-132DG) are given in **Table 5.2**. For instance,  $\tau_y$  can be calculated by replacing  $Y_\infty$ ,  $Y_0$  and  $\alpha_{sY}$  in **Equation (5-9)** with  $\tau_{y_\infty}$ ,  $\tau_{y_0}$  and  $\alpha_{s\tau_y}$ , respectively.

$B$  in **Equation (5-9)** is the magnetic flux density in the MR fluid. A magnetic field simulation using COMSOL Multiphysics (COMSOL Inc) was conducted to obtain the relation between the magnetic flux density in each working areas and the applied current. The simulated magnetic field distribution with 2 A current applied is illustrated

in **Figure 5.9(a)**. **Figure 5.9(b)** provides the relationship between the mean flux density at each MR fluids working areas and the applied current. The result indicates that the mean flux density in all working areas increases with the increase of the applied current. Area 1 has the maximum magnetic flux density and area 5 has the minimum.

Table 5.2. Parameters for MR fluid (Lord MRF-132DG) [18]

$\tau_{y_0}$	10 Pa	$\tau_{y_\infty}$	30 000 Pa	$\alpha_{s\tau_y}$	$2 \text{ T}^{-1}$
$K_{e0}$	$0.22 \text{ Pa}\cdot\text{s}^n$	$K_{e_\infty}$	$3900 \text{ Pa}\cdot\text{s}^n$	$\alpha_{sk}$	$5 \text{ T}^{-1}$
$n_0$	0.917	$n_\infty$	0.25	$\alpha_{sn_e}$	32

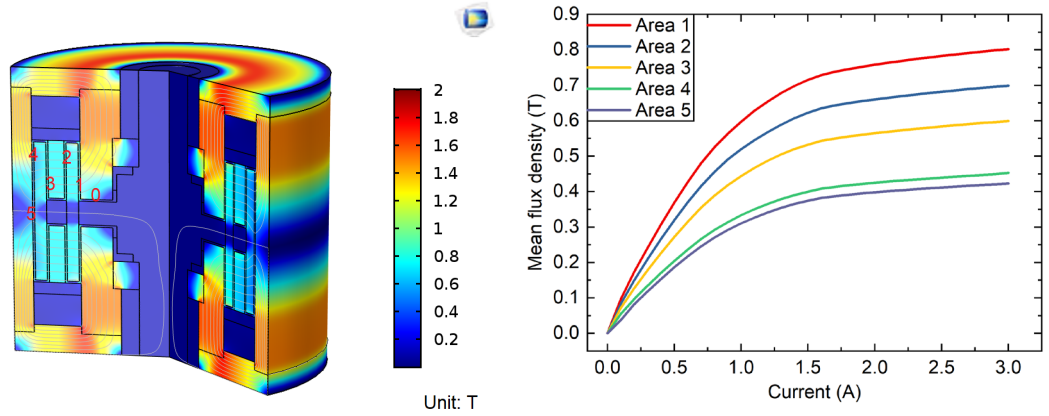


Figure 5.9. Magnetic field simulation.

Based on the result of **Figure 5.9(b)**, polynomial fitting equations for each MR fluids working areas were obtained to represent the relation between the mean magnetic flux and the applied current:

$$B_1 = 0.05151 I_1^3 - 0.36888 I_1^2 + 0.91112 I_1 + 0.00266 \quad (5-10)$$

$$B_2 = 0.04415 I_1^3 - 0.31785 I_1^2 + 0.7897 I_1 + 0.00195 \quad (5-11)$$

$$B_3 = 0.03766 I_1^3 - 0.27121 I_1^2 + 0.67495 I_1 + 0.00116 \quad (5-12)$$

$$B_4 = 0.02823 I_1^3 - 0.20291 I_1^2 + 0.50543 I_1 + 0.00156 \quad (5-13)$$

$$B_5 = 0.02602 I_1^3 - 0.18991 I_1^2 + 0.479 I_1 - 0.00649 \quad (5-14)$$

$\mu_{eq}$  in **Equations (5-7) and (5-8)** is the equivalent viscosity of MR Fluids, and it is calculated by

$$\mu_{eq} = K_e \left( \frac{R_0 \Omega}{d} \right)^{n_e - 1} \quad (5-15)$$

Spring's output torque  $T_s$  is expressed as

$$T_s(t) = k_s \varphi_2(t) \quad (5-16)$$

where  $k_s$  is spring's stiffness.  $\varphi_2$  is the relative displacement of casing 2 to casing 1. If  $T_s(t)$  is smaller than  $T_{damper\ 2}(t)$ , damper 2 is not yielded and casing 2 will rotate together with rotor 1 & rotor 2 at the same velocity. When the  $T_s(t)$  is larger enough to yield  $T_{damper\ 2}(t)$ , casing 2 will stop rotation and keep still. Based on these analyses, it has

$$\begin{aligned} \text{If } T_s(t) &\leq T_{damper\ 2}(t) \\ \dot{\varphi}_2(t) &= \dot{\varphi}_1(t) \\ \text{Elseif } T_s(t) &= T_{damper\ 2}(t) \\ \dot{\varphi}_2(t) &= 0 \end{aligned} \quad (5-17)$$

$\Omega$  in **Equations (5-7) and (5-8)** is the relative angular velocity between rotors and the casings to calculate damper torques  $T_{damper\ 1}$  and  $T_{damper\ 2}$ . For damper 1, the relative velocity between rotor 1 and casing 1 is  $\dot{\varphi}_1$ . As rotor 1 and casing 1 are mounted on beam 1 and beam 2, respectively, the angular displacement of rotor 1 and casing 1:  $\varphi_1$  can be represented by the angular displacement of beam 1 and beam 2. According to the geometrical relation of the scissors structure shown in **Figure 5.1(b)**,  $\varphi_1(t) = 2\theta(t)$ , and  $\sin(\theta(t)) = H(t) / L_0$ . Therefore  $\varphi_1(t)$  is expressed as

$$\varphi_1(t) = 2\sin^{-1}(H(t) / L_0) \quad (5-18)$$

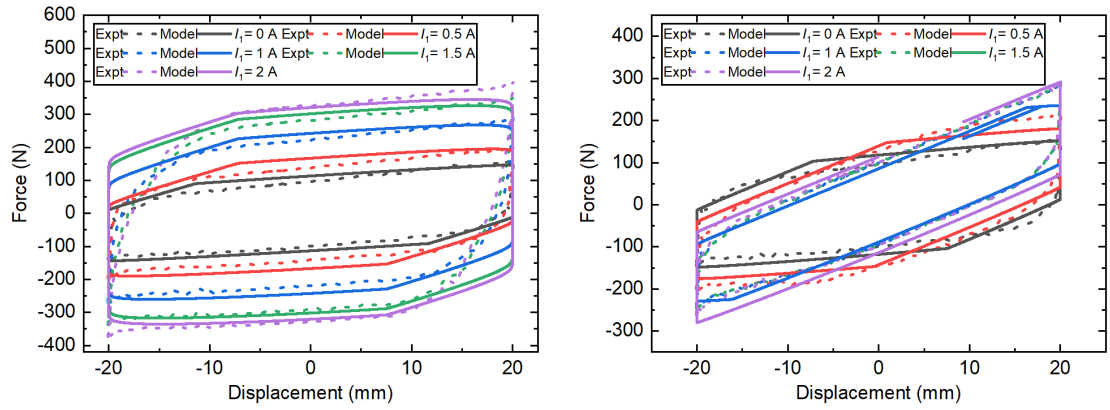
Hence, the relative velocity is

$$\dot{\varphi}_1(t) = 2 \cdot \frac{1}{L_0 \sqrt{1 - \left( \frac{H(t)}{L_0} \right)^2}} \cdot \frac{d}{dt}(H(t)) = 2 \cdot \frac{1}{L_0 \sqrt{1 - \left( \frac{H(t)}{L_0} \right)^2}} \cdot (z_s - z_v) \quad (5-19)$$

For damper 2, the relative velocity between rotor 2 and casing 2 is  $\dot{\varphi}_1(t) - \dot{\varphi}_2(t)$ .  $\dot{\varphi}_2(t)$  can be obtained by **Equation (5-17)**. When applied with current, casing 2 will follow the rotation of rotor 1 & rotor 2. In contrast, it will return to the initial position immediately once the current changed back to 0 because damper 2's output torque will become 0 and is not able to hold the stretched spring. Therefore,  $\varphi_2(t)$  is expressed as

$$\varphi_2(t) = \begin{cases} \int \dot{\varphi}_2(t) dt, & I_2 > 0 \text{ A} \\ 0, & I_2 = 0 \text{ A} \end{cases} \quad (5-20)$$

With the above equations, the mathematic model was established in the MATLAB/Simulink. Applying the model with identical displacement and current conditions of the property test, modelled force-displacement results are obtained and compared with experimental results in **Figure 5.10**. The good accordance between the modelled results and the experimental results in both variable damping and variable stiffness comparisons indicates that the established model can prescribe the behaviour of the suspension very well.



(a) variable damping comparison

(b) variable stiffness comparison

Figure 5.10. Model verification by comparing experimental and simulation results.

#### 5.4.2 Numerical simulation results and analysis.

To evaluate the vibration control performance of the proposed VSVD seat suspension, numerical simulation with the established mathematical model using MATLAB/Simulink module is conducted. To be specific, the response of the occupant and seat can be obtained with the vibration excitation of the vehicle floor ( $z_v$ ) prescribed. Three excitation signals: harmonic signal, bamp signal and random signal are prescribed to evaluate the performance of the proposed VSVD seat suspension. Four control cases as follows are compared:

- 1) Passive on case.  $I_1(t) = 0 \text{ A}$  and  $I_2(t) = 2 \text{ A}$  are prescribed in this control case to represent a passive suspension with a small damping and a large stiffness. Considering the commercial seat suspension needs a large stiffness spring to meet the loading capacity requirement and avoid end-stop impact.



- 2) VD case. Damping is the only variable property in this case, and  $I_1(t)$  is regulated by the designed no jerk skyhook control strategy.  $I_2(t) = 2$  A is also prescribed to make sure the suspension has a large stiffness. This control case is to simulate a seat suspension with large stiffness and capable of vary its damping.
- 3) VS case. Stiffness is the only variable property in this case, and  $I_2(t)$  is regulated by the variable stiffness control strategy.  $I_1(t) = 0$  A is given to provide small damping.
- 4) VSVD case. Both the damping and stiffness are controlled in this case, and  $I_1$  and  $I_2$  are regulated by their control strategies to vary damping and stiffness simultaneously.

#### *Harmonic signal simulation*

Firstly, simulations of harmonic signals from 1 to 3 Hz with an increment of 0.1 Hz were conducted to obtain the transmissibility of the system, which is defined as the vibration amplitude ratio of the seat to floor. The result presented in **Figure 5.11** shows that the natural resonance frequency for the seat suspension is around 1.6 Hz. VSVD case has the smallest transmissibility in the whole frequency range, denoting the VSVD case has the best vibration control performance in all cases. Besides, both VD and VS cases perform better than Passive on case.

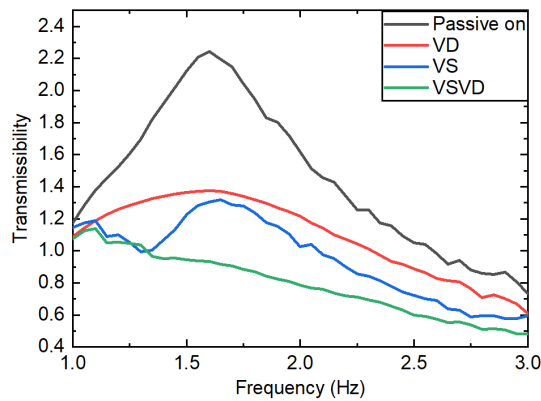
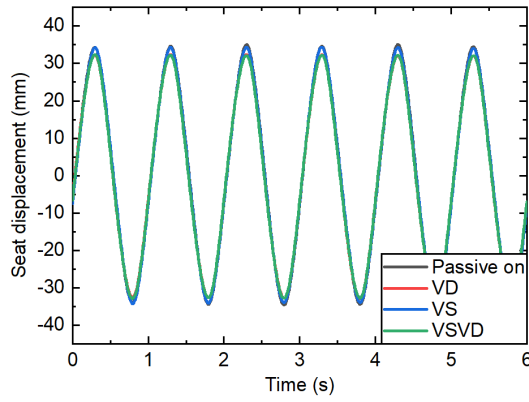


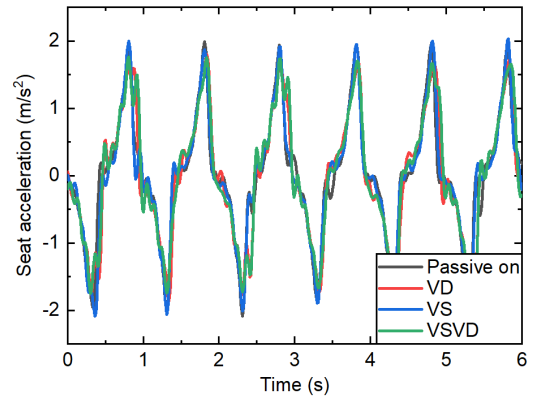
Figure 5.11. Simulated Transmissibility.

The seat displacement and acceleration results of three frequencies: 1, 1.6 and 3 Hz that represent small frequency, resonance frequency and larger frequency are presented in **Figure 5.12**. The seat displacement and acceleration of VD case and VSVD case have almost the same small values at 1 Hz and VD case and VSVD case works better than others at this frequency. VSVD case has the best vibration control performance at

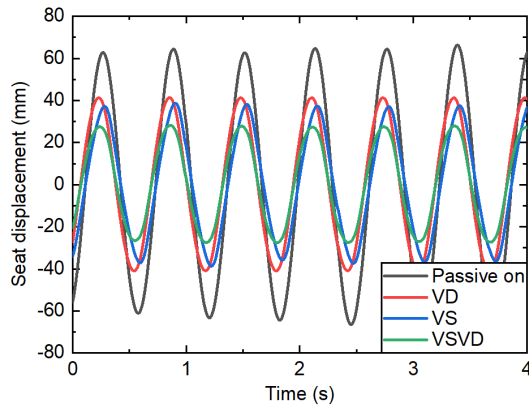
1.6 and 3 Hz. The largest performance improvement of VSVD case is at the resonance frequency of 1.6 Hz.



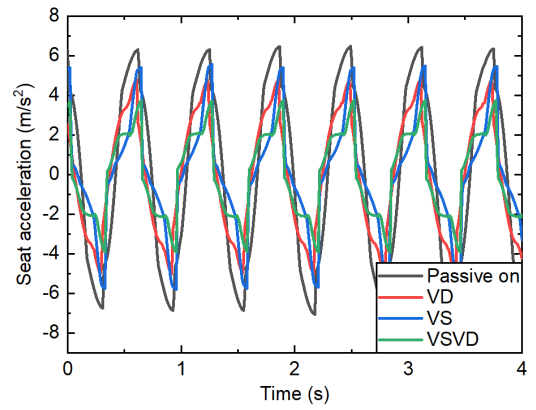
(a) Seat displacement (1 Hz)



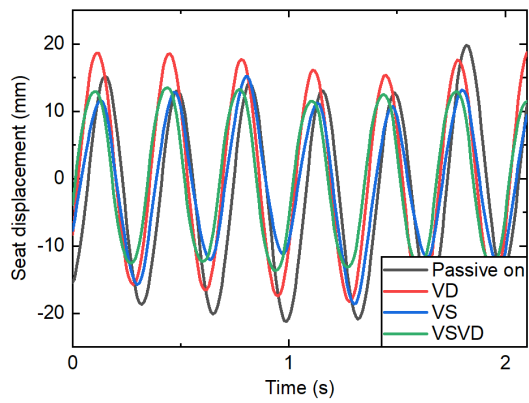
(b) Seat acceleration (1 Hz)



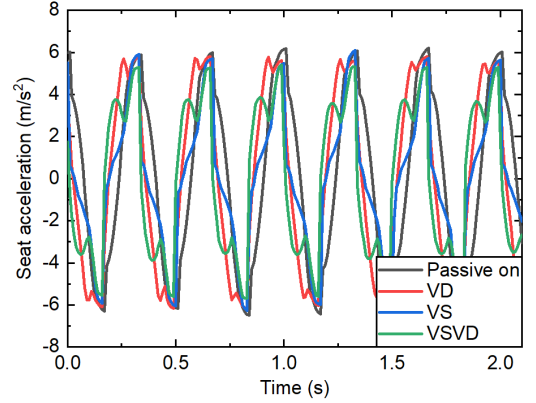
(c) Seat displacement (1.6 Hz)



(d) Seat acceleration (1.6 Hz)



(e) Seat displacement (3 Hz)



(f) Seat acceleration (3 Hz)

Figure 5.12. Simulated seat displacement and acceleration response.

### Bump signal excitation simulation

Bump signal simulation are conducted to evaluate the proposed VSVD seat suspension's instantaneously response performance. As shown in **Figure 5.13**, VS case and VSVD case have much smaller displacement and acceleration amplitude than Passvie on case and VD case. The peak-to-peak data listed in **Table 5.3** shows that VSVD case performs best among the four cases, with 44.51% of displacement and 52.05% acceleration reduced.

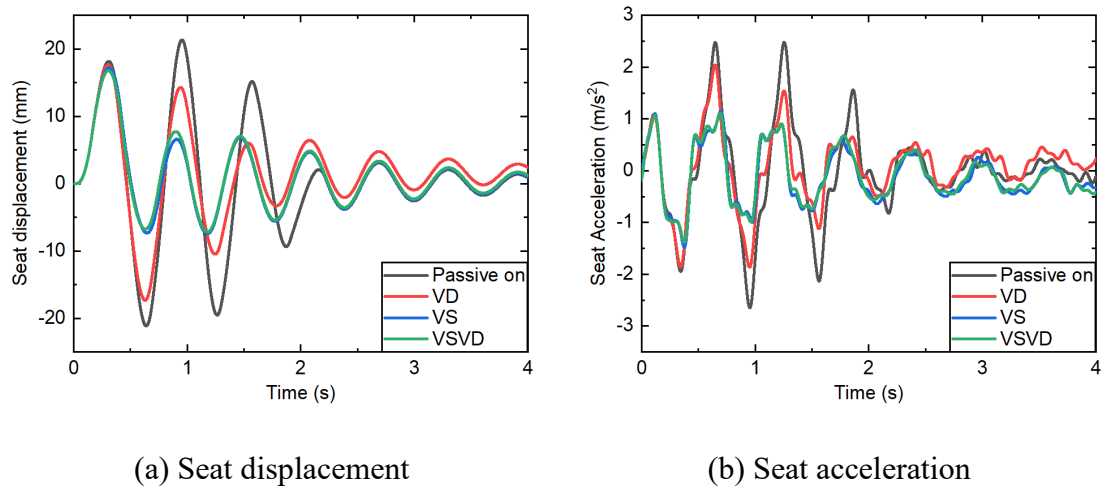


Figure 5.13. Bump signal excitation simulation results

Table 5.3. Peak to peak displacement and acceleration

	Passive on	VD	VS	VSVD
Peak to peak displacement (mm)	42.44	34.96	24.52	23.55
Displacement reduced proportion	NA	17.62%	42.22%	44.51%
Peak to peak acceleration ( $\text{m/s}^2$ )	5.11	3.90	2.57	2.45
Acceleration reduced proportion	NA	23.68%	49.70%	52.05%

### Random signal excitation simulation

Following harmonic signal tests, the performance of the seat suspension was finally evaluated under a random signal simulation. The displacement and acceleration of the seat in the time domain (**Figure 5.14** and **Figure 5.15(a)**) indicate that vibration is reduced if VD or VS control are applied. VSVD case posses the best vibration control performance than other cases. The main frequency of the vibration was found to be 1.64

Hz in **Figure 5.15(b)**. At this frequency, VSVD case performs a 34.72% amplitude reduction of Passive on case with the amplitude reduced from 0.72 to 0.47.

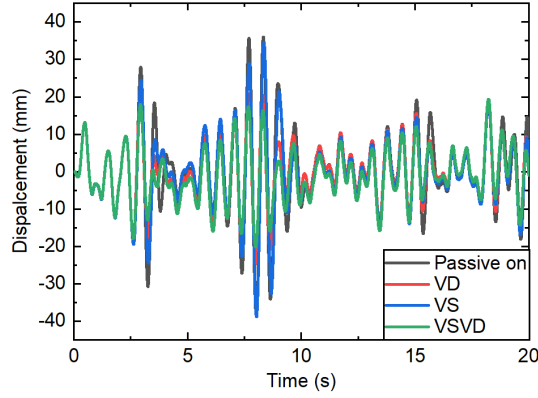


Figure 5.14. Displacement response results of random signal excitation simulation

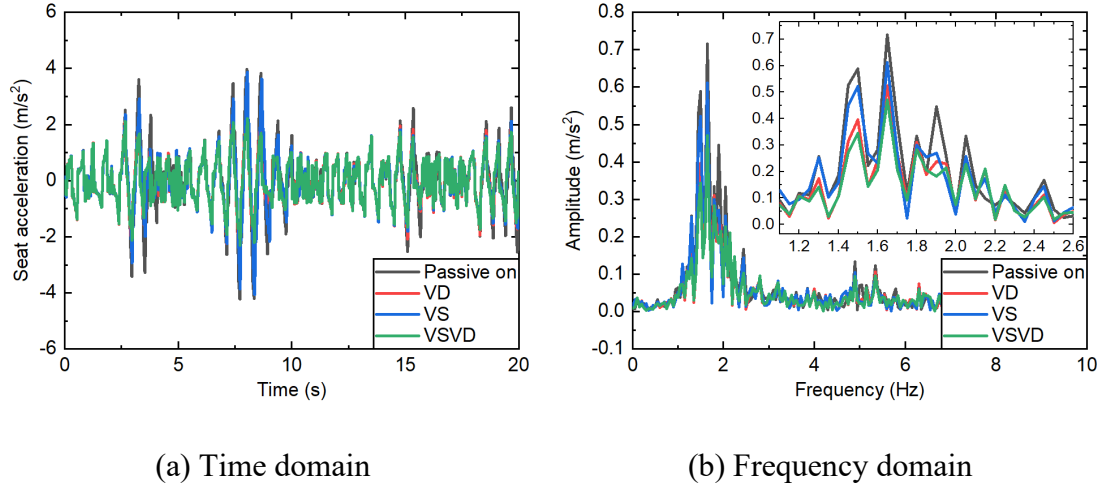


Figure 5.15. Acceleration response results of random signal excitation simulation

Root mean square (RMS) acceleration is an index to evaluate the vibration amplitude. According to ISO 2631-1 [136], the frequency weighted-RMS (FW-RMS) is related to ride comfort and the fourth power vibration dose value (VDV) is another index more sensitive to peak values so as to evaluate shock vibration performance. The results of the four control cases with the above three indexes are demonstrated in **Figure 5.16**. The VSVD case has the smallest magnitude in all indexes, indicating the best vibration reduction performance. To be specific, VSVD case reduced 30.63% in RMS, 26.09% in FW-RMS and 36.70% in VDV. The reduction in RMS and FW-RMS indicate the proposed VSVD seat suspension can provide the best ride comfort and the VDV result also proved that the VSVD case has the best performance regarding shock vibration.

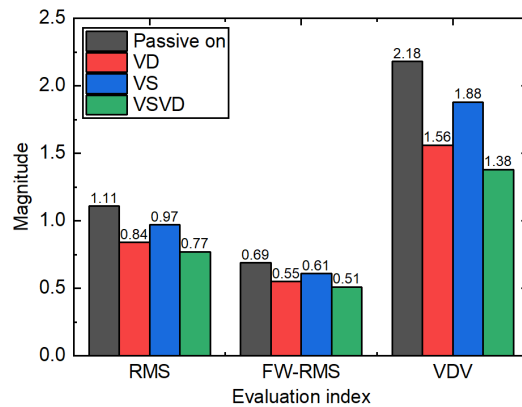


Figure 5.16. Vibration control performance compare

## 5.5 Experimental verification of the VSVD seat suspension

Following the numerical evaluation, the performance of the proposed VSVD seat suspension was experimentally evaluated in this section. The test system setup is firstly introduced in Section 5.5.1. Then the experimental results of the four control cases under the excitation signals are presented and analysed in Section 5.5.2.

### 5.5.1 Test system setup

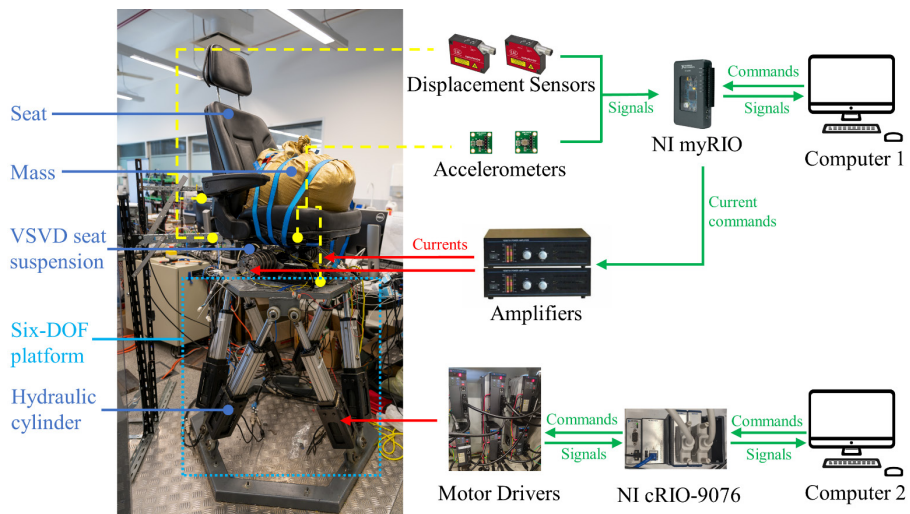


Figure 5.17. Experimental test setup.

As shown in **Figure 5.17**, the proposed VSVD seat suspension together with a commercial vehicle seat fixed to a six-DOF-platform that can provide prescribed vertical vibrations. Meanwhile, a 66.6 kg mass is loaded on the seat to simulate the driver's body. The total weight of the mass and the seat loaded on the seat suspension is 86.6 kg. Computer 2 can give commands to motor drivers through a NI cRIO-9076 to control the six hydraulic cylinders so that a prescribed vertical vibration excitation is

given to the seat suspension system, stimulating a vibration excitation of car body caused by road unevenness. Two displacement sensors: Micro Epsilon ILD 1302-200 and ILD 1302-100 are mounted on a stand to measure the displacements of the seat and the platform for obtaining data of  $z_s$  and  $z_v$ , respectively. Meanwhile, to record their accelerations, two accelerometers (ADXL203EB) are also fixed to the seat and platform, respectively. All these measured data is feedback to computer 1 through a NI myRIO. Then, current commands generated by the programmed control strategy are given to the amplifiers to power the VSVD dampers.

### 5.5.2 Test results and analysis

#### *Harmonic signal tests*

Transmissibility obtained by the displacement vibration amplitude ratio of the seat to the platform in the range from 1 to 3 Hz is also demonstrated in **Figure 5.18**. It is seen that the resonant frequency of the Passive on seat suspension is 1.8 Hz, which is different from the simulated resonant frequency of 1.6 Hz. This may be caused by the difference between simulation and the experiment in reality. The resonant frequency shifts left to 1.5 Hz for VS case, with smaller transmissibility than Passive on case. VD case reduced the transmissibility at small-frequency range from 1 to 1.9 Hz, but increased the transmissibility a bit at a frequency higher than 1.9 Hz. By simultaneously varying damping and stiffness, the VSVD case has an excellent performance in the whole frequency range, even though works worse than the VS case in the large-frequency range but still perform better than Passive on and VS cases. Similar to the above analysis, VSVD case has the largest improvement at the resonant frequency of 1.8 Hz, with transmissibility reduced 64.45%

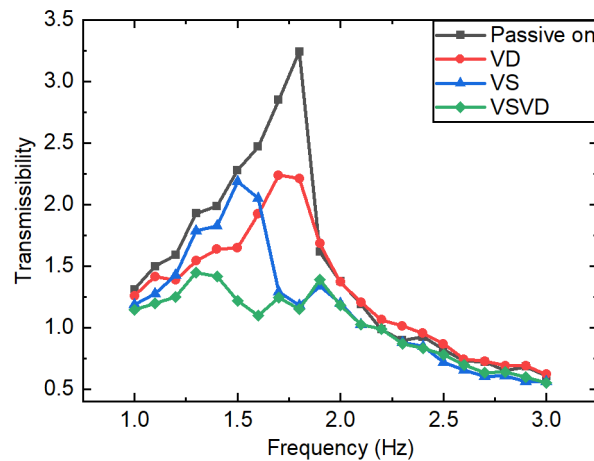
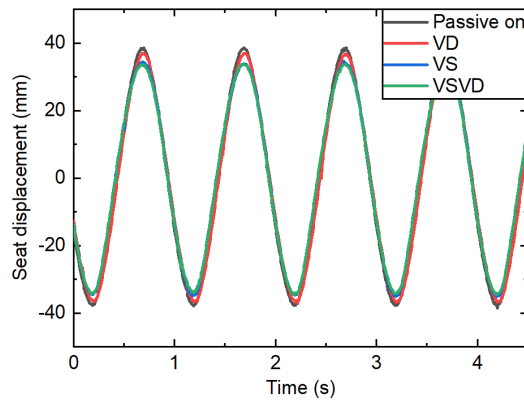
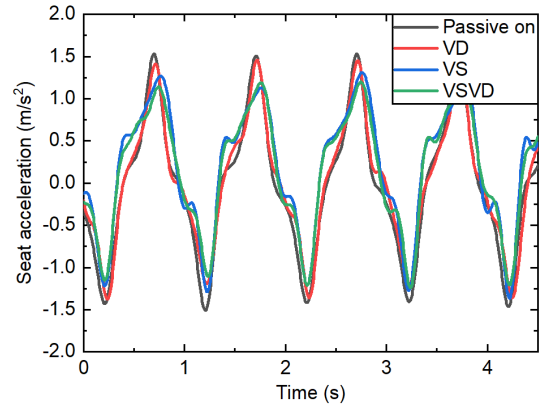


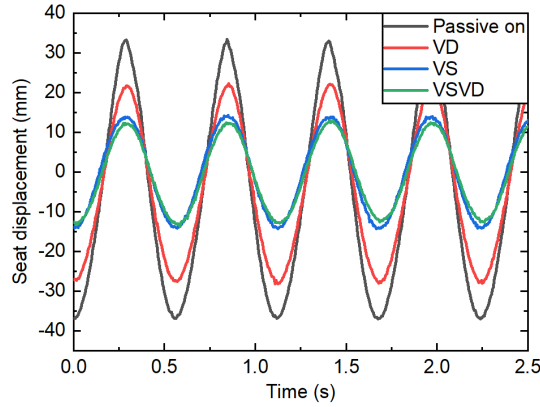
Figure 5.18. Transmissibility compare.



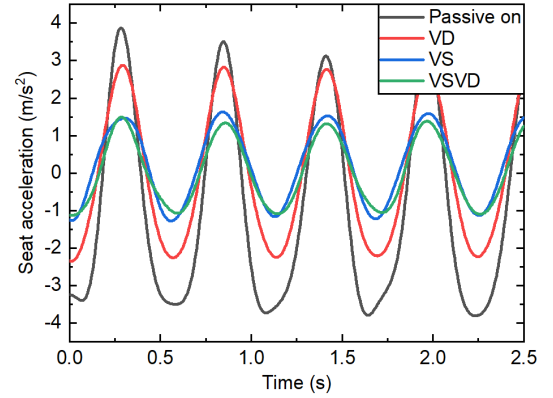
(a) Seat displacement compare 1 Hz



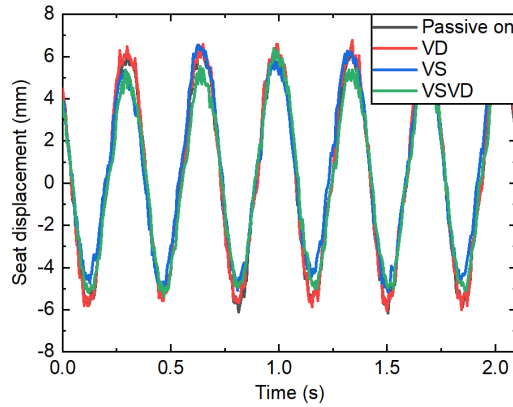
(b) Seat acceleration compare 1 Hz



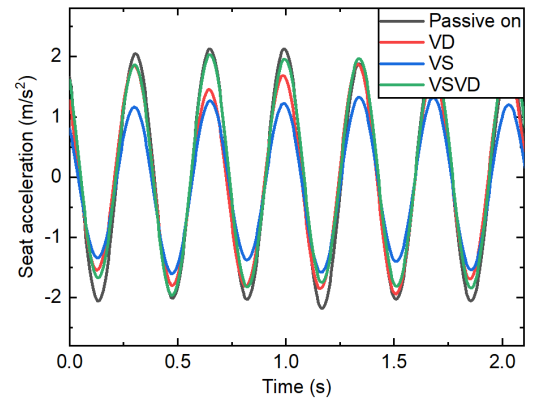
(c) Seat displacement compare 1.8 Hz



(d) Seat acceleration compare 1.8 Hz



(e) Seat displacement compare 3 Hz



(f) Seat acceleration compare 3 Hz

Figure 5.19. Result of three typical harmonic signals

**Figure 5.19** shows typical responses of seat displacement and seat acceleration under small (1Hz), medium/resonant (1.8 Hz) and large frequency (3Hz). At both 1 and 1.8 Hz, VD and VS cases work better than Passive on cases with smaller seat displacement and acceleration values. VSVD works best among all the cases. At the

resonant frequency 1.8 Hz, VSVD case has maximum reductions in seat displacement of 63.53% and in seat acceleration of 61.95%. At the large excitation frequency of 3 Hz, VS has the best vibration reductions performance in both seat displacement and acceleration. VSVD case still performs better than VD and Passive on case in seat displacement. Regarding seat acceleration, VSVD case works better than Passive on case but work worse than VD case.

#### Bump signal tests

Bump signal tests are conducted to evaluate the proposed VSVD seat suspension's instantaneously response performance. **Figure 5.20** shows the seat displacement and acceleration responses and **Table 5.4** summarises the peak-to-peak displacement and acceleration. It is seen that VS has the best performance in displacement, with 17.40 % of peak-to-peak displacement reduced compared to Passive on case. The VSVD has better performance than both Passive on case and VD case, with 11.29% peak-to-peak displacement reduced. In the aspect of seat acceleration, VSVD case has the best performance, with 25.99% of peak-to-peak acceleration reduced from 7.14 to 5.57  $\text{m/s}^2$ . From a general perspective, VSVD case performs superior to other cases in the bump excitation test.

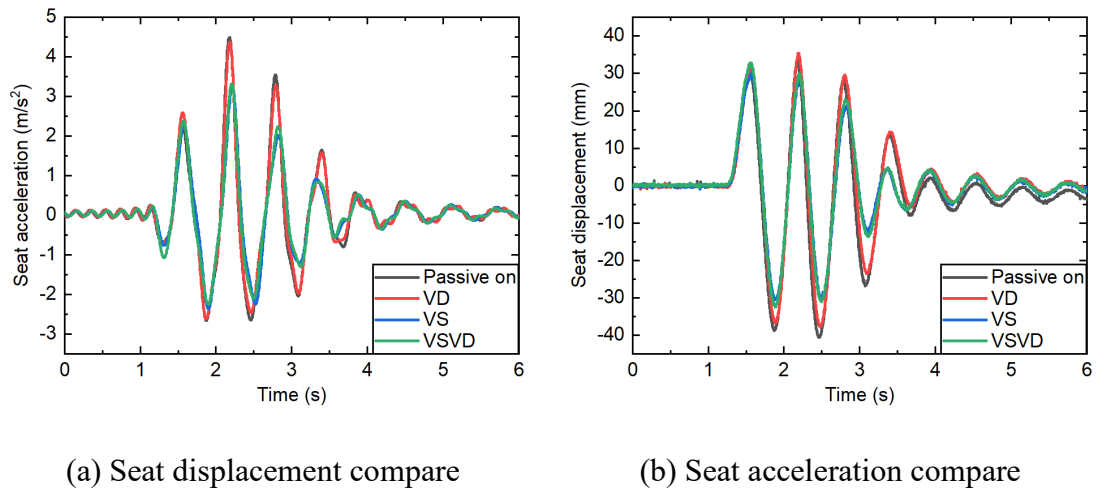


Figure 5.20. Bump excitation.

Table 5.4. Peak to peak displacement and acceleration (value/reduce proportion)

	Passive on	VD	VS	VSVD
Peak to peak displacement (mm)	74.05	73.20	61.17	65.69
Displacement reduced proportion	NA	1.15%	17.40%	11.29%



Peak to peak acceleration ( $\text{m/s}^2$ )	7.14	6.99	5.61	5.57
Acceleration reduced proportion	NA	2.10%	21.43%	21.99%

### *Random signal excitation*

Following the harmonic signal tests, the performance of the seat suspension was finally evaluated under a random signal. The seat displacement response presented in **Figure 5.21** indicates that VSVD case has the best performance.

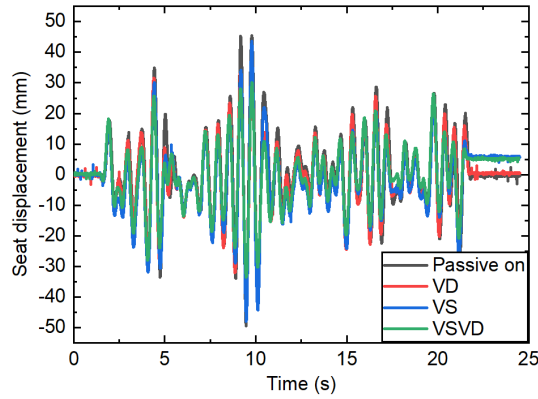


Figure 5.21. Seat displacement response.

To further evaluate the proposed VSVD seat suspension, seat acceleration in both the time- and frequency- domain are illustrated in **Figure 5.22**. The results also proved that the VSVD has the best performance in the random signal excitation tests. As shown in **Figure 5.22(b)**, the main frequency of the vibration is found to be 1.63 Hz, at which the amplitude of VSVD case reduced 25.13% compared to that of Passive on case.

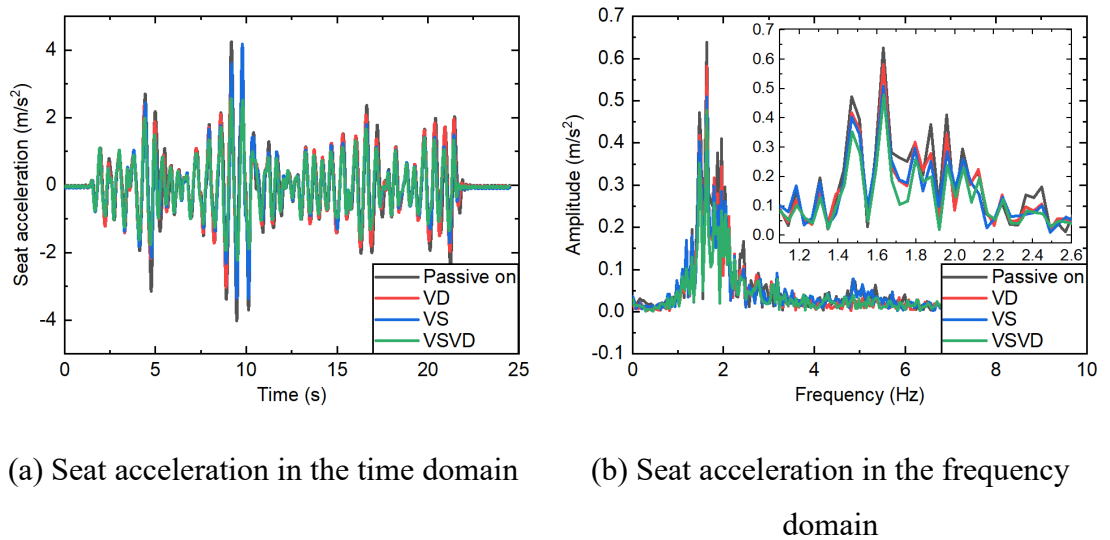


Figure 5.22. Seat acceleration in (a) time domain, (b) frequency domain.

The results of RMS, FW-RMS and VDV are concluded in **Figure 5.23**. It is noticed that VSVD case has the smallest values in these three indexes. Compared to Passive on case, VSVD case has magnitude reductions of 15.38%, 26.76% and 43.96% in RMS, FW-RMS and VDV, respectively. The reduction in RMS and FW-RMS indicate the proposed VSVD seat suspension can provide the best ride comfort. The VDV index also proved that the VSVD case has the best performance regarding shock vibration.

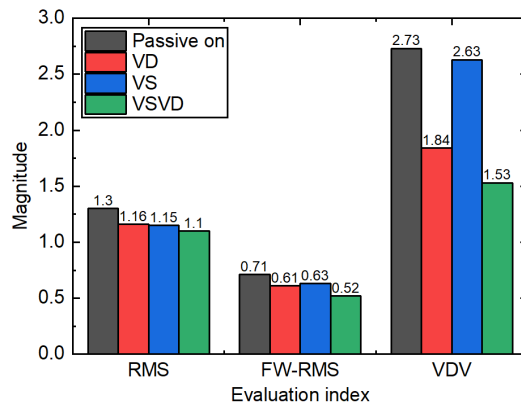


Figure 5.23. Vibration control performance comparison.

To sum up, based on the above analysis on the results of harmonic signals, the bump signal and random signal tests, it is easy to conclude that the proposed VSVD seat suspension can increase the ride comfort with an excellent vibration reduction performance

## 5.6 Conclusion

Vibration control of a seat suspension utilizing VSVD MR dampers to protect the drivers' mental and physical health is investigated in this Chapter. A VSVD seat suspension is proposed with the VSVD dampers designed. The characteristics of variable damping and stiffness of the VSVD seat suspension is verified by experimental property tests. With the current  $I_1$  increased from 0 to 2 A, the equivalent damping of the seat suspension increased 3 times from 1903.89 to 5806.61 N s/m. The effective stiffness also experienced a 5.34 times increase from 1468.69 to 7844.47 N/m. Numerical simulations and experimental tests under the excitations of harmonic signal, bump signal and random signal are conducted to evaluate the vibration performance of the seat suspension. Both the numerical simulation and experimental tests proved that the vibration is significantly reduced by the proposed VSVD seat suspension.

## Chapter 6

### Study on the impact protection performance of a rotary magnetorheological seat suspension

#### 6.1 Introduction

Recently, linear magnetorheological (MR) dampers have been widely utilised for impact protection of seat suspensions. However, the viscous force of linear MR dampers increases seriously with the increase of impact velocity. This results in a sharp increase of the total output force of the linear MR damper seat suspension (LMRSS), which may damage the suspension structure and lead to occupant injuries.

To address this issue, the performance of a seat suspension installed with a rotary MR damper (RMRSS) to improve the impact protection performance is investigated in this chapter. Specifically, A RMRSS was designed and introduced in Section 6.2. With the mathematical model of RMRSS and LMRSS established in Section 6.3, their velocity sensitivity and impact protection performance are evaluated in Section 6.4. Section 6.5 presents the experimental evaluation of RMRSS including its property tests and impact tests. Finally, the conclusion was drawn in Section 6.6.

#### 6.2 Mechanical structural design of RMRSS

As shown in **Figure 6.1(a)**, RMRSS is modified from a traditional seat suspension system with a rotary MR damper installed on the intersection of the scissor structure, which was simply pinned together in previous. Observed from one side, the top and base plates are connected by beam 1 and beam 2 via four joints. When the two plates move relatively in the vertical direction, the two beams will rotate relative to each other and the lower joint of beam 1 will move horizontally along the slider mounted on the base plate. The rotor and the cylinder of the rotary MR damper shown in **Figure 6.1(b)** are fixed with beam 1 and beam 2 respectively through a 10-time gearbox. Therefore, the relative vertical motion of the two plates will be transferred to the relative rotational motion of the rotor and the cylinder of the damper via the scissors structure. Thus, by controlling the damping torque of the damper via regulating the coil current, the damping of the structure is controlled. In addition, the pre-loaded spring mounted on the base plate is compressed, providing stiffness to the suspension.

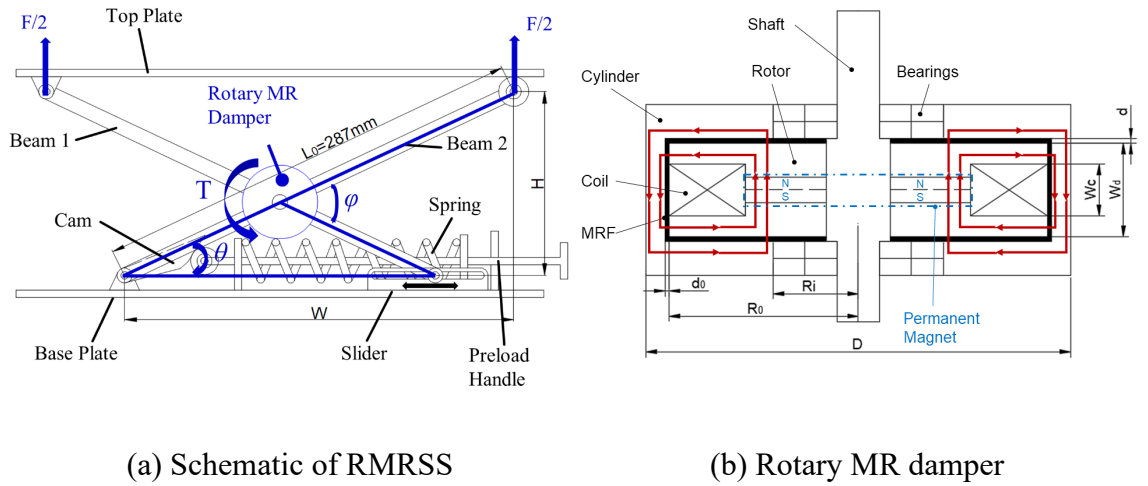


Figure 6.1. Schematic of RMRSS.

The rotary MR damper illustrated in **Figure 6.1(b)** consists of a cylinder fixed with beam 2, and a rotor fixed with beam 1. A permanent ring magnet is installed on the shaft of the rotor to provide an initial magnetic field. Along with this, a coil is wound on the rotor with 0.5 mm diameter copper wire with 500 turns to generate a controllable magnetic field. Provided with a positive current, the wound coil can generate a magnetic field in the same direction with the initial magnetic field provided by the magnet, so the magnetic flux is enhanced. Alternatively, the magnetic flux is reduced if a negative current is supplied. Given this hybrid arrangement, including both a permanent magnet and an electromagnet, a wider magnetic field range can be achieved than what an electromagnet is capable of on its own. MRF (MRF-132EG, Lord corp.) is then filled in the chamber between the rotor and the cylinder to facilitate the controllable damping torque within this system as the magnetic flux through the fluid is controlled. The geometric parameters of the rotary MR damper are provided in **Table 6.1**.

Table 6.1. Configurations of the rotary MR damper

$d_0$	1.5 mm	$D$	100 mm
$d$	1 mm	$R_i$	20 mm
$R_0$	44 mm	$w_d$	22 mm
$w_c$	12 mm		

Comparing the rotary MR damper with a linear MR damper, in which the MRF is required to move from one chamber to another through a narrow gap with a large velocity, the rotary MR damper does not need to make an MRF transfer in this sense.

Instead, continuous shearing of the MRF means that the large viscous force increase of the linear MR damper responding to the increase of impact velocity can be mitigated. Therefore, RMRSS will not possess such a large output force like that of LMRSS in high-velocity impact scenarios. Instead, it will have a similar level of output force performances during small and large impacts, so that the occupant will experience a similar acceleration and will not be injured by the large increase of an impact velocity. Based on this description, the rotary MR damper could theoretically be a better choice than the linear MR damper in the application of impact protection during high impact velocity scenarios, with systematic proof of this explored in later sections of this paper.

### 6.3 Mathematical modelling of RMRSS and LMRSS

In this section, the mathematical model of RMRSS is built for the numerical simulation evaluation in the following section. Additionally, to numerically compare the performance of RMRSS and LMRSS, the mathematical model of LMRSS is also established.

#### 6.3.1 Mathematical modelling of RMRSS

The peak torque of the rotary MR damper mounted on the scissors structure is calculated using the following equations [18, 68]:

$$T_\tau = \frac{4\pi\mu_{eq}R_0^4}{(n_e+3)d} \left[ 1 - \left( \frac{R_i}{R_0} \right)^{n_e+3} \right] \Omega + \frac{4\pi\tau_{ye}}{3} (R_0^3 - R_i^3) + 2\pi R_0^2 L_a \left[ \tau_{ye} + K_e \left( \frac{\Omega R_0}{d_0} \right)^{n_e} \right] \quad (6-1)$$

$$T_{\tau_0} = \frac{4\pi\mu_{eq_0}R_0^4}{(n_{e_0}+3)d} \left[ 1 - \left( \frac{R_i}{R_0} \right)^{n_{e_0}+3} \right] \Omega + \frac{4\pi\tau_{ye_0}}{3} (R_0^3 - R_i^3) + 2\pi R_0^2 W_d \left[ \tau_{ye_0} + K_{e_0} \left( \frac{\Omega R_0}{d_0} \right)^{n_{e_0}} \right] \quad (6-2)$$

where  $T_\tau$  and  $T_{\tau_0}$  are the damper torques with and without a magnetic field, respectively. The parameter  $\Omega$  represents the angular velocity of the rotary MR damper.  $L_a = w_d - w_c$  is the effective length of the annular duct. The rheological properties  $K_e$ ,  $\tau_{ye}$ , and  $n_e$ , are the consistency, yield stress, and the behaviour index of the MRF in the end-face duct, respectively. These three parameters can be estimated by the Hershel-Bulkley (H-B) model [135]:

$$Y = Y_\infty + (Y_0 - Y_\infty)(2e^{-Ba_{sY}} - e^{-2Ba_{sY}}) \quad (6-3)$$

where  $Y$  represents these terms.  $Y_0$  is the values of these rheological properties in the zero-field state, and  $Y_\infty$  represents the corresponding value at the magnetic saturation state. As for the exponential terms, within the indices,  $a_{sY}$  is the saturation moment

index, and  $B$  is the applied magnetic flux density. From [18], the values of  $Y_0$ ,  $Y_\infty$  and  $\alpha_{sY}$  of the MR fluid (Lord MRF-132DG) are given in **Table 6.2**. For instance,  $\tau_y$  can be calculated by replacing  $Y_\infty$ ,  $Y_0$  and  $\alpha_{sY}$  in **Equation (6-3)** with  $\tau_{y_\infty}$ ,  $\tau_{y_0}$  and  $\alpha_{s\tau_y}$ , respectively.

Table 6.2. Parameters for MR fluid (Lord MRF-132DG) [18]

$\tau_{y_0}$	10 Pa	$\tau_{y_\infty}$	30 000 Pa	$\alpha_{s\tau_y}$	2 T <sup>-1</sup>
$K_{e0}$	0.22 Pa · s <sup>n</sup>	$K_{e_\infty}$	3900 Pa · s <sup>n</sup>	$\alpha_{sk}$	5 T <sup>-1</sup>
$n_0$	0.917	$n_\infty$	0.25	$\alpha_{sn_e}$	32

To calculate the MRF equivalent viscosity  $\mu_{eq}$  in **Equations (6-1) and (6-2)**, **Equation (6-4)** is applied:

$$\mu_{eq} = K_e \left( \frac{R_0 \Omega}{d} \right)^{n_e - 1} \quad (6-4)$$

As the rotary MR damper is mounted on the intersection of the two beams via a gearbox with a ratio of 10:1, the torque on the scissors structure is calculated as:

$$T = \begin{cases} 10 T_\tau, & B \neq 0 \\ 10 T_{\tau_0}, & B = 0 \end{cases} \quad (6-5)$$

According to the geometric relationship indicated in **Figure 6.1(a)**, the rotational torque  $T$  generated by the rotary MR damper will finally translate to the vertical damping force of the seat suspension  $F_R$  by:

$$F_R = 2T/w = 2T/\sqrt{L_0^2 - H(t)^2} \quad (6-6)$$

where  $L_0 = 0.287$  m is the length of beam 2 and  $H(t)$  is the vertical height of the top plate relative to the base plate as a function of time  $t$ .

So, the total vertical force of RMRSS  $F_{RMRSS}$  can be calculated from:

$$F_{RMRSS} = F_R + F_k + F_f \quad (6-7)$$

where  $F_k = K_1 x$  is the vertical force generated by the spring installed on the seat suspension,  $K_1$  represents the equivalent vertical stiffness of the structure due to the spring, and  $F_f = 64$  N is the fiction force of the structure.

As shown in **Figure 6.1(a)**,  $\varphi(t) = 2\theta(t)$ , and  $\sin(\theta(t)) = H(t) / L_0$ , which leads to:

$$\varphi(t) = 2\sin^{-1}(H(t)/L_0) \quad (6-8)$$

Therefore, the relative angular velocity of the two beams can be expressed as

$$\dot{\varphi}(t) = 2 \cdot \frac{1}{L_0 \sqrt{1 - \left(\frac{H(t)}{L_0}\right)^2}} \cdot \frac{d}{dt}(H(t)) = 2 \cdot \frac{1}{L_0 \sqrt{1 - \left(\frac{H(t)}{L_0}\right)^2}} \cdot V_{plates}(t) \quad (6-9)$$

where  $V_{plates}(t)$  is the relative velocity of the top and base plates. As the damper is connected to the two beams by a gearbox with 10:1 ratio, the angular velocity of the rotary MR damper  $\Omega$  should be 10 times of that of the two beams:  $\Omega = 10 \dot{\varphi}(t)$ .

### 6.3.2 Mathematical modelling of LMRSS

The schematic of LMRSS is illustrated in **Figure 6.2**. Unlike the design of RMRSS, the linear MR damper is installed between the top and base plates for LMRSS in a slanted position, with the original pin-joint connecting the two beams at their intersection. In this case, the relative displacement between the top and bottom plate transfers to the relative motion of the linear MR damper's movable piston and its cylinder. The electromagnetic coil wound on the piston can provide a magnetic field when it is supplied with current. The detailed geometric parameters of the modelled linear MR damper are provided in **Table 6.3**. Here should state that these parameters are selected to ensure that RMRSS and LMRSS have similar performances at the low-velocity working condition so as to create a fair comparison between them.

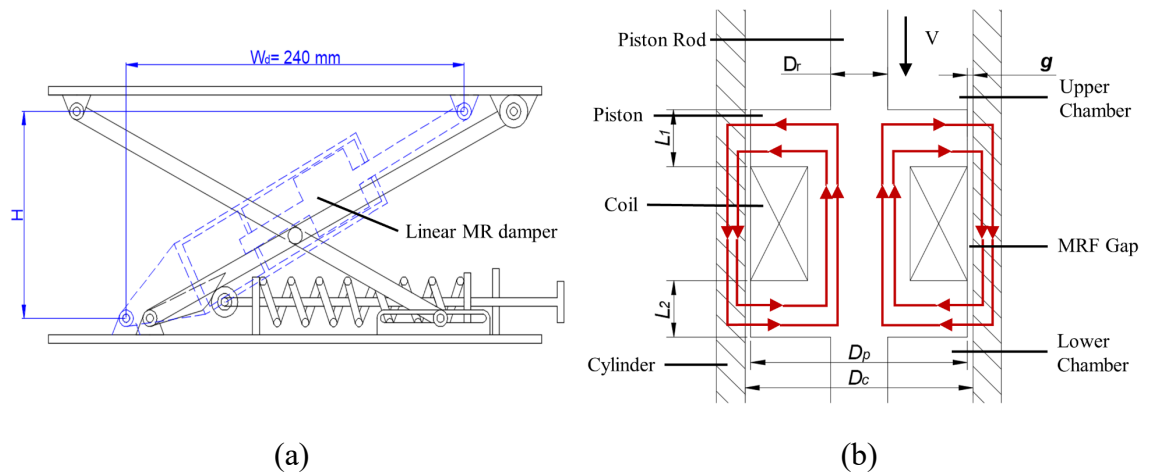


Figure 6.2. (a) Schematic of LMRSS; (b) mounted linear MR damper.

Table 6.3. Configurations of LMRSS

$D_r$	8 mm	$g$	0.8 mm
$D_p$	52.4 mm	$L_1$	12 mm
$D_c$	54 mm	$L_2$	12 mm

To begin the modelling of LMRSS, the output force of the linear MR damper  $F_l$  can be calculated by [137]:

$$F_l = F_\tau + F_\eta \quad (6-10)$$

$$F_\tau = A_e \Delta P_\tau \quad (6-11)$$

$$F_\eta = A_e \Delta P_\eta \quad (6-12)$$

where  $F_\tau$  and  $F_\eta$  are the yield force and the viscous force, respectively, generated by the pressure drop due to the yield stress of the MR fluid  $\Delta P_\tau$  and the Newtonian pressure drop  $\Delta P_\eta$ . The parameter  $A_e$  is the effective piston area, which can be expressed as:

$$A_e = A_p - A_r = \frac{1}{4} \pi (D_p^2 - D_r^2) \quad (6-13)$$

where  $A_p$  and  $A_r$  are the areas of the piston and the piston rod, respectively, with  $D_p$  and  $D_r$  being their corresponding diameters.

The pressure drop due to the yield stress  $\Delta P_\tau$  is given by

$$\Delta P_\tau = \frac{2L\tau_y}{g} \quad (6-14)$$

where  $L$  is the length of the active area and  $L = L_1 + L_2$  in this configuration. The parameter  $w_g$  is the MR fluid gap between the piston and the cylinder in the radial direction. Similar to RMRSS,  $\tau_y$  is the yield stress of the MR fluid, which can be calculated by using **Equation (6-3)**.

The pressure drop due to the yield stress  $\Delta P_\tau$  is given by

$$\Delta P_\eta = \frac{\rho f_d L V_g^2}{4g} \quad (6-15)$$

where  $\rho = 2.95 \text{ g/cm}^3$  is the density of the MR fluid,  $f_d$  is the Darcy friction factor, and  $V_g$  is the fluid velocity in the MR fluid gap. This can be obtained in terms of the piston



velocity  $V_p$ , i.e. the relative velocity of the piston and cylinder:

$$V_g = \frac{A_p - A_r}{A_g} V_p \quad (6-16)$$

$$V_p = \frac{H(t)}{\sqrt{H(t)^2 + W_d^2}} V_{plates} \quad (6-17)$$

where  $A_g$  is the cross-sectional area of the MR fluid gap in the radial direction, where  $A_g = A_c - A_p = \frac{1}{4}\pi(D_c^2 - D_p^2)$ . The parameter  $W_d$  is the horizontal displacement of the two joints of the installed linear MR damper.

To calculate the Darcy friction factor  $f_d$ , this depends on the Reynolds number  $Re$  [138]:

$$f_d = \frac{96}{Re}, \text{ if } Re \leq 2000 \quad (6-18)$$

$$f_d = (1-\alpha) \frac{96}{2000} + \alpha \frac{1}{\left\{ 1.8 \log_{10} \left[ \left( \frac{\varepsilon/2g}{3.7} \right)^{1.11} + \frac{6.9}{4000} \right] \right\}^2}, \text{ if } 2000 \leq Re \leq 4000 \quad (6-19)$$

$$f_d = \frac{1}{\left\{ 1.8 \log_{10} \left[ \left( \frac{\varepsilon/2g}{3.7} \right)^{1.11} + \frac{6.9}{Re} \right] \right\}^2}, \text{ if } Re \geq 4000 \quad (6-20)$$

where

$$\alpha = \frac{Re - 2000}{4000 - 2000} \quad (6-21)$$

and  $\varepsilon$  is the roughness of the internal cylinder wall, which is prescribed as 0.01 mm to represent a smooth wall condition. Lastly, in order to select an appropriate condition at a given time, the Reynolds number  $Re$  can be determined from:

$$Re = \frac{2\rho V_g g}{\eta} \quad (6-22)$$

where  $\eta = 0.112$  Pa·s is the viscosity of the MR fluid.

Combining **Equations (6-11) and (6-14)**, **Equations (6-12), (6-15) and (6-16)**, respectively, the yield force  $F_\tau$  and the viscous force  $F_\eta$  can be expressed as:

$$F_\tau = A_e \frac{2L\tau_y}{g} \quad (6-23)$$

$$F_\eta = A_e \frac{\rho f_d L \left( \frac{A_p - A_r}{A_g} \right)^2}{4g} V_p^2 \quad (6-24)$$

From the above equations, it can be known that the yield force  $F_\tau$  of a linear damper is independent of piston velocity  $V_p$ , while the viscous force  $F_\eta$  is quadratically related to  $V_p$ . Therefore, as the increase of piston velocity, the rapid parabolic rise of the viscous damping force leads to a sharp increase in the total output force of the linear MR damper.

For LMRSS, the vertical damping force of the seat suspension  $F_L$  is the vertical component of the linear MR damper  $F_l$ , described by:

$$F_L = F_l \frac{H(t)}{\sqrt{H(t)^2 + W_d^2}} \quad (6-25)$$

Hence, in this case, the total output force of LMRSS  $F_{LMRSS}$  is given by:

$$F_{LMRSS} = F_L + F_k + F_f \quad (6-26)$$

#### 6.4 Numerical evaluation of RMRSS and LMRSS

In order to evaluate the velocity sensitivity of RMRSS, transient analysis of velocity dependency of RMRSS and LMRSS are presented in this section. Additionally, dynamic impact protection performances of these two suspensions are compared.

##### 6.4.1 Transient output force analysis

Three levels of average magnetic flux density through the MR fluid:  $B = 0, 0.3$ , and  $0.6$  T, are selected to represent no magnetic flux, medium, and large magnetic flux, respectively. For the seat structures, the top plate has a maximum position of 250 mm, and a minimum position of 80 mm relative to the base plate. In this simulation, the neutral position with an occupant is set as 220 mm. The middle position of 150 mm, between the neutral and minimum positions, is then chosen to calculate the transient output forces of the two kinds of seat suspensions in order to compare their velocity sensitivities under a loaded condition. Based on this, the pre-load force of the spring,  $F_k = 350$  N, generated by the spring being compressed from the neutral position to the middle position, is added in the calculation of the total output force. Then providing an

instantaneous relative velocity  $V_{plates} = 0.1 \sim 5 \text{ m/s}$ , the corresponding transient output forces for RMRSS and LMRSS are calculated, with the results shown in **Figure 6.3**.

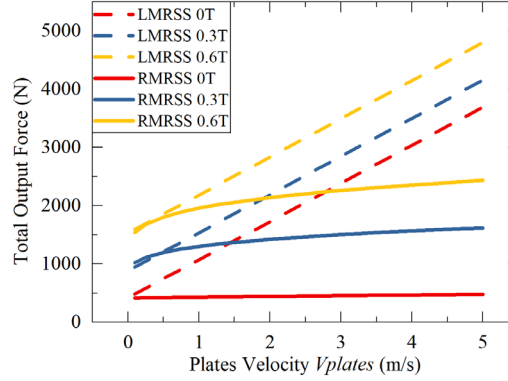


Figure 6.3. Force response to different impact velocities of RMRSS and LMRSS.

As shown in the Figure, the output forces of RMRSS and LMRSS with the contained MR fluid experiencing the same average magnetic flux density are quite similar at the minimum velocity of 0.1 m/s, and both of them increase with the increase of the plate velocity. However, the rate at which the output force of LMRSS increases is much larger than that of RMRSS. For instance, with a large magnetic flux density 0.6 T, the output force of LMRSS increases 3213.21 N across the total velocity range, which is more than 3 times larger than the increase of RMRSS, which is 895 N. The sharp output force increase of LMRSS is caused by the force increase of the linear MR damper, which is the result of the increase of the viscous force. In contrast, the mean rate of increase in the force of RMRSS is much lower and tends to saturate. As such, it can be concluded that RMRSS is less velocity-sensitive than LMRSS, and it can provide a more stable output force as the impact velocity on the seat suspension system increases.

#### 6.4.2 Dynamic impact simulations

Following the transient analysis, the dynamic simulation of the impact response of the seat suspensions coupled with an occupant is presented in this section. Firstly, the mechanical model for the occupied suspension system is established in **Figure 6.4**. The seat of mass  $M_I$  is connected to the floor of a vehicle through the MR seat suspension, with the top plate of the suspension connected to the seat and the base plate of the suspension mounted on the floor. The MR seat suspension includes three elements: the spring of effective vertical stiffness  $K_I$ , the MR damper force  $F_{MR}$ , and the friction force  $F_f$ . Here,  $F_{MR}$  is the vertical damping force of the MR dampers, either  $F_R$  or  $F_L$  for

RMRSS or LMRSS, respectively. Vertical displacements  $z_0$ ,  $z_1$ , and  $z_2$  are of the floor, the seat, and the occupant, respectively. The relative velocity of the top and base plates can be expressed as  $V_{plates} = \dot{z}_1 - \dot{z}_0$ . As for the occupant mass  $M_2$ , this rests on the seat through stiff cushioning material which is represented by the spring stiffness  $K_2$  and viscous damping  $C_2$ . According to [139], around 71% of the total weight of the occupant is supported by the seat, and the rest is supported by their feet on the floor. Therefore, in this simulation, the occupant mass is set as 55 kg to represent a 78 kg human. It is also assumed that this weight distribution remains the same during impacts, with any dynamic effects on the suspension system neglected for simplicity. Detailed parameters of the seat suspension system are listed in **Table 6.4**.

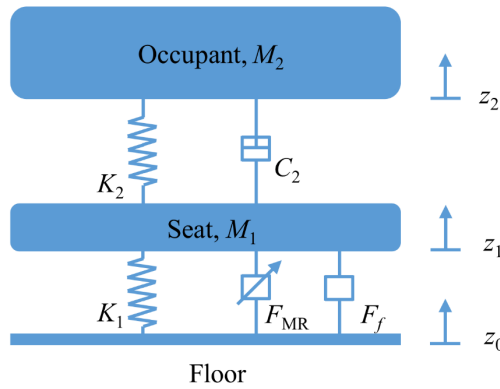


Figure 6.4. Mechanical model for the seat suspensions coupled with an occupant.

Table 6.4. Parameters for the seat suspension model

Parameters	$M_1$ (kg)	$M_2$ (kg)	$K_1$ (kN/m)	$K_2$ (kN/m)	$C_2$ (kN · s/m)
Value	10	55	5	80	2

When the seat suspension suffers an impact transferred through the floor, the motion of the MR seat suspension is governed by **Equations (6-27) and (6-28)**:

$$M_1 \ddot{z}_1 = -K_1(z_1 - z_0) - F_f - F_{MR} + K_2(z_2 - z_1) + C_2(\dot{z}_2 - \dot{z}_1) \quad (6-27)$$

$$M_2 \ddot{z}_2 = -K_2(z_2 - z_1) - C_2(\dot{z}_2 - \dot{z}_1) \quad (6-28)$$

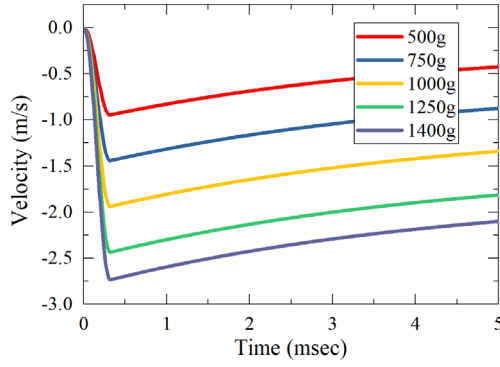
For military vehicles, the blast-induced impacts, particularly those caused by landmine explosions, may cause severe spinal injuries of the occupant. Such an impact- or shock-load is used in this dynamic simulation, and is characterised by the following half-sine function [21]:

$$\ddot{z}_0 = \begin{cases} A \sin\left(\frac{\pi t}{t_s}\right) & \text{if } 0 \leq t \leq t_s \\ 0 & \text{if } t > t_s \end{cases} \quad (6-29)$$

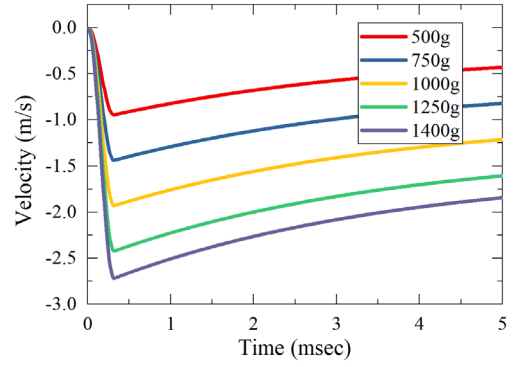
where  $t_s$  is the shock duration, set as 0.32 ms as in the referenced study. The peak force of the half-sine shock load signal is denoted as  $A$ . For a fixed shock duration, the larger the peak force, the larger the shock load. Since the purpose of this simulation is to compare the impact performance of the rotary and linear MR damper systems, stroking-out in either seat suspension system should be avoided for a useful comparison. As such, the largest peak force is set as 1400 g, so that the impact can be dissipated by both MR dampers within the stroke range. In the simulation, for both RMRSS and LMRSS, the magnetic flux density of the dampers is set as 0.6 T.

The dynamic time response of the seat suspensions under impacts ranging from 500 to 1400 g was simulated using MATLAB SIMULINK (ver. R2016b), with the results provided in **Figure 6.5**. To explain the results, we may focus first on the general trends observed for RMRSS, regardless of impact acceleration. As shown in **Figure 6.5(a)**, after applied with an upward impact on the floor at time  $t = 0$ , the seat suspension is compressed. The magnitude of the relative velocity of the top and base plates  $V_{plates}$  increases to the maximum at 0.32 ms, at which time the impact load is fully applied. Because the vertical damping force  $F_R$  is dependent on  $V_{plates}$ , it follows a similar trend, as indicated in **Figure 6.5(c)**. In addition, as the acceleration of the seat is mainly determined by the damping force, it also demonstrates such behaviour, as shown in **Figure 6.5(e)**. After 0.32 ms, floor acceleration subsides and  $V_{plates}$  gradually decreases to zero, so the damping force and the seat acceleration also decreases. Therefore, at the time of 0.32 ms, the relative velocity between the two plates, vertical damping force and the acceleration of the seat reach their peak magnitudes. As indicated in **Figure 6.5(g)**, the peak value of the acceleration of the occupant consequently appears around 15 ms, after which it settles down at about 350 ms when the energy of the system is mostly dissipated.

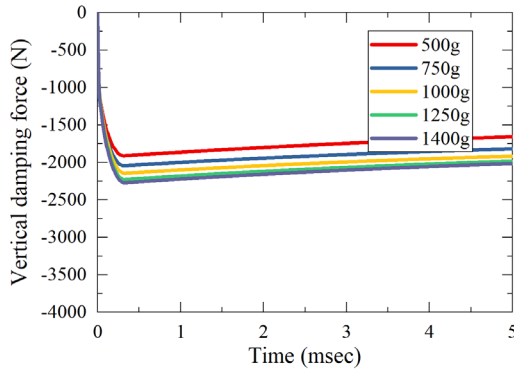
To compare the two seat suspensions, it is important to focus on the acceleration of the occupant, as this is the major consideration for the evaluation of the impact protection performance of seat suspension systems. This is given a large acceleration experienced by the occupant means they will suffer a large force during the impact, and they are more possibly to be injured. As it is shown in **Figure 6.5**, for both RMRSS and



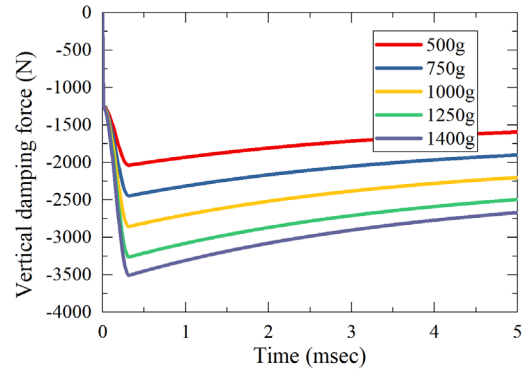
(a) Relative velocity  $V_{plates} = \dot{z}_1 - \dot{z}_0$  (RMRSS)



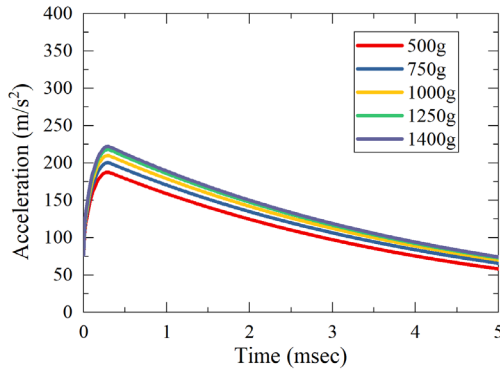
(b) Relative velocity  $V_{plates} = \dot{z}_1 - \dot{z}_0$  (LMRSS)



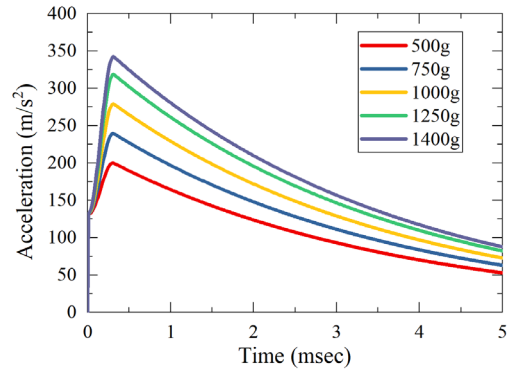
(c) Vertical damping force FR (RMRSS)



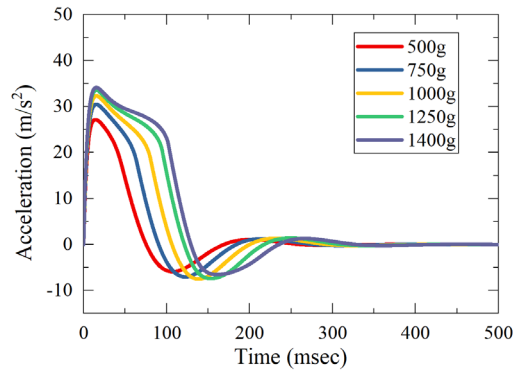
(d) Vertical damping force FL (LMRSS)



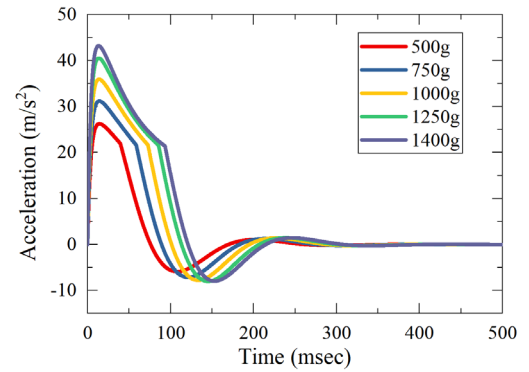
(e) Seat acceleration  $\ddot{z}_1$  (RMRSS)



(f) Seat acceleration  $\ddot{z}_1$  (LMRSS)



(g) Occupant acceleration  $\ddot{z}_2$  (RMRSS)



(h) Occupant acceleration  $\ddot{z}_2$  (LMRSS)

Figure 6.5. Simulated time response of the seat suspension systems under impact loads

LMRSS, the peak magnitudes for all the parameters: relative velocity, vertical damping force, seat acceleration, and occupant acceleration increase with the increases of the peak impact load from 500 to 1400 g. Under the same peak load condition, the peak values of the relative velocity for RMRSS and LMRSS are identical, making other measured parameters suitable for comparison. With the increase of the peak impact loads over the 500 to 1400 g range, the vertical damping force of LMRSS  $F_L$  experiences an increase of 1469.92 N from 2036.97 to 3506.89 N (**Figure 6.5(d)**), while the vertical damping force of RMRSS  $F_R$  only increased 360.67 N from 1910.26 to 2270.93 N (**Figure 6.5(c)**). As a result, the seat acceleration of LMRSS, increased 70% from 200.00 to 342.59 m/s<sup>2</sup> (**Figure 6.5(f)**), but in contrast, the seat acceleration for RMRSS only has a minor increase of 18.38% from 187.75 to 222.25 m/s<sup>2</sup> (**Figure 6.5(e)**). Regarding occupant accelerations, for the peak shock load of 500 g, the peak occupant accelerations for LMRSS is 26.23 m/s<sup>2</sup>, which is slightly smaller than that of RMRSS at 27.18 m/s<sup>2</sup>. This is consistent with the similar total output force at low plate velocities for both seat suspensions, as can be observed for the 0.6 T cases of **Figure 6.3**. However, as the peak impact load increases from 500 to 1400 g, the peak occupant acceleration for LMRSS increases by 64.37% from 26.23 to 43.22 m/s<sup>2</sup> (**Figure 6.5(h)**), while the peak occupant acceleration for RMRSS only has a minor increase of 25.68% from 27.18 to 34.16 m/s<sup>2</sup> (**Figure 6.5(g)**).

To demonstrate the velocity dependency of RMRSS and LMRSS, the relationships of the peak values of the damping force, seat acceleration, and occupant acceleration with the peak relative plates velocity are plotted in **Figure 6.6**. For LMRSS, the values of the peak damping force and peak seat acceleration are not only more sensitive to peak relative velocity but are also larger than that of RMRSS in all cases, regardless of impact velocity. And while the peak occupant acceleration of LMRSS is similarly more sensitive to velocity and generally larger than that of RMRSS, at peak relative velocities with a magnitude of less than 1.39 m/s, those of RMRSS are slightly larger than those of LMRSS. It should be made clear though, this is not a major issue for RMRSS, given this behaviour occurs at low impact loads where the hazard to the occupant is quite low. From this analysis, it can then be concluded that, not only is LMRSS more velocity-sensitive than RMRSS, the effect on the occupant is also very apparent, as the peak acceleration they experience is much larger for high-velocity impact loads, which is harmful to both the structure and the occupant.

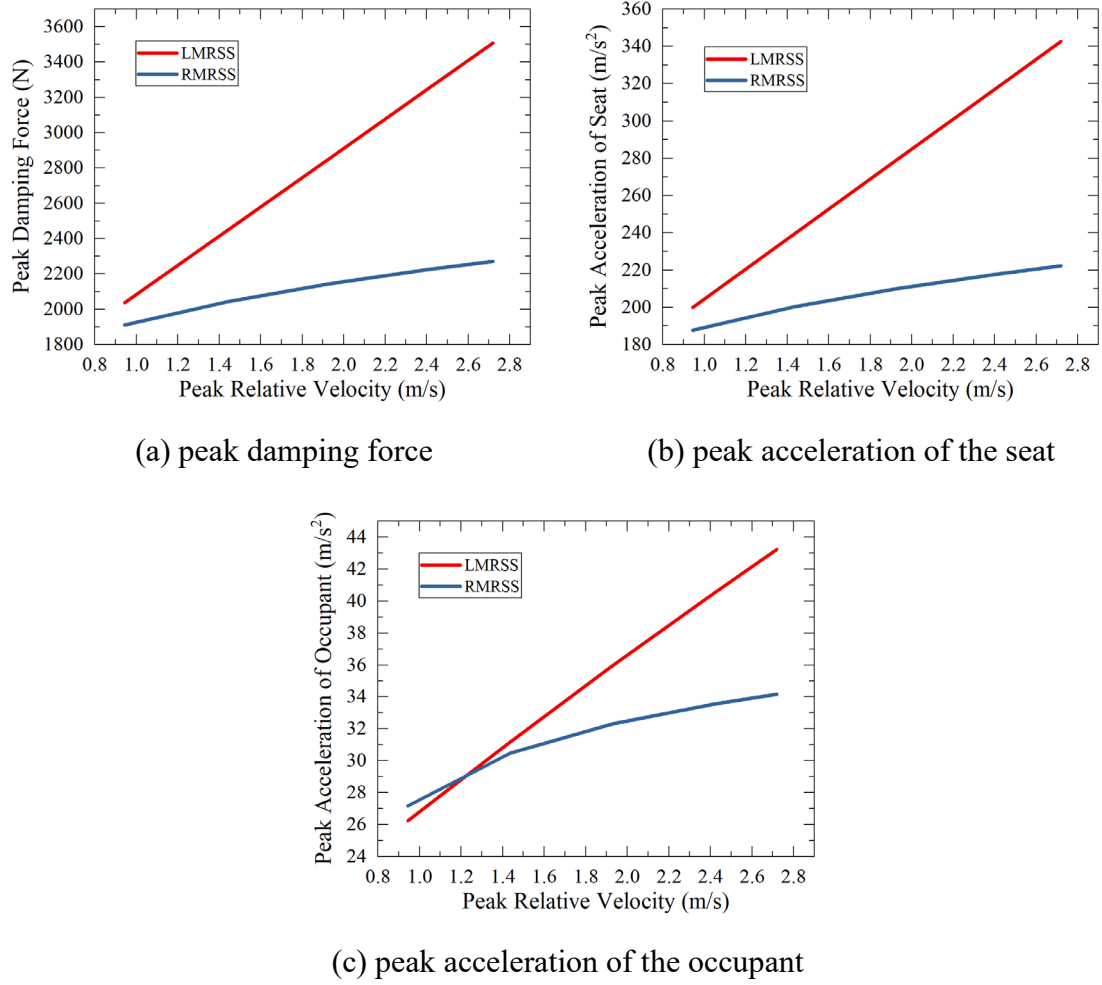


Figure 6.6. Velocity dependency analysis

## 6.5 Experimental evaluation of the RMRSS

Following the numerical evaluation of the RMRSS, an RMRSS is built. Its dynamic characteristics and impact protection performance are evaluated through experimentation in this section. The experimental setup for the characterisation of the RMRSS is illustrated in **Figure 6.7**. The RMRSS is fixed on the lower clamp of a computer-controlled MTS Landmark hydraulic test system (Load Frame Model: 370.02, MTS System Crop.). Driven by a servo-hydraulic system, the upper clamp can move in the vertical direction in accordance with the preprogrammed sequence from the control computer. At the same time, the self-contained linear displacement sensor and the load cell which are mounted to the platform of MTS, are used for logging the measured displacement and force signals to the computer. A DC power supply (GW INSTEK GPC-3030D) is used to provide current at different levels to the rotary MR damper to control the constant level of magnetic flux experienced by the contained MR fluid.



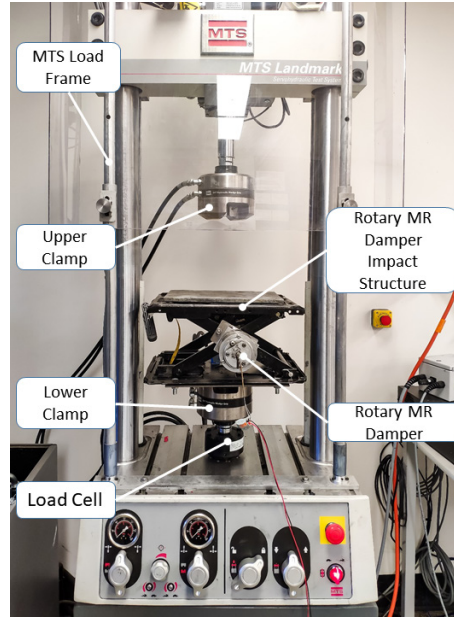


Figure 6. 7. MTS test system for RMRSS.

#### 6.5.1 Dynamic property characterization of the RMRSS

In order to test the damping variation of RMRSS, a harmonic displacement signal with an amplitude of 25 mm and 1 Hz frequency was loaded. The force-displacement responses under different constant currents resulting from these tests are plotted in **Figure 6.8(a)**. **Figure 6.8(b)** shows the corresponding equivalent damping coefficient, which is calculated using the following equation [125]:

$$C_{t,eq} = \frac{EDC}{2\pi^2 f A^2} \quad (6-30)$$

where  $C_{t,eq}$  is the equivalent damping coefficient, EDC is the energy dissipated per cycle, being the enclosed area of each force-displacement loop,  $f$  is the sinusoidal frequency, and  $A$  is the sinusoidal amplitude.

As indicated in **Figure 6.8(a)**, the area of the enclosed force-displacement loop, EDC, increases with the increase of the supplied current from -2.5 to 2.5 A, facilitated by the hybrid magnetic-field rotary MR damper. The equivalent damping coefficient in **Figure 6.8(b)** increases by 3.46 times from 548.25 to 1898.19 N s m<sup>-1</sup> as a result of this. When the current increases from 2.0 to 2.5 A or decreases from -2.0 to -2.5 A, both the force-displacement loops and consequently the equivalent damping coefficient only change slightly, indicating that magnetic saturation of the damper occurs when a large magnitude of current is applied, indicating the functional limits of the device have been reached.

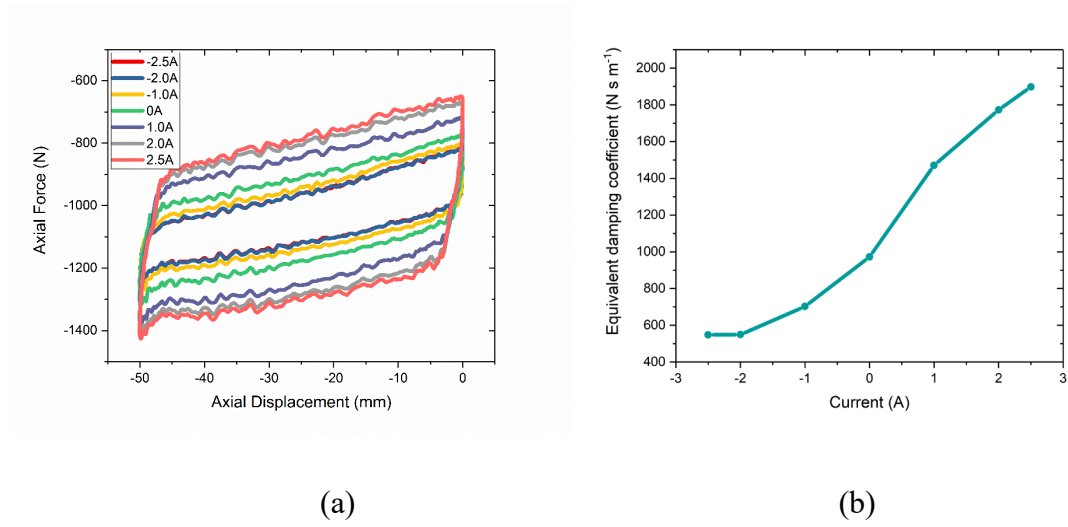


Figure 6. 8. (a) Force–displacement loops and (b) equivalent damping coefficient of the RMRSS under different currents.

#### 6.5.2 Impact test of the RMRSS

Following the characterization tests of the RMRSS, impact tests under different constant velocities were conducted. The testing procedure was set as follows: firstly, the RMRSS is pre-compressed by the upper clamp of the MTS to make sure it touches the top plate of RMRSS; then, the upper clamp moves down by -50 mm at the constant velocity of 0.05, 0.1, and 0.2 m/s, in three separate cases; for each tests, damper current is set to a range of values from -2.5 to 2.5 A. The test results of a constant velocity of 0.05 m/s including the force-displacement relationship and the generated forces are plotted in **Figures 6.9(a) and (b)**.

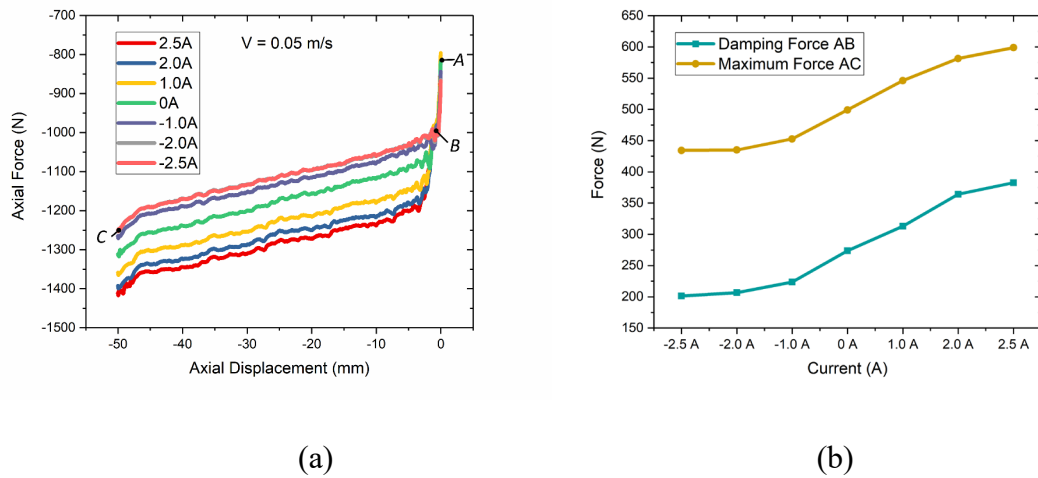


Figure 6. 9. (a) Force–displacement response to impact at a constant velocity  $V = 0.05 \text{ m/s}$  and (b) generated forces of the RMRSS under varied currents.

As shown in **Figures 6.9(a)**, the impact process, from indicated points A to B and then C, can be separated into two distinct sections: AB and BC. At the initial state, point A, the structure is pre-compressed by the upper clamp. The force reading at point A comprises of both the weight of the structure and a small pre-compress force of the spring. The process of the upper clamp moving down to the axial displacement -50 mm is represented by the sections AB and BC. A large initial damping force is generated through AB to overcome the yield torque of the rotary MR damper in order to achieve relative rotation between the rotor and cylinder of the damper, to allow the top plate to move down. The spring on the seat structure is compressed during the whole period of AC, although the main cause for change in force during BC is due to the spring, given the damper is operating purely in the post-yield state at this time. Therefore, the force-displacement ratio of section BC can be regarded as a close approximation of the structure's stiffness. **Figures 6.9(b)** then illustrates the damping force and maximum force that are separately calculated from the force differences of sections AB and AC in **Figures 6.9(a)**. The damping force shows an increase of 1.9 times from 201.38 to 382.76 N as the current increased from -2.5 to 2.5 A. The maximum force AC increases in a similar proportion from 434.34 to 598.96 N.

The force-displacement response at the constant velocities  $V = 0.1$  m/s and  $V = 0.2$  m/s are plotted in **Figure 6.10(a) and (b)**, respectively. It can be seen that the force-displacement response of these two velocities is similar to that of  $V = 0.05$  m/s in **Figure 6.9(a)**. Both the damping force and the maximum force of the structure have similar tendencies to increase with applied current. The force-displacement responses with currents -2.5 and 2.5 A for the three tested impact velocities of 0.05, 0.1, and 0.2 m/s are then compared in **Figure 6.10(c)**. It is observed that under the same current condition, the impact performances for the three velocities are identical. Although, as the velocity increases from 0.05 to 0.2 m/s, the force fluctuates more during the impact process. A force peak is generated when the axial displacement is near -2 mm at the largest velocity  $V = 0.2$  m/s when -2.5 A current is applied, while no apparent force peak is found under the lowest impact velocity  $V = 0.05$  m/s. This is likely due to the inertial torque to accelerate the rotor of the damper, which is much larger for the  $V = 0.2$  m/s case.

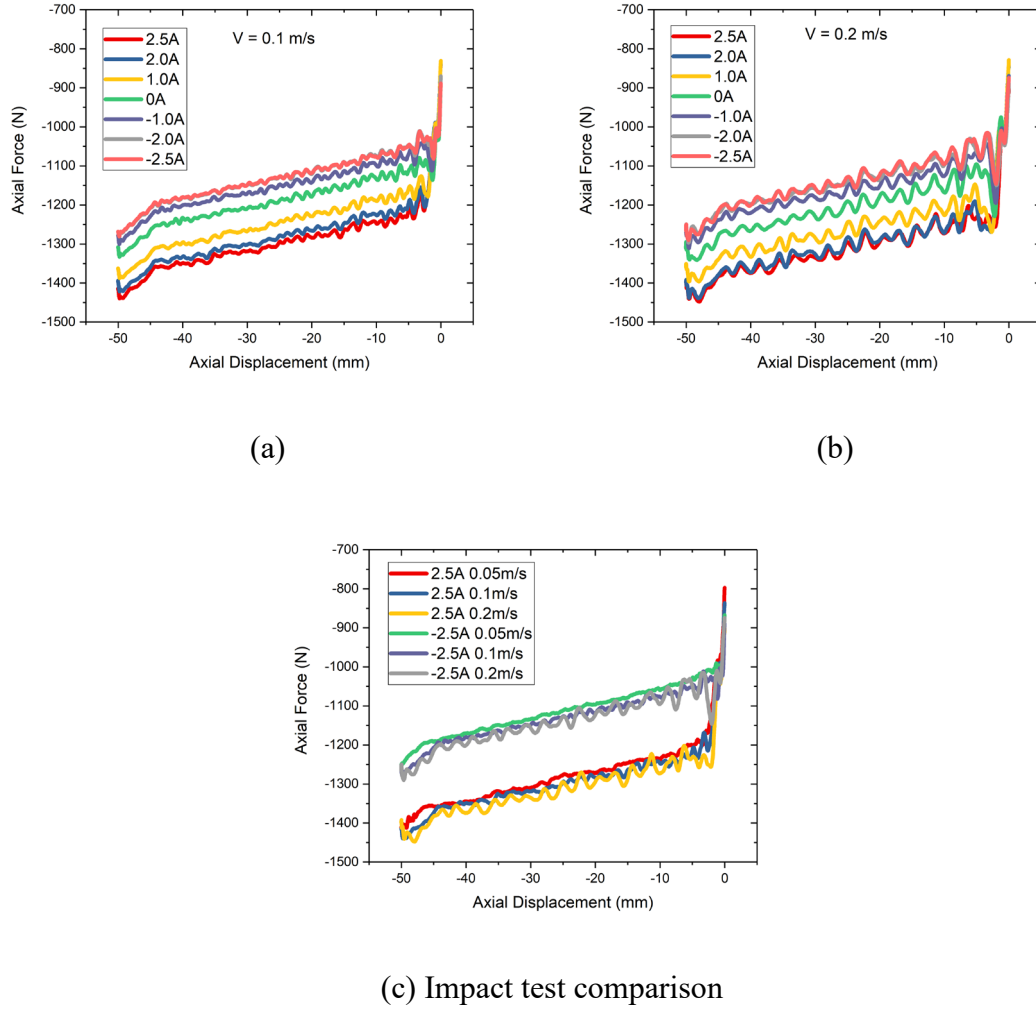


Figure 6. 10. Force-displacement response at velocities of 0.1 m/s (a) and 0.2 m/s (b); (c) force-displacement response at 2.5 and -2.5 A for impact velocities: 0.05, 0.1, and 0.2 m/s.

As the maximum constant velocity of the MTS Landmark hydraulic testing system used in this study is 0.2 m/s, only low-velocity impact tests could be conducted, however, high-velocity impact tests will be conducted in the future by building new equipment. Although the impact tests included here were performed at quite low impact-velocities, the results support the hypothesis and modelling comparisons of the RMRSS and the LRMRSS. Namely, it has been demonstrated that the RMRSS does not appear to be very sensitive to the impact velocity and can provide a similar damping force variation range under different impact velocities, satisfying the key requirement of impact protection.

## 6.6 Conclusion

This chapter investigated the impact protection performance of the RMRSS

theoretically and experimentally in order to avoid the velocity-sensitive limitation of the LMRSS. The transient mathematical modelling and dynamic impact simulations demonstrated that the RMRSS has much smaller velocity-sensitivity and a hence better impact protection performance than that of the LMRSS, achieving lower peak occupant acceleration. In addition, experimental characterisation and impact testing of a prototype RMRSS validated that the RMRSS has a low sensitivity to the impact velocity, which verifies that the RMRSS can provide better impact performance for seat occupants, at least for the low-range impact velocities tested, with high-velocity impacts to be tested in the future.

## Chapter 7

### Conclusion and future work

#### 7.1 Conclusions

##### 7.1.1 Developing a rotary VSVD MR damper

This thesis successfully expanded the idea of variable damping and stiffness from linear MR dampers to rotary MR dampers. A rotary VSVD damper was designed, prototyped and experimentally verified. The experimental results indicated that the proposed damper is able to simultaneously change its damping and stiffness via two control currents. Its damping increased 141.6% from 13.98 to 33.78 N.m.s.rad<sup>-1</sup> as the applied damping current increased from 0 to 1 A. Meanwhile, the effective stiffness had a 618.1% increase from 31.51 to 226.26 N.m.rad<sup>-1</sup> with the stiffness current increased from 0 to 2 A. A mathematical model was also built with its parameters identified, and it was proved to describe the behaviour of the rotary VSVD damper very well. The success of designing and prototyping a VSVD rotary damp built a solid foundation for the idea of variable damping and stiffness applying to angular rotational scenarios on vibration control, position control and other possible applications.

##### 7.1.2 Positioning control of a robotic arm

A positioning control system for a robotic arm based on a rotary damping and stiffness MR damper was researched in this thesis to solve the overshoot and vibration during the positioning process. A rotary VSVD MR damper had been modified with larger damping variation and smaller stiffness for the robotic arm's positioning system. Two excitations of a step function signal and a harmonic function signal were designed for the evaluation of the proposed positioning system. Mathematical simulation using Matlab/Simulink and experimental tests were conducted to evaluate the performance of the proposed positioning control system. Both the simulation and experiment results indicated that the positioning control performances had been significantly improved by VSVD control with smaller overshoot, less settling time and less power consumption.

##### 7.1.3 Vibration control of a seat suspension

Vibration control aiming at reducing seat suspension's vibration and protecting drivers' health using rotary VSVD dampers based seat suspension was investigated. Rotary VSVD dampers that can be installed on the intersection of the suspension's

scissor structure was designed and prototyped. The property tests of the proposed seat suspension using MTS verified that the equivalent damping of the proposed suspension has a 3-times increase with the increase of damping current from 0 to 2 A, and the effective stiffness increased 5.34 times with the corresponding increase of stiffness current. Three kinds of excitation: harmonic signal, bump signal and random signal were chosen as the excitations for the vibration control performance evaluation. Mathematica simulation using Matlab/Simulink with the three excitations was conducted. Besides, the assembled VSVD seat suspension was also tested on the six-DOF vibration platform under these excitations. Both the numerical simulation and the experimental test proved that VSVD case works better than passive on case, pure damping control case and pure stiffness control case. The vibration control performance of the seat was largely improved by the proposed VSVD seat suspension.

#### 7.1.4 Impact protection of seat suspensions

Apart from vibrations, a driver may also suffer dangers caused by impacts such as mine-blast cause impact for military vehicles, hash- or crash- landing for helicopters. Such kinds of impacts can result in severe diseases like spinal fractures or even death. Through the analysis, the linear MR damper based seat suspension (LMRSS) has a strong velocity-dependent behaviour, namely, the damping force can increase rapidly due to the increase of impact velocity. Because of the structural difference, the rotary damper with a less velocity-dependency can be a good candidate for the design of seat suspension. Hence, the impact protection performance of a rotary MR damper based suspension (RMRSS) was studied. The transient mathematical analysis and dynamic impact simulation demonstrated that RMRSS has a smaller velocity-sensitivity and a better impact protection performance than LRMSS. The experimental characterisation and impact tests also proved the low velocity sensitivity of RMRSS, indicating good impact protection of RMRSS

## 7.2 Future work

### 7.2.1 Developing MR dampers with a large damping range

During the research of developing a rotary VSVD MR damper, it is found that the damping force will increase further if the applied current is larger than only 1 A. The damping variation change only has 1.5 times from 13.98 to 33.78 N.m.s.rad<sup>-1</sup>, which is worse than a mature MR damper. One reason is magnetic field saturation which means the generated magnetic flux density will not increase further with the larger current

because the material does not allow more magnetic flux to pass through. Another reason for the small damping variation is that the working areas of the internal MR damper unit are very limited. Hence, the design of the internal MR damper must be optimized. Firstly, the dimension parameters of the shaft, rotator and casing should be optimized to avoid the magnetic field saturation phenomenon. Then, the working areas of the MRF should be expanded to enlarge the damping force output. The enlarged working areas can also increase the damping variation change ratio because it weakens the magnetic saturation phenomenon.

#### 7.2.2 Energy saving study on the robotic arm manoeuvre

In terms of the research on positioning control of the robotic arm, the overshoot and vibration during the settling time were reduced by the rotary VSVD damper. The stiffness unit, a spring, can provide additional torque apart from the damping unit and can be used for acceleration. However, the spring unit's contribution to saving energy during the movement from one point to another has not been investigated. Specifically, acceleration and deceleration are the two process of a robotic arm moving back and forth from one point to another. Theoretically, the energy can be saved to the spring during the deceleration process and release in the acceleration process so as to saving energy. This may be a good topic for the following research in the future. One challenge for this idea may be the control of spring, namely, how to hold the spring after storage energy (being stretched) in the deceleration process and release the spring for letting the energy to help in the acceleration process.

#### 7.2.3 Developing an MR damper based semi-active seat suspension with non-linear stiffness

A VSVD seat suspension that can reduce the vibration and protect the driver was researched in this thesis. For the stiffness control, the seat suspension's stiffness is provided by a spring with small stiffness on the seat suspension and the spring of the VSVD damper with a large spring. The suspension remains a small stiffness in small vibration amplitude to achieve small transmissibility. In the large vibration amplitude, the suspension's stiffness will be increased because the VSVD damper will provide additional stiffness when the control current applied so as to avoid end-stop impacts caused by stroke used out. However, for stiffness's semi-active control, the suspension's stiffness will always be small once the controller fails. In this case, end-stop impacts may occur and endanger the driver. Considering this fail-safety issue of the proposed



VSVD seat suspension, an MR damper with a passive non-linear stiffness structure can be a good candidate for the vibration control of seat suspension with better fail-safety. Hence, this may be an interesting topic for research in the future.

#### 7.2.4 Application of rotary VSVD MR dampers on the impact protection application

The thesis presented a study of the impact protection performance of a rotary MR damper based seat suspension. It is proved that rotary MR dampers is a better choice than linear MR dampers for the seat suspension regarding on the high-velocity impact. In the research, the damping control strategy to achieve maximum energy dissipation and the smallest acceleration of occupant has not been discussed. In addition, stiffness variability may also be a help in impact protection. Hence, it may be a good idea to introduce VSVD dampers that can optimally vary damping and stiffness at the same time in the impact process to improve protection performance, which requires further investigations in the future.

## References

- [1] R. Ahamed, S.-B. Choi, M.M. Ferdous, A state of art on magneto-rheological materials and their potential applications, *Journal of Intelligent Material Systems and Structures*, 29 (2018) 2051-2095.
- [2] S. Sun, X. Tang, J. Yang, D. Ning, H. Du, S. Zhang, W. Li, A new generation of magnetorheological vehicle suspension system with tunable stiffness and damping characteristics, *IEEE Transactions on Industrial Informatics*, 15 (2019) 4696-4708.
- [3] S.-B. Choi, Y.-M. Han, *Magnetorheological fluid technology: applications in vehicle systems*, CRC press 2012.
- [4] X.-X. Bai, W. Hu, N.M. Wereley, Magnetorheological damper utilizing an inner bypass for ground vehicle suspensions, *IEEE Transactions on Magnetics*, 49 (2013) 3422-3425.
- [5] H.-J. Jung, B. Spencer Jr, Y. Ni, I. Lee, State-of-the-art of semiactive control systems using MR fluid dampers in civil engineering applications, *Structural Engineering and Mechanics*, 17 (2004) 493-526.
- [6] T. Nguyen, N. Kwok, Q. Ha, J. Li, B. Samali, Adaptive sliding mode control for civil structures using magnetorheological dampers, 2006 *Proceedings of the 23rd International Symposium on Robotics and Automation in Construction, ISARC 2006*, 2006.
- [7] S. Laflamme, J.J. Connor, Application of self-tuning Gaussian networks for control of civil structures equipped with magnetorheological dampers, *Active and Passive Smart Structures and Integrated Systems 2009*, International Society for Optics and Photonics, 2009, pp. 72880M.
- [8] J.-S. Oh, S.-B. Choi, State of the art of medical devices featuring smart electro-rheological and magneto-rheological fluids, *Journal of King Saud University-Science*, 29 (2017) 390-400.
- [9] F. Gao, Y.-N. Liu, W.-H. Liao, Optimal design of a magnetorheological damper used in smart prosthetic knees, *Smart Materials and Structures*, 26 (2017) 035034.
- [10] Q. Fu, D.-H. Wang, L. Xu, G. Yuan, A magnetorheological damper-based prosthetic knee (MRPK) and sliding mode tracking control method for an MRPK-based lower limb prosthesis, *Smart Materials and Structures*, 26 (2017) 045030.
- [11] C. Han, B.-H. Kang, S.-B. Choi, J.M. Tak, J.-H. Hwang, Control of landing efficiency of an aircraft landing gear system with magnetorheological dampers, *Journal of Aircraft*, 56 (2019) 1980-1986.
- [12] Y.-T. Choi, R. Robinson, W. Hu, N.M. Wereley, T.S. Birchette, A.O. Bolukbasi, J. Woodhouse, Analysis and control of a magnetorheological landing gear system for a helicopter, *Journal of the American Helicopter Society*, 61 (2016) 1-8.
- [13] M. Mao, W. Hu, Y.-T. Choi, N.M. Wereley, A magnetorheological damper with bifold valves for shock and vibration mitigation, *Journal of Intelligent Material Systems and Structures*, 18 (2007) 1227-1232.
- [14] S. Sun, J. Yang, W. Li, H. Du, G. Alici, T. Yan, M. Nakano, Development of an isolator working with magnetorheological elastomers and fluids, *Mechanical Systems and Signal Processing*, 83 (2017) 371-384.
- [15] S. Sun, J. Yang, W. Li, H. Deng, H. Du, G. Alici, Development of a novel variable stiffness and damping magnetorheological fluid damper, *Smart Materials and Structures*, 24 (2015) 085021.
- [16] H. Huang, S. Sun, S. Chen, W. Li, Numerical and experimental studies on a new variable stiffness and damping magnetorheological fluid damper, *Journal of Intelligent Material Systems and Structures*, 30 (2019) 1639-1652.

- [17] S. Sun, X. Tang, W. Li, H. Du, Advanced vehicle suspension with variable stiffness and damping MR damper, 2017 IEEE International Conference on Mechatronics (ICM), IEEE, 2017, pp. 444-448.
- [18] S. Sun, D. Ning, J. Yang, H. Du, S. Zhang, W. Li, A seat suspension with a rotary magnetorheological damper for heavy duty vehicles, Smart Materials and Structures, 25 (2016) 105032.
- [19] G.J. Hiemenz, W. Hu, N.M. Wereley, Semi-active magnetorheological helicopter crew seat suspension for vibration isolation, Journal of Aircraft, 45 (2008) 945-953.
- [20] Y.-T. Choi, N.M. Wereley, Biodynamic response mitigation to shock loads using magnetorheological helicopter crew seat suspensions, Journal of aircraft, 42 (2005) 1288-1295.
- [21] Y.T. Choi, N.M. Wereley, Mitigation of biodynamic response to vibratory and blast-induced shock loads using magnetorheological seat suspensions, Proceedings of the Institution of Mechanical Engineers, Part D: Journal of Automobile Engineering, 219 (2005) 741-753.
- [22] R. Ahamed, S.-B. Choi, M.M. Ferdous, A state of art on magneto-rheological materials and their potential applications, J Intel Mat Syst Str, DOI (2018) 1045389X18754350.
- [23] J.D. Carlson, M.R. Jolly, MR fluid, foam and elastomer devices, Mechatronics, 10 (2000) 555-569.
- [24] J. De Vicente, D.J. Klingenberg, R. Hidalgo-Alvarez, Magnetorheological fluids: a review, Soft matter, 7 (2011) 3701-3710.
- [25] M. Kciuk, R. Turczyn, Properties and application of magnetorheological fluids, Journal of Achievements in Materials and Manufacturing Engineering, 18 (2006) 127-130.
- [26] Y. Li, J. Li, W. Li, H. Du, A state-of-the-art review on magnetorheological elastomer devices, Smart materials and structures, 23 (2014) 123001.
- [27] J. Yang, S. Sun, S. Zhang, W. Li, Review of structural control technologies using magnetorheological elastomers, Current Smart Materials, 4 (2019) 22-28.
- [28] B.M. Kavlicoglu, F. Gordaninejad, X. Wang, Study of a magnetorheological grease clutch, Smart Materials and Structures, 22 (2013) 125030.
- [29] N. Mohamad, S. Mazlan, S.-B. Choi, M. Nordin, The field-dependent rheological properties of magnetorheological grease based on carbonyl-iron-particles, Smart Materials and Structures, 25 (2016) 095043.
- [30] T. Mitsumata, Recent progress in magnetorheological gels and elastomers, Recent Patents on Chemical Engineering, 2 (2009) 159-166.
- [31] B. Wei, X. Gong, W. Jiang, L. Qin, Y. Fan, Study on the properties of magnetorheological gel based on polyurethane, Journal of applied polymer science, 118 (2010) 2765-2771.
- [32] A.K. Bastola, M. Hossain, A review on magneto-mechanical characterizations of magnetorheological elastomers, Composites Part B: Engineering, DOI (2020) 108348.
- [33] S. Xuan, Y. Xu, T. Liu, X. Gong, Recent progress on the magnetorheological elastomers, International Journal of Smart and Nano Materials, 6 (2015) 135-148.
- [34] G. Bossis, S. Lacis, A. Meunier, O. Volkova, Magnetorheological fluids, Journal of magnetism and magnetic materials, 252 (2002) 224-228.
- [35] A.-G. Olabi, A. Grunwald, Design and application of magneto-rheological fluid, Materials & design, 28 (2007) 2658-2664.
- [36] M. Ashtiani, S. Hashemabadi, A. Ghaffari, A review on the magnetorheological fluid preparation and stabilization, Journal of magnetism and Magnetic Materials, 374 (2015) 716-730.

- [37] J.N. Ghogh, Application of smart technologies in drilling fluids, Petroleum University of Technology, 2016.
- [38] D. Truong, K. Ahn, MR fluid damper and its application to force sensorless damping control system, Smart Actuation and Sensing Systems-Recent Advances and Future Challenges, InTech, Rijeka, DOI (2012) 383-424.
- [39] W. Jiang, Y. Zhang, S. Xuan, C. Guo, X. Gong, Dimorphic magnetorheological fluid with improved rheological properties, Journal of Magnetism and Magnetic Materials, 323 (2011) 3246-3250.
- [40] M. Brigley, Y.-T. Choi, N.M. Wereley, S.-B. Choi, Magnetorheological isolators using multiple fluid modes, J Intel Mat Syst Str, 18 (2007) 1143-1148.
- [41] S.-B. Choi, S.-R. Hong, K.-G. Sung, J.-W. Sohn, Optimal control of structural vibrations using a mixed-mode magnetorheological fluid mount, International Journal of Mechanical Sciences, 50 (2008) 559-568.
- [42] S.-R. Hong, S. John, N.M. Wereley, Y.-T. Choi, S.-B. Choi, A unifying perspective on the quasi-steady analysis of magnetorheological dampers, J Intel Mat Syst Str, 19 (2008) 959-976.
- [43] X.-m. Dong, M. Yu, C.-r. Liao, W.-m. Chen, Comparative research on semi-active control strategies for magneto-rheological suspension, Nonlinear dynamics, 59 (2010) 433-453.
- [44] R. Jeyasenthil, S.-B. Choi, Response time effect of magnetorheological dampers in a semi-active vehicle suspension system: performance assessment with quantitative feedback theory, Smart Materials and Structures, 28 (2019) 054001.
- [45] X. Du, M. Yu, J. Fu, C. Huang, Experimental study on shock control of a vehicle semi-active suspension with magneto-rheological damper, Smart Materials and Structures, 29 (2020) 074002.
- [46] L.A.A. Powell, Y.T. Choi, W. Hu, N.M. Wereley, Nonlinear modeling of adaptive magnetorheological landing gear dampers under impact conditions, Smart Materials and Structures, 25 (2016) 115011.
- [47] B.-H. Kang, J.-Y. Yoon, G.-W. Kim, S.-B. Choi, Landing efficiency control of a six-degree-of-freedom aircraft model with magnetorheological dampers: Part 1—Modeling, Journal of Intelligent Material Systems and Structures, DOI (2020) 1045389X20942578.
- [48] D. Cruze, G. Hemalatha, S.V.S. Jebadurai, L. Sarala, D. Tensing, S.J.E. Christy, A review on the magnetorheological fluid, damper and its applications for seismic mitigation, Civil Engineering Journal, 4 (2018) 3058-3074.
- [49] M. Christie, S. Sun, L. Deng, D. Ning, H. Du, S. Zhang, W. Li, A variable resonance magnetorheological-fluid-based pendulum tuned mass damper for seismic vibration suppression, Mechanical Systems and Signal Processing, 116 (2019) 530-544.
- [50] B. Ebrahimi, Development of hybrid electromagnetic dampers for vehicle suspension systems, DOI (2009).
- [51] E. Nima, Development of a semi-active intelligent suspension system for heavy vehicles, DOI (2008).
- [52] J.A. Norris, M. Ahmadian, Behavior of magneto-rheological fluids subject to impact and shock loading, ASME 2003 International Mechanical Engineering Congress and Exposition, American Society of Mechanical Engineers, 2003, pp. 199-204.
- [53] G. Yang, B. Spencer Jr, J. Carlson, M. Sain, Large-scale MR fluid dampers: modeling and dynamic performance considerations, Engineering structures, 24 (2002) 309-323.
- [54] D. Wang, H. Ai, W. Liao, A magnetorheological valve with both annular and radial fluid flow resistance gaps, Smart materials and structures, 18 (2009) 115001.

- [55] D. Lee, Y. Nam, R. Yamane, M. Park, Performance evaluation on vibration control of MR landing gear, *Journal of Physics: Conference Series*, IOP Publishing, 2009, pp. 012068.
- [56] M.T. Avraam, MR-fluid brake design and its application to a portable muscular rehabilitation device, *Doktora Tezi*, Université Libre De Bruxelles, Faculté De Sciences Appliquées, DOI (2009).
- [57] A. Farjoud, N. Vahdati, Y.F. Fah, MR-fluid yield surface determination in disc-type MR rotary brakes, *Smart Materials and Structures*, 17 (2008) 035021.
- [58] J. Huang, J. Zhang, Y. Yang, Y. Wei, Analysis and design of a cylindrical magneto-rheological fluid brake, *Journal of Materials Processing Technology*, 129 (2002) 559-562.
- [59] D. Senkal, H. Gurocak, Compact MR-brake with serpentine flux path for haptics applications, *EuroHaptics conference*, 2009 and *Symposium on Haptic Interfaces for Virtual Environment and Teleoperator Systems*. World Haptics 2009. Third Joint, IEEE, 2009, pp. 91-96.
- [60] T. Kikuchi, K. Kobayashi, Design and development of cylindrical MR fluid brake with multi-coil structure, *Journal of System Design and Dynamics*, 5 (2011) 1471-1484.
- [61] W. Li, H. Du, Design and experimental evaluation of a magnetorheological brake, *The International Journal of Advanced Manufacturing Technology*, 21 (2003) 508-515.
- [62] E.J. Park, D. Stoikov, L.F. da Luz, A. Suleman, A performance evaluation of an automotive magnetorheological brake design with a sliding mode controller, *Mechatronics*, 16 (2006) 405-416.
- [63] W. Zhou, C.-M. Chew, G.-S. Hong, Development of a compact double-disk magneto-rheological fluid brake, *Robotica*, 25 (2007) 493-500.
- [64] S. Mazlan, A. Issa, H. Chowdhury, A. Olabi, Magnetic circuit design for the squeeze mode experiments on magnetorheological fluids, *Materials & Design*, 30 (2009) 1985-1993.
- [65] Y.-J. Nam, Y.-J. Moon, M.-K. Park, Performance improvement of a rotary MR fluid actuator based on electromagnetic design, *J Intel Mat Syst Str*, 19 (2008) 695-705.
- [66] P.-B. Nguyen, S.-B. Choi, A new approach to magnetic circuit analysis and its application to the optimal design of a bi-directional magnetorheological brake, *Smart Materials and Structures*, 20 (2011) 125003.
- [67] Q.H. Nguyen, J.C. Jeon, S.B. Choi, Optimal design of an hybrid magnetorheological brake for middle-sized motorcycles, *Applied Mechanics and Materials*, Trans Tech Publ, 2011, pp. 371-377.
- [68] Q. Nguyen, S. Choi, Selection of magnetorheological brake types via optimal design considering maximum torque and constrained volume, *Smart Materials and Structures*, 21 (2011) 015012.
- [69] J. Yu, X. Dong, W. Wang, Prototype and test of a novel rotary magnetorheological damper based on helical flow, *Smart Materials and Structures*, 25 (2016) 025006.
- [70] W. Liao, C. Lai, Harmonic analysis of a magnetorheological damper for vibration control, *Smart Materials and Structures*, 11 (2002) 288.
- [71] Z. Wang, Z. Chen, H. Gao, H. Wang, Development of a self-powered magnetorheological damper system for cable vibration control, *Applied Sciences*, 8 (2018) 118.
- [72] Y. Liu, H. Matsuhisa, H. Utsuno, J.G. Park, Vibration control by a variable damping and stiffness system with magnetorheological dampers, *JSME International Journal Series C Mechanical Systems, Machine Elements and Manufacturing*, 49 (2006) 411-417.
- [73] Y. Liu, H. Matsuhisa, H. Utsuno, Semi-active vibration isolation system with

- variable stiffness and damping control, *Journal of sound and vibration*, 313 (2008) 16-28.
- [74] S. Hong, G. Wang, W. Hu, N. Wereley, Liquid spring shock absorber with controllable magnetorheological damping, *Proceedings of the Institution of Mechanical Engineers, Part D: Journal of Automobile Engineering*, 220 (2006) 1019-1029.
- [75] X. Zhu, X. Jing, L. Cheng, A magnetorheological fluid embedded pneumatic vibration isolator allowing independently adjustable stiffness and damping, *Smart Materials and Structures*, 20 (2011) 085025.
- [76] G. Liao, X. Gong, S. Xuan, C. Kang, L. Zong, Development of a real-time tunable stiffness and damping vibration isolator based on magnetorheological elastomer, *Journal of Intelligent Material Systems and Structures*, 23 (2012) 25-33.
- [77] W. Li, X. Wang, X. Zhang, Y. Zhou, Development and analysis of a variable stiffness damper using an MR bladder, *Smart materials and structures*, 18 (2009) 074007.
- [78] X. Zhang, X. Wang, W. Li, K. Kostidis, Variable stiffness and damping MR isolator, *Journal of Physics: Conference Series*, IOP Publishing, 2009, pp. 012088.
- [79] S. Sun, H. Deng, W. Li, Variable stiffness and damping suspension system for train, *Active and Passive Smart Structures and Integrated Systems 2014*, International Society for Optics and Photonics, 2014, pp. 90570P.
- [80] D. Verscheure, B. Paijmans, H. Van Brussel, J. Swevers, Vibration and motion control design and trade-off for high-performance mechatronic systems, 2006 IEEE Conference on Computer Aided Control System Design, 2006 IEEE International Conference on Control Applications, 2006 IEEE International Symposium on Intelligent Control, IEEE, 2006, pp. 1115-1120.
- [81] K. Sato, A. Shimokohbe, Characteristics of practical control for point-to-point (PTP) positioning systems: Effect of design parameters and actuator saturation on positioning performance, *Precision Engineering*, 27 (2003) 157-169.
- [82] M.F.M. Yakub, W. Martono, R. Akmeiliawati, Vibration control of two-mass rotary system using improved NCTF controller for positioning systems, 2010 IEEE Control and System Graduate Research Colloquium (ICSGRC 2010), IEEE, 2010, pp. 61-67.
- [83] T. Tang, S. Chong, C. Chan, V. Sakthivelu, Point-to-point positioning control of a pneumatic muscle actuated system using improved-PID control, 2016 IEEE International Conference on Automatic Control and Intelligent Systems (I2CACIS), IEEE, 2016, pp. 45-50.
- [84] M.R. Jolly, Pneumatic motion control using magnetorheological technology, *Smart Structures and Materials 2001: Industrial and Commercial Applications of Smart Structures Technologies*, International Society for Optics and Photonics, 2001, pp. 300-307.
- [85] P. Yadmellat, A.S. Shafer, M.R. Kermani, Design and development of a single-motor, two-DOF, safe manipulator, *IEEE/ASME Transactions on Mechatronics*, 19 (2013) 1384-1391.
- [86] B. Sapiński, M. Węgrzynowski, J. Nabielec, Magnetorheological damper-based positioning system with power generation, *Journal of Intelligent Material Systems and Structures*, 29 (2018) 1236-1254.
- [87] Z. Bai, X. Li, Z. Sun, Pneumatic servo rotary actuator with a MRF-damper, *Proceedings of 2011 International Conference on Fluid Power and Mechatronics*, IEEE, 2011, pp. 242-247.
- [88] S. Nagai, H. Tomori, Y. Midorikawa, T. Nakamura, The position and vibration control of the artificial muscle manipulator by variable viscosity coefficient using MR brake, *IECON 2011-37th Annual Conference of the IEEE Industrial Electronics*

Society, IEEE, 2011, pp. 307-312.

[89] J.J. Lima, J.M. Balthazar, R.T. Rocha, F.C. Janzen, D. Bernardini, G. Litak, D.G. Bassinello, A.M. Tusset, On Positioning and Vibration Control Application to Robotic Manipulators with a Nonideal Load Carrying, Shock and Vibration, 2019 (2019).

[90] J.J. Lima, R.T. Rocha, F.C. Janzen, A.M. Tusset, D.G. Bassinello, J.M. Balthazar, Position control of a manipulator robotic arm considering flexible joints driven by a DC motor and a controlled torque by a MR-brake, ASME International Mechanical Engineering Congress and Exposition, American Society of Mechanical Engineers, 2016, pp. V04BT05A022.

[91] H. Tomori, S. Nagai, T. Majima, T. Nakamura, Variable impedance control with an artificial muscle manipulator using instantaneous force and MR brake, 2013 IEEE/RSJ International Conference on Intelligent Robots and Systems, IEEE, 2013, pp. 5396-5403.

[92] K. Krajnak, Health effects associated with occupational exposure to hand-arm or whole body vibration, Journal of Toxicology and Environmental Health, Part B, 21 (2018) 320-334.

[93] J.L. Coyte, D. Stirling, H. Du, M. Ros, Seated whole-body vibration analysis, technologies, and modeling: a survey, IEEE Transactions on Systems, Man, and Cybernetics: Systems, 46 (2015) 725-739.

[94] A. Heidarian, X. Wang, Review on seat suspension system technology development, Applied Sciences, 9 (2019) 2834.

[95] M. Al-Ashmori, X. Wang, A Systematic Literature Review of Various Control Techniques for Active Seat Suspension Systems, Applied Sciences, 10 (2020) 1148.

[96] Y. Zhao, X. Wang, A review of low-frequency active vibration control of seat suspension systems, Applied Sciences, 9 (2019) 3326.

[97] I. Maciejewski, L. Meyer, T. Krzyzynski, Modelling and multi-criteria optimisation of passive seat suspension vibro-isolating properties, Journal of sound and Vibration, 324 (2009) 520-538.

[98] M.W. Holtz, J.L. Van Niekerk, Modelling and design of a novel air-spring for a suspension seat, Journal of sound and Vibration, 329 (2010) 4354-4366.

[99] T.D. Le, K.K. Ahn, A vibration isolation system in low frequency excitation region using negative stiffness structure for vehicle seat, Journal of Sound and Vibration, 330 (2011) 6311-6335.

[100] L. Tu, D. Ning, S. Sun, W. Li, H. Huang, M. Dong, H. Du, A novel negative stiffness magnetic spring design for vehicle seat suspension system, Mechatronics, 68 (2020) 102370.

[101] D. Ning, S. Sun, J. Zhang, H. Du, W. Li, X. Wang, An active seat suspension design for vibration control of heavy-duty vehicles, Journal of low frequency noise, vibration and active control, 35 (2016) 264-278.

[102] D. Ning, S. Sun, L. Wei, B. Zhang, H. Du, W. Li, Vibration reduction of seat suspension using observer based terminal sliding mode control with acceleration data fusion, Mechatronics, 44 (2017) 71-83.

[103] D. Ning, S. Sun, F. Zhang, H. Du, W. Li, B. Zhang, Disturbance observer based Takagi-Sugeno fuzzy control for an active seat suspension, Mechanical Systems and Signal Processing, 93 (2017) 515-530.

[104] D. Ning, S. Sun, H. Li, H. Du, W. Li, Active control of an innovative seat suspension system with acceleration measurement based friction estimation, Journal of Sound and Vibration, 384 (2016) 28-44.

[105] Z. Gan, A.J. Hillis, J. Darling, Adaptive control of an active seat for occupant vibration reduction, journal of sound and vibration, 349 (2015) 39-55.

- [106] R. Kieneker, C. Graf, J. Maas, Active seat suspension with two degrees of freedom for military vehicles, *IFAC Proceedings Volumes*, 46 (2013) 523-529.
- [107] H. Gavin, R. Hanson, F. Filisko, Electrorheological dampers, part I: analysis and design, DOI (1996).
- [108] H. Gavin, R. Hanson, F. Filisko, Electrorheological dampers, part II: testing and modeling, DOI (1996).
- [109] S.-B. Choi, M.-H. Nam, B.-K. Lee, Vibration control of a MR seat damper for commercial vehicles, *Journal of intelligent material systems and structures*, 11 (2000) 936-944.
- [110] S.-B. Choi, Y.-M. Han, MR seat suspension for vibration control of a commercial vehicle, *International journal of vehicle design*, 31 (2003) 202-215.
- [111] C. Park, D. Jeon, Semiactive vibration control of a smart seat with an MR fluid damper considering its time delay, *Journal of intelligent material systems and structures*, 13 (2002) 521-524.
- [112] S. McManus, K.S. Clair, P. Boileau, J. Boutin, S. Rakheja, Evaluation of vibration and shock attenuation performance of a suspension seat with a semi-active magnetorheological fluid damper, *Journal of Sound and Vibration*, 253 (2002) 313-327.
- [113] G.J. Hiemenz, Y.-T. Choi, N.M. Wereley, Semi-active control of vertical stroking helicopter crew seat for enhanced crashworthiness, *Journal of aircraft*, 44 (2007) 1031-1034.
- [114] H.J. Singh, N.M. Wereley, Influence of occupant compliance on a vertically stroking helicopter crew seat suspension, *Journal of Aircraft*, 52 (2015) 1286-1297.
- [115] H. Du, W. Li, N. Zhang, Semi-active variable stiffness vibration control of vehicle seat suspension using an MR elastomer isolator, *Smart materials and structures*, 20 (2011) 105003.
- [116] S. Sun, D. Ning, J. Yang, H. Du, S. Zhang, W. Li, M. Nakano, Development of an MR seat suspension with self-powered generation capability, *Smart Materials and Structures*, 26 (2017) 085025.
- [117] H.J. Singh, N.M. Wereley, Influence of occupant compliance on a vertically stroking helicopter crew seat suspension, *Journal of Aircraft*, 52 (2014) 1286-1297.
- [118] X.-X. Bai, N.M. Wereley, Magnetorheological impact seat suspensions for ground vehicle crash mitigation, *Active and Passive Smart Structures and Integrated Systems 2014*, International Society for Optics and Photonics, 2014, pp. 90570R.
- [119] X.-X.F. Bai, S. Yang, Hybrid controller of magnetorheological semi-active seat suspension system for both shock and vibration mitigation, *Journal of Intelligent Material Systems and Structures*, DOI (2019) 1045389X19844009.
- [120] R. Jiang, X. Rui, F. Yang, W. Zhu, H. Zhu, M. Jiang, Simulation and experiment of the magnetorheological seat suspension with a seated occupant in both shock and vibration occasions, *Smart Materials and Structures*, 29 (2020) 105008.
- [121] S.-B. Choi, K.-G. Sung, Vibration control of magnetorheological damper system subjected to parameter variations, *International Journal of Vehicle Design*, 46 (2008) 94-110.
- [122] A.M. Aly, Vibration control of buildings using magnetorheological damper: a new control algorithm, *Journal of Engineering*, 2013 (2013).
- [123] B. Yang, S. Sun, L. Deng, T. Jin, W. Li, H. Li, Vibration control of a tunnel boring machine using adaptive magnetorheological damper, *Smart Materials and Structures*, 28 (2019) 115012.
- [124] Y. Shen, M. Golnaraghi, G. Heppler, Semi-active vibration control schemes for suspension systems using magnetorheological dampers, *Journal of Vibration and Control*, 12 (2006) 3-24.



- [125] Y. Li, J. Li, W. Li, B. Samali, Development and characterization of a magnetorheological elastomer based adaptive seismic isolator, *Smart Materials and Structures*, 22 (2013) 035005.
- [126] B. Spencer Jr, S. Dyke, M. Sain, J. Carlson, Phenomenological model for magnetorheological dampers, *Journal of engineering mechanics*, 123 (1997) 230-238.
- [127] L. Deng, S. Sun, M.D. Christie, J. Yang, D. Ning, X. Zhu, H. Du, S. Zhang, W. Li, Experimental testing and modelling of a rotary variable stiffness and damping shock absorber using magnetorheological technology, *Journal of Intelligent Material Systems and Structures*, 30 (2019) 1453-1465.
- [128] D. Wang, W.H. Liao, Magnetorheological fluid dampers: a review of parametric modelling, *Smart materials and structures*, 20 (2011) 023001.
- [129] J. Tamboli, S. Joshi, Optimum design of a passive suspension system of a vehicle subjected to actual random road excitations, *Journal of Sound and vibration*, 219 (1999) 193-205.
- [130] A. Agharkakli, G.S. Sabet, A. Barouz, Simulation and analysis of passive and active suspension system using quarter car model for different road profile, *International Journal of Engineering Trends and Technology*, 3 (2012) 636-644.
- [131] M. Yu, C. Liao, W. Chen, S. Huang, Study on MR semi-active suspension system and its road testing, *Journal of intelligent material systems and structures*, 17 (2006) 801-806.
- [132] S. Sun, J. Yang, P. Wang, M. Nakano, L. Shen, S. Zhang, W. Li, Experimental Study of a Variable Stiffness Seat Suspension Installed With a Compact Rotary MR Damper, *Frontiers in Materials*, 8 (2021) 38.
- [133] D. Ning, S. Sun, H. Du, W. Li, Integrated active and semi-active control for seat suspension of a heavy duty vehicle, *Journal of Intelligent Material Systems and Structures*, 29 (2018) 91-100.
- [134] M. Ahmadian, X. Song, S.C. Southward, No-jerk skyhook control methods for semiactive suspensions, *J. Vib. Acoust.*, 126 (2004) 580-584.
- [135] M. Zubieta, S. Eceolaza, M. Elejabarrieta, M. Bou-Ali, Magnetorheological fluids: characterization and modeling of magnetization, *Smart Materials and Structures*, 18 (2009) 095019.
- [136] I. ISO, 2631-1: Mechanical vibration and shock-evaluation of human exposure to whole-body vibration-Part 1: General requirements, Geneva, Switzerland: ISO, DOI (1997).
- [137] M. Mao, Y.-T. Choi, N.M. Wereley, Effective design strategy for a magnetorheological damper using a nonlinear flow model, *Smart Structures and Materials 2005: Damping and Isolation*, International Society for Optics and Photonics, 2005, pp. 446-455.
- [138] J.B. Franzini, E.J. Finnemore, R.L. Daugherty, *Fluid mechanics with engineering applications*, McGraw-Hill College 1997.
- [139] T. Gunston, M. Griffin, The isolation performance of a suspension seat over a range of vibration magnitudes tested with an anthropodynamic dummy and human subjects, *INTER-NOISE and NOISE-CON Congress and Conference Proceedings*, Institute of Noise Control Engineering, 1999, pp. 949-954.

## Publications during my PhD study

1. **L Deng**, S. S. Sun, M. D. Christie, J. Yang, D. H. Ning, X. J. Zhu, H. P. Du, S. W. Zhang, W. H. Li. Experimental testing and modelling of a rotary variable stiffness and damping shock absorber using magnetorheological technology. *Journal of Intelligent Material Systems and Structures*, 30(10), 1453-1465, 2019.
2. **L Deng**, S. S. Sun, M. D. Christie, D. H. Ning, H. P. Du, S. W. Zhang, W. H. Li. Numerical investigation of rotary MR seat suspension on the impact protection. *International Conference on Applied Nonlinear Dynamics, Vibration, and Control*, 2021. (accepted)
3. **L Deng**, S. S. Sun, M. D. Christie, D. H. Ning, H. P. Du, S. W. Zhang, W. H. Li. Development of a Robotic Arm Positioning System Based on a Variable Damping and Stiffness Magnetorheological Damper. *IEEE/ASME TRANSACTIONS ON MECHATRONICS*, (under review).
4. **L Deng**, S. S. Sun, M. D. Christie, D. H. Ning, H. P. Du, S. W. Zhang, W. H. Li. Vibration control of a seat suspension using VSVD magnetorheological damper. *Mechanical Systems and Signal Processing*, (submitted)
5. S. D. Jin§, **L. Deng§**, J. Yang, S. S. Sun, D. H. Ning, Z. X. Li, H. P. Du, W. H. Li. A Smart Passive MR Damper with a Hybrid Powering System for Impact Mitigation: An Experimental Study. *Journal of Intelligent Material Systems and Structures*, 2021. (Co-first author)
6. X. J. Zhu, **L. Deng**, S. S. Sun, T. H. Yan, J. Q. Yu, Z. S. Ma, W. H. Li. Development of a variable stiffness magnetorheological damper with self-powered generation capability. *Journal of Intelligent Material Systems and Structures*, 31(2)(2020), 209-219.
7. M. D. Christie, S. S. Sun, **L. Deng**, D. H. Ning, H. P. Du, S. W. Zhang, W. H. Li. A variable resonance magnetorheological-fluid-based pendulum tuned mass damper for seismic vibration suppression. *Mechanical Systems and Signal Processing*, 116 (2019): 530-544.
8. B. Yang, S. S. Sun, **L Deng**, T. H. Jin, W. H. Li, H. Li. Vibration control of a tunnel boring machine using adaptive magnetorheological damper, *Smart Materials and Structures* 28, no. 11 (2019): 115012.

9. M. D. Christie, S. S. Sun, **L. Deng**, D. H. Ning, H. P. Du, S. W. Zhang, W. H. Li. The variable resonance magnetorheological pendulum tuned mass damper: Mathematical modelling and seismic experimental studies, *Journal of Intelligent Material Systems and Structures* 31, no. 2 (2020): 263-276.
10. B. Yang, S. M. Chen, S. S. Sun, **L. Deng**, Z. Q. Li, W. H. Li, H. Li. Vibration suppression of tunnel boring machines using non-resonance approach, *Mechanical Systems and Signal Processing* 145 (2020): 106969.
11. M. D. Christie, S. S. Sun, Q. H. Joshua, **L. Deng**, H. P. Du, W. H. Li. A Magnetorheological fluid based planetary gear transmission for mechanical power-flow control, *Smart Materials and Structures* (2021).
12. J. Yang, S. S. Sun, D. H. Ning, Z. X. Li, **L. Deng**, M. D. Christie, H. P. Du, S. W. Zhang, W. H. Li. Development and evaluation of a highly adaptive MRF-based absorber with a large effective frequency range. *Smart Materials and Structures* 28, no. 10 (2019): 105003
13. T. H. Jin, Z. M. Liu, S. S. Sun, Z. S. Ren, **L. Deng**, B. Yang, M. D. Christie, W. H. Li. Development and evaluation of a versatile semi-active suspension system for high-speed railway vehicles, *Mechanical Systems and Signal Processing* 135 (2020): 106338.
14. T. H. Jin, Z. M. Liu, S. S. Sun, Z. S. Ren, **L. Deng**, D. H. Ning, H. P. Du, W. H. Li. Theoretical and experimental investigation of a stiffness-controllable suspension for railway vehicles to avoid resonance. *International Journal of Mechanical Sciences* 187 (2020): 105901.
15. S. Y. Tang, X. C. Zhang, S. S. Sun, D. Yuan, Q. B. Zhao, S. Yan, **L. Deng**, G. L. Yun, J. Zhang, S. W. Zhang, W. H. Li. Versatile microfluidic platforms enabled by novel magnetorheological elastomer microactuators. *Advanced Functional Materials*, 28(8) (2018), p.1705484.
16. G. L. Yun, S. Y. Tang, S. S. Sun, D. Yuan, Q. B. Zhao, **L. Deng**, S. Yan, H. P. Du, M. D. Dickey, W. H. Li. Liquid metal-filled magnetorheological elastomer with positive piezoconductivity. *Nature communications* 10, no. 1 (2019): 1-9.
17. G. L. Yun, S. Y. Tang, Q. B. Zhao, Y. X. Zhang, H. D. Lu, D. Yuan, S. S. Sun, **L. Deng**, M. D. Dickey, W. H. Li. Liquid metal composites with anisotropic and unconventional piezoconductivity. *Matter* 3, no. 3 (2020): 824-841.

## Appendix

### The modified VSVD damper for position control of a robotic arm

In the appendix, the structure design and experimental test of the VSVD damper for the robotic arm positioning system are introduced. The VSVD damper is a modification of the VSVD damper in chapter 3, with its internal damper, new shaft&rotor and new casing redesigned. Additionally, its rubber spring was also replaced with a thicker and softer one. Considering it has different structure and characteristics, its structure design and experimental tests are presented here.

#### *Mechanical structure of the proposed VSVD damper*

As shown in **Figure A.1**, the new VSVD damper consists of a drum-type internal damper unit that controls the damping and a disk-type external damper unit that controls the stiffness. Compared with our previous damper reported in [127], the new VSVD damper has a large internal damper rotor that with more working areas to increase the damping output, and has a thicker rubber spring to reduce the stiffness. The internal damper casing is fixed to an unmovable base and an aluminium part of the external damper. With a small permeability, this aluminium part works as a magnetic insulator between the internal and the external damper to make sure they can be controlled separately without interference. Other aluminium parts as demonstrated in the figure are also utilised in both the internal and external damper units to optimise the magnetic flux distribution. The shaft, which is also integrated with the internal damper rotor, connects both the gearbox and motor on the bottom side, and the plate on the upper side. The plate works as an output, and it connects to the robotic arm. A cylindrical rubber spring made of silicone rubber (4601A/B, Barnes crop.) connects both the plate and the external damper casing. Two electromagnetic coils (0.5mm copper wire, 180 turns each) are wound on the internal damper rotor in opposite directions to enhance the magnetic field distribution. The applied current on these two coils is prescribed as the internal damper current  $I_1$ . Besides, an external damper coil is seated in the external damper casing (0.5 mm copper, 200 turns). The corresponding current applied is prescribed as external damper current  $I_2$ . For both the internal and external dampers, MRFs (MRF-132GD, Lord crop.) is filled in the 0.8 mm gaps (black chambers in Figure 10). All the parts in the yellow block including the internal damper casing and the external damper

disk cannot rotate. Other parts such as the internal damper rotor and the external damper casing are rotatable.

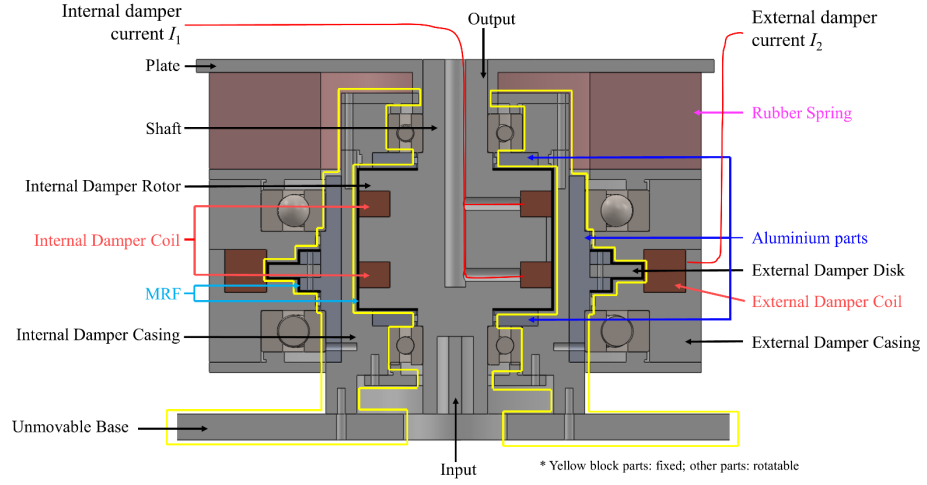


Figure A.1. Schematic of the VSVD MR damper

Without current given to both the internal damper and the external damper ( $I_1 = I_2 = 0$  A), the internal damper rotor, plate, rubber spring and external damper casing can rotate freely against the fixed parts. Apart from the motor torque, the initial torque of the internal damper is added to the torque output. At the same time, the rubber spring is slightly twisted to overcome the initial torque of the external damper so that the external damper casing can rotate following the rotation of the plate. In this case, the output torque acting on the arm is the motor torque plus the initial torques of the internal and external damper. If  $I_1 > 0$  A, the damping torque of the internal damper will increase so the damping torque of the VSVD damper will increase. The damping torque of the external damper will also increase if  $I_2 > 0$  A. In this case, the rubber spring will make a large twist to yield the increased damping torque of the external damper. At the same time, a large spring torque will be added to the output torque, and the stiffness of the VSVD damper increases as a result.

#### *Experimental tests for property characterization*

To characterise the VSVD damper, a test platform similar to **Figure 4.1** was built, as shown in **Figure A.2**. Compared with the configuration in **Figure 4.1**, the robotic arm wasn't installed and a power supply replaced the amplifier to provide currents to the internal and external damper currents.

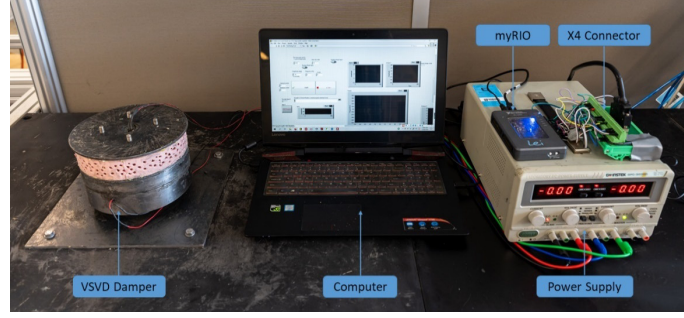
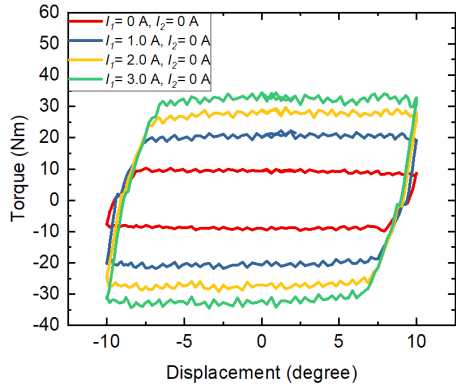


Figure A.2. Experimental setup of the property test

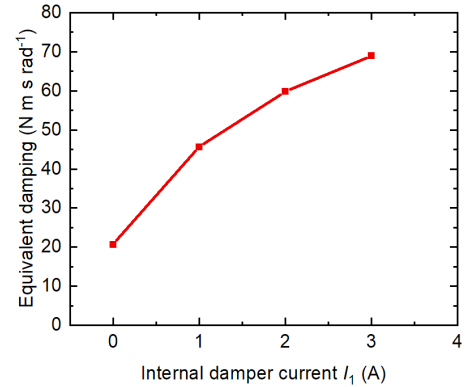
**Figure A.3** presents the damping variability of the VSVD damper as  $I_1$  increases from 0 to 3.0 A with a step of 1.0 A. The external damper current was set as 0 A in this test. The harmonic signal with amplitude  $A = 10$  degrees and frequency  $f = 0.5$  Hz was prescribed as the test input. The torque-displacement response of the variable damping tests is demonstrated in **Figure A.3(a)**, and the corresponding equivalent damping is plotted in **Figure A.3(b)**, which is calculated by [125]:

$$C_{t,eq} = \frac{EDC}{2\pi^2 f A^2} \quad (A-1)$$

where  $C_{t,eq}$  is the equivalent damping coefficient;  $EDC$  represents the energy dissipated per cycle, namely the area enclosed of each torque-displacement loop.



(a) Torque-displacement response



(b) Equivalent damping

Figure A.3. Experimental result of variable damping test

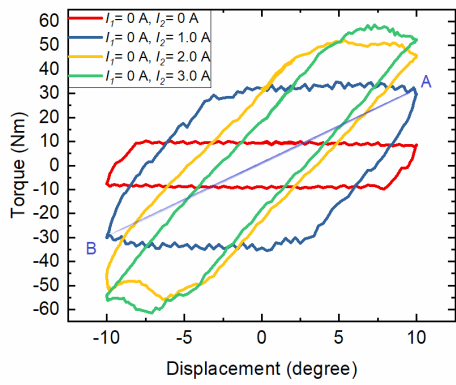
It is seen from **Figure A.3(a)** that the maximum torque output of the internal damper increased 350.84% from around 9.54 to 33.47 N·m as  $I_1$  increases from 0 A to 3.0 A. Represented by the area of the enclosed cycle, EDC also shows an increasing tendency. As plotted in **Figure A.3(b)**, the equivalent damping is increased from 20.64 to 68.98 N·m s rad<sup>-1</sup> with the change of currents.

To test the stiffness variability,  $I_2$  was increased from 0 to 3.0 A with an increment

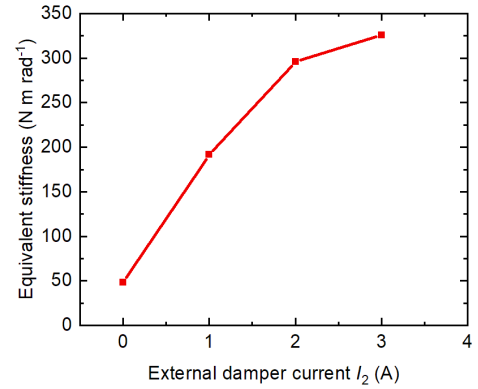
of 1.0 A, and  $I_1$  was set to be 0 A during the stiffness variability test. The test input was the same as the previous variable damping test. From **Figure A.4(a)**, we can see that the maximum torque of the output increased from around 9.54 N·m to 60 N·m as the increase of  $I_2$ . Equivalent stiffness  $K_{eff}$  is also presented in **Figure A.4(b)**, and it is calculated by the following equation [125]:

$$C_{t,eq} = \frac{EDC}{2\pi^2 f A^2} \quad (A-2)$$

where  $T_{max}$  and  $T_{min}$  represent the maximum and the minimum torque of the output.  $A_{max}$  and  $A_{min}$  are the maximum and the minimum of the displacements. Take the torque-displacement loop of ‘  $I_1=0$  A,  $I_2=1.0$  A ’ as an example, the calculated equivalent stiffness under this condition is represented by the ratio of line AB in **Figure A.4(a)**. From **Figure A.4(b)**, it is known that the equivalent stiffness of the damper has a 671.40% increase from 48.50 to 325.63 N·m rad<sup>-1</sup>.



(a) Torque-displacement loop



(b) Equivalent stiffness

Figure A.4. Experimental result of variable stiffness test